

Turbulent Particle Transport and its Effect on Flotation

Proefschrift

ter verkrijging van de graad van doctor
aan de Technische Universiteit Delft,
op gezag van de Rector Magnificus prof. ir. K.C.A.M. Luyben,
voorzitter van het College voor Promoties,
in het openbaar te verdedigen op dinsdag 13 mei 2014 om 12:30 uur

door

Norbert Gustav Werner WARNCKE
Diplom-Physiker, Technische Universität Braunschweig, Deutschland,
geboren te Wurzen, Duitsland.

Dit proefschrift is goedgekeurd door de promotor:
Prof.dr.ir. J. Westerweel

Samenstelling promotiecommissie:

Rector Magnificus,	voorzitter
Prof.dr.ir. J. Westerweel,	Technische Universiteit Delft, promotor
Prof.dr.ir. W. van de Water,	Technische Universiteit Eindhoven,
Prof.dr.ir. H.W.M. Hoeijmakers,	Universiteit Twente,
Prof.dr.ir. C. van Rhee,	Technische Universiteit Delft,
Prof. M. Reeks,	Newcastle University,
Dr. R. Delfos,	Technische Universiteit Delft,
Ir. D. van der Plas,	Tata Steel,
Prof.dr.ir. G. Ooms,	Technische Universiteit Delft, reservelid



The work in this thesis was carried out at the Aero&Hydrodynamics Laboratory of the faculty of Mechanical, Maritime and Materials Engineering of the Delft University of Technology. It was part of the project 07510 “Flotation and de-mixing of turbulent three-phase flows” of the “Stichting voor de Technische Wetenschappen”. The project was co-financed by Tata Steel.

Copyright ©2014 by N.G.W. Warncke.
All rights reserved.
ISBN 978-94-6108-678-5

Printed by Gildeprint, Enschede

Contents

1	Introduction	1
1.1	A Sphere Immersed in a Fluid – the “Terrible” Problem of Fluid Mechanics	2
1.2	Flotation in Industrial Applications	2
1.3	Flotation in the Continuous Casting Process	3
1.4	Transport of Cyanobacteria in Bodies of Water	5
1.5	Research Motivation and Problem Definition	6
1.6	Outline of this Thesis	6
2	Theory and Entrainment Model	9
2.1	Single Particle Dynamics: A Sphere in a Fluid	11
2.1.1	Fundamental Theory	11
2.1.2	Forces in the Point Particle Approximation	14
2.1.3	Equations of Motion for a Spherical Particle	24
2.1.4	Weak-Inertia Approximation	27
2.2	A Model for the Near-Wake	29
2.3	A Model for Particle Entrainment	30
2.3.1	Particle Entrainment in a Spherical-Cap Wake	30
2.3.2	The Influence of Gravity	36
2.3.3	A Model for an Elliptical Wake	38
2.3.4	Convergence to the Stationary State	42
2.3.5	The Contribution of Turbophoresis	43
3	Experiments on Particle Entrainment	45
3.1	Experimental Setup	46
3.1.1	Vermeer-Setup	46
3.2	Data Correction and Analysis	49
3.2.1	Image Alignment for 2-phase PIV	49
3.2.2	Detection of Wake Boundaries	56
3.2.3	Flux Measurements	58

3.2.4	Concentration Measurements	65
4	Results on Particle Entrainment	77
4.1	The Wake of a Spherical Cap	78
4.1.1	Qualitative Description	78
4.1.2	Flow Length and Time Scales	82
4.2	Particle Transport over the Wake Boundary	85
4.2.1	Analysis of the Flux Data	85
4.2.2	Discussion of the Flux Measurement Results	88
4.3	Preferential Concentration	88
4.3.1	Dependency on Particle Properties	88
4.3.2	Discussion of the Concentration Measurements	93
5	Surface Attachment	95
5.1	Models for Particle-Bubble Attachments	96
5.1.1	Particle-Bubble Encounter	97
5.1.2	Particle Attachment	100
5.1.3	Particle Detachment	104
5.1.4	A Model for the Surface Coverage	106
5.2	Measurements of Particle Attachment Rates	107
5.2.1	The DABuT Facility	110
5.2.2	Measurement Principle	111
5.2.3	Methods for Image Analysis	113
5.2.4	Qualitative results	120
5.2.5	Observations	123
5.2.6	Discussion of the Attachment Measurements	143
6	Applicability and Conclusion	147
6.1	The Wake Experiments and the Wake Model	148
6.2	The Bubble Experiments	149
6.3	Applicability of the Results	151
6.3.1	Make it Turbulent!	151
6.3.2	Scaling of Wake Entrainment with Bubble Volume	151
6.3.3	Estimates of Removal Rates	152

List of Figures

1.1	Electron microscopy records of cavities of argon bubbles in solidified steel	4
2.1	Spherical model for the near-wake behind a spherical-cap gas bubble	31
2.2	Measured particle concentration in the wake of a solid spherical cap	34
2.3	Coordinate system for the flow around a prolate ellipsoid	38
3.1	Schematic drawing of the VerMeer facility	47
3.2	Correction of camera misalignments for an external target	52
3.3	Effect of displacements of the wake boundary	55
3.4	Methods for determining the wake boundary	57
3.5	Velocities normal to the elliptic boundaries	59
3.6	Dependence of the flux error estimate on the number of interpolation points at the wake boundary	61
3.7	Convergence of the flux measurement	63
3.8	Bootstrapping of the flux results	64
3.9	Mie-scattering for a $55\mu\text{m}$ gas bubble (hollow sphere) .	67
3.10	Schematic drawing of the particle imaging	68
3.11	Illustration of the image processing steps	74
3.12	Bubble concentration with Shadowgraphy	75
4.1	Instantaneous and time-averaged velocity field	79
4.2	Comparison of the near wake for different Re and Tl . .	80
4.3	Deformation of the near-wake for low Re	81
4.4	Wake size over Re	82
4.5	Relative standard deviation u'_n/U_∞ as a function of θ .	84
4.6	Measured particle flux versus the estimated flux	87
4.7	Particle concentration over St	91

List of Figures

5.1	Imaging setup of DABuT	110
5.2	Test section and bubble injector of the DABuT setup . .	111
5.3	Principle of the attachment measurements	112
5.4	Stability of the POD colour space decomposition	116
5.5	Bimodal distribution of the pink signal	117
5.6	Uncertainties in the particle counting	118
5.7	Time-development of the particle concentration	120
5.8	Observed monolayers on bubble surfaces	123
5.9	Selected records of a time series with a semi-spherical bubble, 4g PE particles of diameter 53-63 μm	125
5.10	Selected records of a time series with a wobbling-ellipsoidal bubble, 2g PE particles of diameter 53-63 μm	127
5.11	Selected records of a time series with a group of small bubbles, 8g PE particles of diameter 53-63 μm	128
5.12	Clusters of millimetre-sized bubbles and particles (106- 125 μm) in the wake of a Taylor bubble	129
5.13	Selected records of a time series with a Taylor bubble, 6g PE particles of diameter 75-90 μm	130
5.14	Time-development of the bubble surface area covered by particles	131
5.15	Bias in the particle counting	132
5.16	Covered surface area over time, 27-45 μm and 53-63 μm particles	133
5.17	Covered surface area over time, 75-90 μm and 106-125 μm particles	134
5.18	Comparison of the single-step and two-step behaviour of surface coverage over time	136
5.19	Covered surface area over time for a wobbling-ellipsoidal bubble	137
5.20	Observed two-step behaviour	138
5.21	Time-series with a double-step behaviour	140
5.22	Problems of the two-step model	142

List of Tables

3.1	Legend to Fig. 3.1	46
3.2	Selected parameters of the VerMeer facility	50
3.3	Alignment matrix coefficients and coefficient errors (mean μ and standard deviation σ for two data sets, recorded with filters removed (autocalibration)	53
3.4	Systematic alignment errors due to installed filters	54
4.1	Estimates of relevant turbulent length and time scales	83
4.2	Summary of the particle flux measurements	86
4.3	Properties of the particles types used for the measurements	89
4.4	Overview of selected measurement results	90
5.1	Parameters for the particle attachment measurements	108
5.2	Selected parameters of the measurements in the DABuT facility	112
5.3	Attachment time scales T_{att} obtained from fitting Eq. (5.19) for all measured semi-spherical bubbles	139
5.4	Time scales obtained from the two-step model	143

Summary

This thesis studies the hydrodynamics of froth flotation, a process that is used in industry as a means of removing small inclusions from the treated liquid by gas bubble injection. This work is particularly motivated by the removal of aluminium and silicon oxides from liquid steel.

Hydrodynamic aspects have a strong influence on the efficiency of froth flotation. The flow around a rising bubble, especially the turbulent flow in the near-wake, is of particular importance as it may cause preferential concentration of particles as well as significantly change the collision and attachment rates of particles with the surface of the bubble. Both effects are studied in this work.

Preferential concentration of particles in the near-wake is a result of the time-averaged balance of inertial and pressure forces on a dispersed particle, resulting in a drift towards the wake. It can therefore be observed by an effective time-averaged particle slip velocity over the wake boundary. Likewise, a direct confirmation of preferential concentration is possible by measurements of the average concentration of particles in the wake. These measurements were done in the wake of a solid mock-up of a spherical-cap bubble in the VerMeer vertical water tunnel. The particle slip velocity was obtained from simultaneous two-phase Particle Image Velocimetry measurements and numerically integrated in post-processing. The particle concentration was obtained directly from the average scattered light intensity. Both experimental results are compared to the predictions of a model for the preferential concentration in the wake, derived from a local balance of inertial, gravitational and diffusive fluxes.

The influence of turbulence on particle attachment rates was measured in the newly constructed DABuT (Dynamic Air Bubble Trap) facility, using bubbles of different shapes and volumes. The research was again focused on the semi-spherical bubbles, these were also found to have the highest attachment rates. The results of the measurements are compared to a model based on a turbulent attachment flux and the

List of Tables

effective shielding of particle attachments by a mono layer of particles building up and finally covering the rear side of the bubble in proximity to the wake.

In conclusion, both effects contribute to the overall efficiency of flotation. the results of this work suggest that spherical-cap bubbles — although potentially difficult to generate — have the highest potential for the optimisation of flotation processes in industry.

Samenfatting

Dit proefschrift beschrijft de hydrodynamica van bellen-flotatie, een proces dat industrieel wordt toegepast om kleine deeltjes uit vloeistoffen te verwijderen door middel van gasbel-injectie. Dit werk is specifiek gemotiveerd op het verwijderen van aluminium en siliciumoxiden uit vloeibaar staal.

Hydrodynamische effecten hebben een grote invloed op de efficiëntie van bellen-flotatie. De stroming rondom een opstijgende gasbel, en in het bijzonder de turbulentie in het zog direct achter de bel, is belangrijk omdat deze kan leiden tot een preferente concentratie van deeltjes in het zog, maar ook invloed heeft op het botsings- en het aanhechtingsproces aan het oppervlak van de bel. Beide effecten zijn beschreven in dit proefschrift.

Preferente concentratie van deeltjes in het belzog is het resultaat van een tijdsgemiddelde balans tussen traagheids- en drukkrachten op de deeltjes, leidend tot een naar het belzog gerichte flux van deeltjes. Deze kan waargenomen worden door een tijds-gemiddelde driftsnelheid over de rand van het belzog. Anderzijds is een directe bevestiging van preferente concentratie te meten aan de hand van de gemiddelde concentratie in het belzog. Deze metingen zijn uitgevoerd in het zog van een vast model voor een 'spherical cap' (half-ronde) gasbel in de 'VerMeer' verticale watertunnel. De driftsnelheid van de deeltjes is verkregen aan de hand van twee-fasen Particle Image Velocimetry metingen en in een nabewerking numeriek geïntegreerd. De deeltjesconcentratie werd direct verkregen uit de intensiteit van het verstrooide laserlicht.

Beide experimentele resultaten zijn vergeleken met de voorspellingen van een fysisch model voor preferente concentratie afgeleid op basis van lokale balansen van fluxen veroorzaakt door traagheid, zwaartekracht en turbulente diffusie.

De invloed van turbulentie op de snelheid van deeltjes-aanhechting aan het beloppervlak is gemeten in de nieuw geconstrueerde DABuT (Dynamic Air Bubble Trap) meetopstelling voor bellen van variërende

List of Tables

vorm en volume. De focus lag opnieuw op half-ronde bellen, waarbij werd gevonden dat deze ook het meest efficiënt zijn.

De meetresultaten zijn vergeleken met een fysisch model gebaseerd op een turbulente aanhechtingsflux en effectieve afscherming door een zich geleidelijk vormende mono-laag van deeltjes die de zog-zijde van de gasbel uiteindelijk volledig afdekt.

In conclusie dragen beide effecten bij aan de overall efficiëntie van flotatie. De resultaten van dit proefschrift tonen aan dat half-ronde "spherical-cap" bellen - hoewel wellicht moeilijk te maken - het beste potentieel hebben voor het optimaliseren van industriële flotatie-processen.

Zusammenfassung

Ziel dieser Dissertation ist die Untersuchung der Hydrodynamik der Schaumflotation, ein Prozess zur Trennung von dispersen Feststoffen von der Trägerflüssigkeit durch die Injektion von Gasblasen. Diese Arbeit ist insbesondere motiviert durch das Entfernen von Oxiden (Alumina- und Silica-Partikel) aus Stahlschmelzen.

Hydrodynamische Effekte sind von großer Bedeutung für die Effektivität des Flotationsprozesses. Die Strömung um eine aufsteigende Gasblase, und insbesondere die turbulente Strömung in deren Nachlauf, ist besonders bedeutsam, da sie die Ursache darstellt für eine erhöhte Partikelkonzentration im Nachlauf und ebenso Einfluss hat auf die Stoßwahrscheinlichkeit von Partikeln mit der Blasenoberfläche. Diese beiden Effekte werden in dieser Arbeit untersucht.

Die Anreicherung von Partikeln im Nachlauf ist das Ergebnis eines Kräftegleichgewichts im zeitlichen Mittel zwischen Trägheits- und Druckkräften auf ein suspendiertes Partikel, welches eine zum Nachlauf gerichtete Bewegung zur Folge hat. Diese Bewegung kann durch eine effektive Driftgeschwindigkeit der Partikel im zeitlichen Mittel und relativ zum Fluid beobachtet werden. Die Anreicherung von Partikeln im Nachlauf kann über eine Messung der mittleren Partikeldichte auch direkt gemessen werden. Diese Messungen wurden im Nachlauf eines Messingmodells einer Blase in dem vertikalen VerMeer-Wasserkanal durchgeführt. Die Driftgeschwindigkeit der suspendierten Partikel wurde mittels Mehrphasen-PIV bestimmt und in der Nachbearbeitung numerisch über den Rand des Nachlaufs integriert. Die Partikeldichte wurde direkt über die mittlere Intensität des Streulichtes bestimmt. Die Ergebnisse beider Experimente wurden mit den Vorhersagen eines Modells für die Partikelanreicherung im Nachlauf verglichen, welches auf der Annahme eines Gleichgewichts der Terme für die trägheitsbedingte, die gravitative und die diffusive Partikelflussdichte basiert.

Der Einfluss der Turbulenz auf die Stoßrate wurde in dem neu entwickelten DABuT Versuchsaufbau gemessen, unter Benutzung von ver-

List of Tables

schieden Blasenvolumen und -formen. Die Untersuchung wurde wiederum hauptsächlich an halbkugelförmigen Blasen durchgeführt, da bei diesen die höchsten Stoßraten gefunden wurden. Die Ergebnisse dieser Messungen wurden mit einem Modell verglichen, welches auf einer turbulenten Stoßflussdichte und der Abschirmung durch bereits mit Partikeln beladenen Oberflächenteilen basiert, welche nach einer gewissen Zeit die komplette Rückseite der Blase bedecken.

Das Ergebnis dieser Arbeit ist, dass beide Effekte einen Einfluss auf die Effizienz des Flotationsprozesses haben. Blasen in Form eines Kugelabschnittes haben, trotz möglicher Probleme bei deren Erzeugung in industriellen Anlagen, dabei das größte Potential für die großtechnische Optimierung der Flotation.

1 Introduction

1.1 A Sphere Immersed in a Fluid – the “Terrible” Problem of Fluid Mechanics

The scientific field of fluid mechanics deals — as the name suggests — with the dynamics of the motion of fluids. Although there have been considerable efforts spent to understand the dynamics of a fluid in an unbound domain (e.g. in the case of homogeneous, isotropic turbulence), the problem is of practical interest as soon as the flow domain is bounded by walls, which is confirmed by the fundamental works Poiseuille on pipe flows, and those of Ludwig Prandtl (Prandtl, 1904) on the boundary layer. In 1851, Sir George Gabriel Stokes already published his famous work (Stokes, 1851) on a flow that is “bounded from the inside”, that is the viscous flow around a sphere.

In 2013, a search on Web of Science[®] for the keywords “fluid flow” and “particle” gives almost 25000 search results after the year 1900, and over 17000 for a period over the last ten years. This shows that there is a considerable — and still growing — interest in this field, driven by a wide range of applications in industry and nature. This work is dedicated to the understanding of the hydrodynamic processes found in one of these industrial applications: *Flotation*, that is the effect of particle transport induced by gas bubbles rising in a fluid.

1.2 Flotation in Industrial Applications

Gaudin (1957) writes that “flotation is a process for separating finely divided solids from each other”. It is phase separation technique that was originally used to separate (valuable) ore from (invaluable) stone after being crushed to pieces/powder (*bulk-oil flotation*¹). The flotation process then was applied to other separation problems in the chemical industry and is nowadays a major process with a wide range of applications. In the literature it is therefore not divided by application anymore but by the process particles attach to a carrier phase: *skin or film flotation* at water-air surfaces, and *froth flotation* when separated particles and the carrier gas form a froth on the surface.

The importance of the flotation process for science is maybe best summarised by the following quote attributed to P.A. Rehbinder: “Flotation

¹Terminology from Gaudin (1957).

is the encyclopaedia of colloid sciences” (from Nguyen & Schulze, 2004, who also gives a nice overview over the historical development of the process). The complexity of the problem arises from the wide range of phenomena that influence it, from the macroscopic scale of the flow around the rising gas bubbles to the break-up of the thin liquid film at molecular scale. Next to hydrodynamic forces, these small scales are strongly influenced by electrostatic forces in the form of dipole layers and surface charges

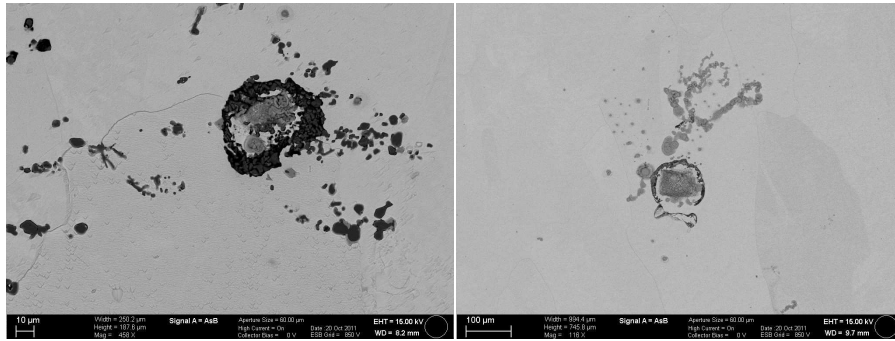
1.3 Flotation in the Continuous Casting Process

Besides chemical factors that influence the quality of steel, Zhang & Thomas (2003) give an overview about the degradation of steel quality by non-metallic inclusions that is summarised here in the following. They write that the “source of most fatigue problems in bearing steel are hard and brittle oxides, especially large alumina particles over $30\mu\text{m}$ ”. These inclusions have further negative impact on the quality as they locally reduce ductility and cause voids and cracks during rolling.

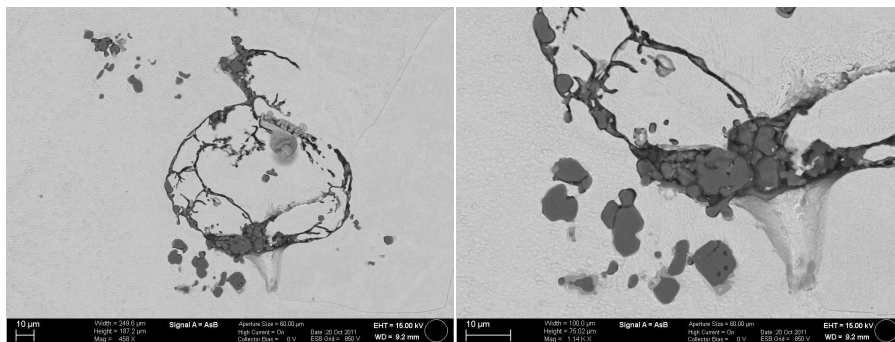
These non-metallic inclusions can be created indigenous by the deoxidisation of pure iron by adding Aluminium or Silicon as deoxidants to the mould. These alumina and silica particles crystallise and form larger clusters by collision and aggregation. A further source of inclusions (so-called precipitated inclusions) is caused by the reduction of solubility during cooling and solidification of the steel. These inclusions consist again of alumina and silica, but also of Nitride and Sulphides, and are typically smaller ($< 10\mu\text{m}$). Exogenous inclusions are those that enter the steel by reoxidation, slag entrainment or the erosion of lining refractory. Flotation is therefore used to remove these inclusions (besides the precipitated inclusions) by injecting Argon gas into the mould in ducts/nozzles and the tundish.

Fig. 1.1 shows electron microscopy images of samples taken from solidified steel. The argon bubbles leave a cavity in the solidified steel where typically agglomerates of inclusions can be found either near the cavity or directly on its surface, see Fig. 1.1(a). The alumina inclusions are dark grey in the images, the lighter grey particles are oxides that are created during preparation of the sample. The equilibrium size of Argon bubbles in liquid steel is in the range of 3 to 8 mm in diameter,

1 Introduction



(a) Argon bubble with inclusions and smaller bubbles in the wake



(b) Accumulation of inclusions in the wake and on the surface of a cavity originating from a bubble



(c) Cavity from an Argon bubble with inclusions (dark grey), the light grey areas in the cavity are not inclusions but the remains of oxidised steel during sample preparation

Figure 1.1: Electron microscopy records of cavities of argon bubbles in solidified steel. By courtesy of Tata Steel

the smaller cavities (approximately $100\ \mu\text{m}$ in diameter) shown in the images were created in cases where the buoyancy was insufficient for the bubble to depart the mold during solidification. The accumulation of inclusions near the surface of the bubble can be seen in Figures 1.1(b) and 1.1(c) (left) and also in the magnified parts (right). The number “1” in Fig. 1.1(c) (right) marks a dark-grey alumina inclusion.

1.4 Transport of Cyanobacteria in Bodies of Water

Particle transport in natural bodies of water is often related to microorganisms and their seasonal cycle of growth and decay. *Microcystis aeruginosa* is a planktonic cyanobacteria with the ability to control buoyancy by growing gas vesicles inside cells and interstitially by nutrient intake and photosynthesis. Their seasonal cycle is described in detail in Zohary & Robarts (1990) and is summarised here in the following. In spring, increasing solar irradiance causes higher near-surface water temperatures leading to thermal stratification. These circumstances together with high grazing pressures on competitive algal species give *Microcystis aeruginosa* advantages that lead to high growth rates and finally the formation of hyperscums, millimetre-thick algal films directly under the water surface that prevent gas exchange (see Ploug (2008) for a study on different cyanobacteria species with similar characteristics causing blooms in the Baltic Sea) and severely hinders light penetration to deeper zones. These hyperscums typically reach their maximum extent mid-summer and disappear due to stronger agitation of the water surface by winds in autumn. The hyperscums can nevertheless reach a second (lower) maximum during winter under conditions (low water temperature, less solar irradiation) that typically prevent any growth. This effect can therefore be attributed to the flotation of existing cyanobacteria colonies to the surface in calm waters.

Similar to algae blooms (high concentrations below the surface), the emergence of hyperscums of cyanobacteria at the surface is particularly hazardous to other species and has severe implications on the quality of drinking water. The (re)appearance of both hyperscums and blooms is particularly interesting for this work as they appear on a timescale smaller than what would be expected for their natural buoyancy.

1.5 Research Motivation and Problem Definition

Only a small aspect of the whole flotation problem is studied in this work, namely the hydrodynamic influence on the whole process. Two aspects of the fluid flow can potentially be relevant to flotation, the direct transport of inclusions by the gas bubble due to preferential concentration in the wake, and the influence of a turbulent flow on the attachment rates of particles to the surface of the bubble. Both effects are investigated in this work. Although also the attachment process is a result of the hydrodynamic instability of the thin liquid film between inclusion and bubble surface, leading to the break-up of the film and the formation of a stable three-phase contact line, the scale at which this process occurs are too small to be experimentally accessible.

1.6 Outline of this Thesis

The first part of Ch. 2 tries to stretch an arc from Newton's second law to the equation of motion for a particle in a fluid, and explains briefly all contributing terms. Newton's second law is essential the underlying principle for deriving the Navier-Stokes equation, the governing equation for describing the time-development of the momentum of a viscous fluid in an Eulerian frame of reference. For small particle Reynolds numbers, a solution of the simplified Navier-Stokes equation can be obtained analytically and the forces presented and discussed in Sec. 2.1.2 can be derived from the resulting flow field. The reason for this classification is that — despite the fact that all forces and moments can be combined to a single integral over the particle's boundary each — all forces relate to somewhat different effects and do not contribute under certain conditions.

After discussing all contributing forces, a brief survey is given in Sec. 2.1.3 on combining the contributing forces to an equation of motion for a particle immersed in a non-stationary flow. This survey is finishing with the well-known Maxey-Riley-Gatignol equation that is used to describe a particle for a low particle Reynolds number throughout the modern literature. By simplifying this equation further to the so-called weak-inertia approximation in Sec. 2.1.4, one part of the basis is obtained for modelling preferential concentration in a wake.

The second part needed is a model for the flow around and in the near-wake of a spherical-cap bubble. It is obtained by extending the spherical-wake model of Dayan & Zalmanovich (1982) to an ellipsoid of rotation, a fact that is motivated by the experimental results presented in Sec. 4.1. Putting together the weak-inertia approximation with this flow field resulted in the model derived in Sec. 2.3 for the preferential concentration of particles in the near-wake. Ch. 2 is concluded with a discussion of the dimensionless numbers that are the parameters of the model for the preferential concentration of particles in the near-wake.

Ch. 3 describes the facilities used for the experiments as well as the necessary alignment and calibration methods. These measurements were done using a solid spherical cap in a vertical water tunnel, a simplification that was made necessary because real air bubbles could not be used in this facility without extensive modifications. The chapter discusses the two approaches that were used to measure the preferential concentration, the indirect way via the integration of the time-averaged particle flux over the wake boundary in Sec. 3.2.3, and by measuring the particle concentration directly from the raw PIV images in Sec. 3.2.4, integrated over the near-wake of the spherical cap and relative to the concentration in the outer flow.

Before describing the measurement principle in Sec. 3.2.3 and the detection of the wake boundary in Sec. 3.2.2, the image alignment is discussed in detail in Sec. 3.2.1 as it is crucial to the obtained measurement accuracy of this method. The section is concluded by an assessment of the uncertainties of the resulting flux results in Fig. 3.7.

For the direct measurement of particle concentration described in Sec. 3.2.4, two methods were developed to obtain concentration data from the scattered light intensity that deal with the inhomogeneity in the illumination in different ways: the method described in Eq. (3.18) is based on a model for the inhomogeneous illumination that can be fitted to the data for normalisation. All contributions to this illumination model are also discussed. The other method presented in Eq. (3.24) is based on a trick: a relative concentration increase can be obtained by dividing two data sets measured with different flows but under identical conditions of illumination. This chapter is concluded by a comparison of the two methods: despite potentially better results with the first method, it introduces a bias to the resulting concentration value that can be of the order of the result. It is a consequence of the model

1 Introduction

for the Mie scattering of the dispersed particles, which does not always match reality. All results presented in the following chapter are therefore obtained using the normalisation trick, despite much larger statistical measurement uncertainties.

The results of both the flux and the concentration measurements are presented in Ch. 4. This chapter includes a brief description of the shapes of the wakes under different flow conditions in Sec. 4.1. Both concentration and flux results are compared to the model derived in Ch. 2.

Ch. 5 contains everything about the measurements done with real air bubbles. The chapter starts with an overview in Sec. 5.1 over the most important models used for the describing the flotation process: the particle-bubble encounter, the attachment of the particle to the gas-liquid interface, and a possible detachment due to strong forces exerted on the already attached particle. Due to the extensive amount of literature in the field of flotation, this theoretical overview cannot be complete. Based on the discussion of the turbulent particle encounter in Sec. 5.1.1, the small formula for the increase in covered surface area is developed in Sec. 5.1.4.

For these measurements, a smaller facility described in Sec. 5.2.1 was built. Essentially, the experiment measures the increase in surface area covered by particles on a semi-spherical bubble, a shape that is a special case of a spherical cap as a result of the near pipe walls, and as such it is a reasonably stable object that allows to do reproducible measurements. The experiment itself and the methods used for data analysis are described in Sections 5.2.2 and 5.2.3. The results of these measurements are presented in Sections 5.2.4 and 5.2.5, including a qualitative description of the observations made also for other bubble shapes than semi-spheres. These results are compared to the small model for the concentration build-up derived in Sec. 5.1.4.

Finally, Ch. 6 discusses the obtained results and the implications for the optimisation of the flotation process in industry. It compares the efficiency of both the wake entrainment and the particle attachment to the bubble surface based on the results obtained in the previous chapters. It also gives ideas for further research on this topic, and discusses possible improvements to the experiments and methods used throughout this work.

2 Theoretical Background and a Model for Particle Entrainment

2 Theory and Entrainment Model

The aim of this work is to derive a model for predicting the concentration increase in the near-wake of a spherical cup over the outer flow. The model output — the concentration increase — should be a function of the flow properties and the particle properties only, because these properties are known a-priori and/or can be estimated from empirical correlations. This restriction is required if the model is useful for predicting the efficiency of particle flotation due to the effect of entrainment, as more complicated or very specific flow parameters are typically not known for flows in industrial processes. Summarising the requirements, the derivation of the model requires

- a formula for the local eulerian particle phase velocity as a function of the local fluid velocity field,
- and a sufficiently simple geometry for the flow field in the near-wake of a spherical cap, which potentially can also be used to describe the wake of a rising spherical-cap bubble.

The formula for the particle phase velocity can be obtained from the theory of a sphere immersed in a fluid, and this line of thought is presented in the first part of this chapter, Sec. 2.1. Starting from Newton's second law, the forces acting on the sphere can be derived if the sphere is small and so is its velocity relative to the fluid (small Reynolds number). Combining these forces yields an equation of motion for the immersed sphere, and a simplified version of it can be obtained by an analysis of the magnitude of the contributing terms. This simplified equation of motion is the *weak-inertia approximation* described in Sec. 2.1.4.

The model for the near wake is briefly described in Sec. 2.2. It is based on a spherical geometry describing the spherical cap and its wake, and a potential flow around it. It therefore fulfills the requirement for simplicity. Based on it and the weak-inertia approximation, Sec. 2.3 contains the derivation of the formula for the wake entrainment.

In the recent years, dispersed multiphase flows have been the topic of ongoing research, as the theses of Evans (2013); Zahnnow (2010); Mazzitelli (2003); van Haarlem (2000) and many others show. Each of these theses introduces the theory in similar ways but yet to a different extend and level of detail; the aim in this work is to stretch a complete arc from the foundations to the equation of motion used for our model's

derivation, and to discuss in detail the conditions for the validity of the simplifications made.

2.1 Single Particle Dynamics: A Sphere in a Fluid

The first part of this section gives an overview over the theoretical descriptions of a small spherical body immersed in a fluid; from Newton's second law over the contributing forces to the best-known equation of motion. The weak-inertia approximation, a simplified version of the equation of motion for low Reynolds numbers, is introduced in the following as it forms the basis for the description of the motion of the particulate phase in a turbulent fluid.

2.1.1 Fundamental Theory

Suspensions are in general described as a system consisting of a *continuous phase*, i.e. the fluid (liquid or gas) that occupies a certain domain, and a *dispersed phase*, which represents the inclusions (typically objects of a solid material and different sizes and shapes, but liquid drops or small gas bubbles are also possible) that are enclosed by the fluid. The term *continuous* implies that the fluid is usually not described by the interaction of atoms or molecules, but as a continuum; a simplification that is valid when the mean inter-molecular distance is small compared to the characteristic size of flow features. For the dispersed phase it is often assumed that the inclusions have sufficiently stable shapes and that they can be described by a single size parameter (an effective diameter); in other words, they are usually described as small solid spheres.

The definition above is more a necessary condition than a sufficient one, based on the necessity to simplify the system to a degree that makes it treatable. Exceptions exist to all constraints given above: for small aerosols in gases (Friedlander, 2000), the characteristic size is of the order of (or even significantly smaller than) the molecular free path length. The size of the dispersed particles is usually neither constant nor is their shape simple, particle agglomerates exhibit very complex or even fractal shapes (Zahnou *et al.*, 2011). Particles tend to agglomerate due to (gentle) collisions and form larger clusters. These clusters can also break up into smaller ones if there are strong shear forces in the flow, or again due to collisions, now at higher kinetic energies. Liquid

2 Theory and Entrainment Model

and gaseous inclusions are even more complex; additionally to break-up and coalescence, they must be described by a continuum with an appropriate boundary condition at the interface. However, when the viscosity of the dispersed phase is high compared to the viscosity of the continuous phase and surface tension is dominating all other body and pressure forces, the equilibrium shape is approximated by a sphere and disturbances are strongly damped. Rain drops $\leq 1\text{mm}$ (or any other liquid drop with a vanishing Weber number) are the ideal example for the definition above (Beard & Chuang, 1987).

Despite the mentioned constraints, the dissipative nature of fluid flows allows to treat dispersed particles as point masses independently of their actual shape, if a condition for the size of the particle is fulfilled. Small-scale fluctuations in fluid flows are strongly damped by viscosity for $Re \ll 1$, such that the flow at these scales can solely be described by the balance of viscous and pressure forces

$$\mu\Delta\mathbf{u} = \nabla p. \quad (2.1)$$

The *Stokeslet* is a solution of this equation for a point at the origin moving with a velocity relative to the fluid velocity \mathbf{u}_∞ infinitely far away from the origin. Independently of the shape of the particle, the Stokes flow solution converges to the solution of the sphere for distances sufficiently large compared to the effective diameter of the particle. Furthermore, the effective diameter itself can be defined by the diameter of a sphere that creates the same flow in the far field. Consequently, all particles can be described by spheres if their effective diameter is small enough that the flow around it can be treated as Stokes flow, i.e. if it is smaller than the smallest turbulent scale in the flow.

The time-evolution of mass and momentum density of the continuous phase is described by the continuity equation and Newton's second law

$$\frac{\partial\rho_F}{\partial t} = -\nabla \cdot (\rho_F\mathbf{u}_F) \quad (2.2a)$$

$$\begin{aligned} \rho_F\frac{D\mathbf{u}_F}{Dt} &= \nabla \cdot \left(-p\mathbb{1} + \mu \left(\nabla\mathbf{u}_F + \nabla\mathbf{u}_F^T - \frac{2}{3}\mathbb{1}\nabla \cdot \mathbf{u}_F \right) + \zeta\mathbb{1}\nabla \cdot \mathbf{u}_F \right) \\ &= \nabla \cdot \boldsymbol{\sigma} \end{aligned} \quad (2.2b)$$

2.1 Single Particle Dynamics: A Sphere in a Fluid

in the most general form for a viscous fluid (Landau & Lifshitz, 1987). The shear viscosity μ (second order tensor describing the resistance of a fluid to shear deformations, often simply called viscosity) and the second or volume viscosity ξ (can be a vector) are in general not constant in space and depend on the pressure p and on temperature. The differential operator D/Dt represents the total derivative after time here; it should not be confused with the Lagrangian time derivative d/dt later in this chapter. For an incompressible Newtonian fluid with constant viscosity, the stress tensor is given by

$$\boldsymbol{\sigma} = -p\mathbb{1} + \boldsymbol{\mu}(\mathbf{u}_F + \mathbf{u}_F^T) \quad (2.3)$$

and Eq. (2.2b) can be simplified to the well-known Navier-Stokes equation

$$\rho_F \frac{D\mathbf{u}_F}{Dt} = -\nabla p + \mu\Delta\mathbf{u}_F. \quad (2.4)$$

Eq. (2.1) can be obtained from Eq. (2.4) in the limit of vanishing Reynolds number $\text{Re}_P = \rho_F|\mathbf{v}_P - \mathbf{u}_{F,\infty}|d_P/\mu_F$ (here the definition of the particle Reynolds number is used).

The motion of the spherical particle (now in the sense of a Lagrangian time derivative) with three translational and three rotational degrees of freedom is described by the system

$$\frac{d\mathbf{x}_P}{dt} = \mathbf{v}_P \quad (2.5a)$$

$$m_P \frac{d\mathbf{v}_P}{dt} = \iint_{\partial V_P} \boldsymbol{\sigma} d\mathbf{S} + \sum \mathbf{F}_{\text{ext}} \quad (2.5b)$$

$$I_P \frac{d\boldsymbol{\omega}_P}{dt} = \iint_{\partial V_P} (\mathbf{x} - \mathbf{x}_P) \times (\boldsymbol{\sigma} d\mathbf{S}) + \sum \mathbf{M}_{\text{ext}}, \quad (2.5c)$$

with the particle mass m_P and its moment of inertia I_P . The external forces \mathbf{F}_{ext} and moments \mathbf{M}_{ext} represent all the interactions of the particle with external fields and/or collisions.

The coupling from the particle to the fluid is included by enforcing the appropriate (Dirichlet or von-Neumann) boundary condition to Eq. (2.2) at the boundary of the particle. Including all contributions from particle-particle collisions (both direct collisions and hydrodynamic interactions by the change of the flow field due to the presence of the other particle are possible), the system is said to be in

2 Theory and Entrainment Model

the *four-way coupling* regime. In the case of a high volume fraction of suspended particles, this leads to an effective chemical potential (see Seiter & Alder, 1978): particles in a zone with a high concentration have a preference to move into regions with low concentrations due to the higher chance of collisions.

The system consisting of Equations (2.2) and (2.5) can be further simplified if it is sufficiently dilute (low volume load $V_P/V_F = \Phi \ll 1$) that particle-particle collisions can be neglected (*two-way coupling*). Furthermore, if all friction forces between the particles and the fluid are so small that the momentum of a sufficiently large ($> d_P$) fluid element is not significantly changed by the presence of the particle (low mass load $\Phi\rho_P/\rho_F \ll 1$, weak external fields), then the fluid flow can be considered to be undisturbed by the dispersed phase (*one-way coupling*). In terms of transport, the dispersed phase is then called a *passive scalar*, in contrast to an *active scalar* that interacts with the transporting continuous phase in the two- and four-way coupling regime. This terminology is typically used to describe scalar fields like dye concentrations (passive scalar) or temperature (active scalar). The analogy here is that the particle concentration (or alternatively probability density to find a particle at a certain place) is fully determined by the advection of the fluid. It should be mentioned that the particle velocity — though being a (non-linear) function of the fluid velocity — is in general not solenoidal, even if the fluid is incompressible.

2.1.2 Forces in the Point Particle Approximation

The solution of Eq. (2.5) requires the calculation of the surface integrals over the particle boundary. In the case of a spherical particle in a viscous flow and providing that the conditions for one-way coupling are fulfilled, these surface integrals can be directly computed from the analytical solutions of the flow field. The evaluated integrals will then be functions of the fluid velocity, the particle velocity and angular velocity as well as their derivatives, and it can furthermore be decomposed into several contributing effects that are briefly discussed in the following.

Particle Drag

The equation for the drag of a solid sphere moving relative to a resting fluid

$$-F_{\text{dg}} = 6\pi\eta\rho_F R_P v_P \quad (2.6)$$

was derived in section IV of Stokes (1851) by neglecting the non-linear term from the stationary Navier-Stokes equation. As written by Landau & Lifshitz (1987) and Batchelor (1967), it was improved by Oseen¹ by linearising the advection term by $(\mathbf{u}_\infty \cdot \nabla)\mathbf{u}_F$. As Faxén (1922) points out, this is a necessary correction if the fluid domain is infinite, as in that case, for any finite value of the viscosity ν , a characteristic size l of a fluid volume element can be found that the Reynolds number $u_\infty l/\nu \not\ll 1$ as assumed by Stokes (1851).² Corrections of higher order, obtained from a perturbative expansion of the stream function, were first obtained by Goldstein (1929), and were later improved by Proudman & Pearson (1957) and Chester *et al.* (1969). These higher-order corrections were summarised by Veysey & Goldenfeld (2007), resulting in the formula for the drag

$$F_{\text{dg}} = -6\pi\eta R_P v_P \left(\underbrace{1}_{\text{Stokes}} + \underbrace{\frac{3}{8}\text{Re}}_{\text{Oseen}} + \underbrace{\frac{9}{40}\text{Re}^2 \log \text{Re}}_{\text{Proudman\&Pearson}} + \underbrace{\frac{9}{40}\text{Re}^2 \left(\gamma + \frac{5}{3} \log 2 - \frac{323}{360} \right) + \frac{27}{80}\text{Re}^3 \log \text{Re} + \mathcal{O}(\text{Re}^3)}_{\text{Chester \& Breach}} \right), \quad (2.7)$$

with the Euler constant γ . Veysey & Goldenfeld (2007) furthermore present a comparison with experimental and numerical results which suggests that despite a better approximation for $\text{Re} < 0.3$, the higher-order corrections deviate stronger for $\text{Re} \geq 1$ than the Oseen correction.

¹Oseen, C.W. *Über die Stokes'sche Formel, und über eine verwandte Aufgabe in der Hydrodynamik*, Arkiv för matematik, astronomi och fysik, **6**, 29, (1910); this text was not available during the writing of this thesis.

²It is interesting to note that Faxén (1922) qualitatively attributes this to the development of a wake behind the sphere, something that delayed if the fluid domain is bounded by walls - the case studied in his work.

2 Theory and Entrainment Model

Likewise, the approach of using perturbation methods for solving this problem is strongly criticised by Liao (2002), as the underlying assumption of all perturbation methods is a small Reynolds number; a condition that will necessarily fail for values of Re beyond unity. This leads to the effect that for larger Re the Oseen formula is a better approximation than those including the higher-order terms. Liao (2002) therefore uses the homotopy analysis method to derive a tenth-order approximation to the drag formula that shows a surprisingly good agreement with experimental data for $Re < 30$. He however states that the order of this approximation is “not high enough to determine the convergence region of our drag formula”.³

Veysey & Goldenfeld (2007) spent more effort on the “terrible problem”⁴ by deriving the drag formula

$$F_{\text{dg}} = \rho_F u_F^2 R_P^2 \frac{4\pi(24 + 24Re + 8Re^2 + Re^3 + 4\exp(Re)(Re^2 - 6))}{Re(2(Re + 1) + \exp(Re)(Re^2 - 2))} \quad (2.8)$$

by the aid of renormalisation group methods, which is probably the best analytical approximation to the drag of a sphere for the interval $0.5 \leq Re \leq 50$ existing to this date. Their comparison with experimental data nevertheless indicates that — similarly to the conclusions of Liao (2002) — still further improvements are needed.

More recently, Guo (2011) completely questioned all the analytical approaches and suggested the use of semi-empirical drag formulae. This approach dates back to Rubey (1933) who — one should note the similarity with Oseen’s formula — postulated his widely used drag law as

$$C_D = \frac{\beta}{Re} + \alpha, \quad (2.9)$$

where $\alpha = 0.44 \pm 0.06$ is the asymptotic drag coefficient for high Re ,⁵ and $\beta = 24$ the Stokes result for low Re . Eq. (2.9) is a reasonable estimate for the drag of a sphere for $Re \leq 2 \cdot 10^5$.

³Liao (2002) however achieves a good matching by an ingenious choice of the auxiliary parameter of the homotopy analysis method.

⁴original quote of Veysey & Goldenfeld (2007).

⁵According to Guo (2011) a constant drag coefficient was already observed in experiments by Newton in 1687.

2.1 Single Particle Dynamics: A Sphere in a Fluid

Instead of the increasingly complicated drag formulae, it is often easier to use the Faxén theorem (Mazur & Bedeaux, 1974)

$$\mathbf{F}(\mathbf{r}, t) = \frac{6\pi\mu R_P}{4\pi R_P^2} \int_{\delta V} \mathbf{u}_F(\mathbf{r}, t) d\mathbf{A} \quad (2.10)$$

in the general case of an inhomogeneously moving fluid with known $\mathbf{u}_F(\mathbf{r}, t)$.

Bagchi & Balachandar (2004) analysed the effect of free-stream turbulence on the drag of a particle by means of surface integrals of shear stress and pressure induced by simulated turbulent velocity fields. For a sinking sphere in a turbulent fluid, there are two effects that influence the observed time-averaged drag, namely

- a decreasing settling velocity with increasing turbulence intensity due to the non-linearity of the drag on the velocity relative to the fluid,
- and the *preferential trajectory* effect, an increase in settling velocity as a result of settling particles having a higher probability to be found in downwash regions and avoiding zones with an upward motion.⁶

According to results of Bagchi & Balachandar (2004), there is no systematic dependency of the time-averaged drag of either the turbulent Reynolds number or the turbulence intensity. However, with particle sizes increasing the Komogorov length scale, the drag formula cannot capture the small-scale fluctuations that were observed in the DNS. Particles with a diameter of about $10\eta_K$ show a significant damping even in the low-frequency part of the spectrum. In this case, the point-particle approximation is not a valid model any more.

Acceleration of the Fluid

Following Batchelor (1967), the external acceleration of the fluid with force density $\mathbf{f} = D\mathbf{u}_F/Dt$ per unit mass gives a contribution $-\rho_F \mathbf{f} \mathbf{x}^T$ to the stress tensor if the accelerating force is constant over a subset

⁶This preferential trajectory effect was already described by Maxey (1987).

2 Theory and Entrainment Model

of the domain that is larger than the particle. Calculating the surface integral gives

$$\mathbf{F}_{\text{acc}} = -\rho_F V_0 \frac{D\mathbf{u}_F}{Dt}, \quad (2.11)$$

with the material derivative $D/Dt = \partial/\partial t + (\mathbf{u}_F \cdot \nabla)$.

Added Mass

The added or virtual mass of a body is a term used for describing the inertia of the fluid in the vicinity of the body. A change in momentum of the body therefore always requires a change of momentum of the fluid that is influenced by the body's motion, or in other words, a change in kinetic energy of the body requires a change in kinetic energy of the surrounding fluid. Following Batchelor (1967), the kinetic energy of a fluid surrounding a moving body without rotation can be written as

$$T = \iiint_V \frac{\rho_F}{2} C_{M,ij} u_{F,i} u_{F,j} dV. \quad (2.12)$$

The fluid momentum is therefore given by

$$p_i = \frac{\partial T}{\partial u_{F,i}} = \iiint_V \rho_F C_{M,ij} u_{F,j} dV, \quad (2.13)$$

and hence the resulting force due to a change of that momentum is

$$\mathbf{F}_{\text{am}} = \frac{d\mathbf{p}}{dt} = \rho_F V_0 C_M \frac{d\mathbf{u}_F}{dt}. \quad (2.14)$$

Batchelor (1967) also calls this force the *acceleration reaction*, and $C_{M,ij}$ the *coefficient of virtual inertia*. The added mass coefficient C_M is in general a tensor of second order and the product $\text{tr}(C_M)\rho_F V_0$ is the mass of the fluid that is displaced by the motion of the body. If the body is simultaneously accelerated by the fluid, its acceleration relative to the fluid at infinity is $\partial\mathbf{U}_\infty/\partial t - D\mathbf{u}_F/Dt$, and the expression in Eq. (2.14) changes accordingly. This is in accordance with the argumentation by Auton *et al.* (1988).⁷ The specific term for a spherical body was first derived by Basset (1888).

⁷Auton *et al.* (1988) point out that the difference in the fluid inertia should be proportional to $d\mathbf{v}_P/dt - D\mathbf{u}_F/Dt$ instead of $d(\mathbf{v}_P - \mathbf{u}_F)/dt$ in the work of Maxey

The History Force

While the added mass term describes the change of inertia in the surrounding fluid due to an acceleration of the immersed body (the flow pattern is not changed), the history term describes the contribution to this change in the flow pattern (Ahmadi & Goldschmidt, 1971). Gatignol (1983) and Maxey & Riley (1983) derive the term

$$\mathbf{F}_{\text{hist}} = 6\pi\mu R_P \int_0^t \frac{d(\mathbf{v}_P - \mathbf{u}_F)}{d\tau} \frac{d\tau}{\sqrt{\pi(t-\tau)}}, \quad (2.15)$$

and call it the Basset history term,⁸ as this term was first derived by Basset (1888)⁹ in an attempt to derive an equation of motion for a sphere in a viscous flow.

If the flow field can be described by a stream function Ψ , the history term arises from the time-dependency of the stream function $\partial\Psi/\partial t$ that has to fulfil the differential equation

$$D \left(D - \frac{1}{\nu} \frac{d}{dt} \right) \Psi = 0 \quad (2.16)$$

with

$$D = \frac{\partial^2}{\partial r^2} + \frac{\sin\theta}{r^2} \frac{\partial}{\partial\theta} \left(\operatorname{cosec}\theta \frac{\partial}{\partial\theta} \right), \quad (2.17)$$

as derived by Stokes (1851).

The history force is often small compared to the other contributions and is furthermore costly to compute numerically, as the velocity of the

& Riley (1983). Both terms are only equal if the sphere is accelerated from rest in a stagnant fluid, which was the case for which this term was derived first by Basset (1888). The correct term was however already used by Batchelor (1967) and also in the thesis of Then (1947). Nonetheless, the other term can still be found in recent literature, see e.g. Marchioli *et al.* (2007).

⁸It should be noted here that Ahmadi & Goldschmidt (1971), Maxey & Riley (1983) and Gatignol (1983) all use the term $d/dt(\mathbf{v}_P - \mathbf{u}_F)$ inside the integral, which is somewhat surprising as the difference in the total time derivatives is done for \mathbf{v}_P relative to the particle path and for \mathbf{u}_F relative to the fluid motion in case of the added mass.

⁹Vojir & Michaelides (1994) dedicate a short passage in their work to the origin of the history term: apparently, the term was derived already three years earlier in the works of Boussinesq (1885*a,b*), which were not available during the writing of this thesis, though.

2 Theory and Entrainment Model

whole trajectory must be kept in memory.¹⁰ Thomas (1992) however points out that it delivers a significant contribution near shocks, while Hjelmfelt & Mockros (1966) confirms its relevance for high accelerations in general. More computationally efficient methods have been proposed by van Hinsberg *et al.* (2011) and Michaelides (1992). The term becomes negligible again in the case of statistically stationary response,¹¹ and it is also often neglected compared to other terms for gentle changes in the velocities. Despite this zero-mean effect on the particle location, the history term has a significant effect on the diffusivity of particles in a turbulent flow; see Reeks & McKee (1984). It furthermore causes a stronger high-frequency response to fluctuations in the fluid velocity (Vojir & Michaelides, 1994). In the so-called *weak-inertia approximation* (Maxey, 1987), the Basset history term is not part of the equation of motion.

Hydrodynamic Lift

A lift force is in general the result of a non-zero circulation of the fluid around the sphere. This circulation can have several causes, therefore different problems were described in literature. The general lift force is given by Saffman (1992) as

$$\mathbf{F}_L = \iiint_V \rho(\mathbf{v} \times \boldsymbol{\omega}_F) dV \quad (2.18)$$

$$= \rho_F \mathbf{v}_P \times \iiint_{V_P} \boldsymbol{\omega}_F dV. \quad (2.19)$$

If the total circulation over the whole domain is zero, the integral can be done over the vorticity outside the sphere $V \setminus V_P$ instead of V_P . If the flow is quasi-2D, the famous *Kutta-Joukowski theorem*

$$\mathbf{F}_L = \rho_F \mathbf{v} \times \boldsymbol{\Gamma} \quad (2.20)$$

¹⁰Another numerical complication arises from the fact that the integrand is singular for $\tau \rightarrow t$. The integral is however well-defined as the derivation was done for a sphere accelerating from rest, i.e. $\lim_{\tau \rightarrow t} \mathbf{v}_P(\tau) = \mathbf{u}_F(t)$.

¹¹As shown by Ahmadi & Goldschmidt (1971), the integral effect of the Basset history term over a long time $t \rightarrow \infty$ of the motion is bounded by

$$|\mathbf{F}_{\text{hist}}| \leq \frac{2M}{\sqrt{t}}$$

with a positive constant M for bounded $\mathbf{w} = \mathbf{v}_P - \mathbf{u}_F$.

2.1 Single Particle Dynamics: A Sphere in a Fluid

with the total circulation $\Gamma = \iint_A \boldsymbol{\omega} dA$ is obtained, giving the lift per-unit-span of an airfoil profile.

In the viscous regime, the lift force acting on a freely rotating particle in the unbounded shear flow $\mathbf{u} = (\kappa z + U)\mathbf{e}_x$ was first analysed by Saffman (1965), who derived the relation

$$F_{L,z} = K_1 U R_P \underbrace{\left(\frac{\kappa R_P^2}{\nu} \right)^{1/2}}_{=\sqrt{\text{Re}_\kappa}} + \mathcal{O}(\nu^{-1/2}) \quad (2.21)$$

with the numerically determined constant $K_1 = 81.2$. The lift force can also be expressed as the function of some shear Reynolds number $\text{Re}_\kappa = \kappa R_P^2 / \nu$ that was introduced by Saffman (1965).¹² The lift force under shear flow of a sphere in contact with a solid wall was studied by Leighton & Acrivos (1985)¹³, who derived

$$F_{L,z} = K_2 (\kappa \mu R_P^2) \underbrace{\left(\frac{\kappa R_P^2}{\nu} \right)}_{=\text{Re}_\kappa} \quad (2.22)$$

with the numerically determined constant $K_2 = 9.22$. It should be noted that the lift is here proportional to Re_κ instead of $\sqrt{\text{Re}_\kappa}$ in the case of the unbounded shear flow.

A rotating body that is moving relative to a fluid¹⁴ will also experience a lift force normal to its translational velocity. Auton (1987) shows, by using a method developed by Lighthill (1956*a,b*, 1957) for

¹²Saffman (1965) also mentions that “no sideway force on a single rigid sphere can be derived on the basis of the creeping flow equations” $\nabla p = \nu \Delta \mathbf{u}$ with $\nabla \cdot \mathbf{u} = 0$, a result derived earlier by him (Saffman, 1956). This can easily be seen as the term $\Delta \mathbf{u}$ is identical to that of a uniform flow. Therefore, the advection term $(\mathbf{u} \cdot \nabla) \mathbf{u}$ must be included in the analysis.

¹³Leighton & Acrivos (1985) studied the causes for re-suspension of particles at particle Reynolds numbers of $\mathcal{O}(10^{-2})$. He concluded that the calculated lift force is “far too small to be of significance relative to the drag”, and that “the factors responsible for the observed re-suspension remain, therefore, to be identified”. This motivates the use of statistical models for the particle re-suspension based on an attractive potential and particles “borrowing” kinetic energy from the fluid to detach, see Sec. 5.1.3.

¹⁴This is the famous Magnus effect in ball sports.

2 Theory and Entrainment Model

weakly rotational flows that comply with $|\omega|R_P \ll \|\mathbf{v}_P - \mathbf{u}_F\|$, that this force can be written as

$$\mathbf{F}_L = C_L V_P \rho_F (\mathbf{v}_P - \mathbf{u}_F) \times \boldsymbol{\omega}_F, \quad (2.23)$$

with the lift coefficient $C_L = 1/2$ for a sphere and $V_P = \frac{4}{3}\pi R_P^3$. It should be noted that the general lift coefficient is “the combined effect of the rotationally and inertially induced forces” (Auton *et al.*, 1988) and is given by

$$C_L = \frac{1}{2}(1 + C_M) + C_{L\Omega} \quad (2.24)$$

in an inviscid rotational flow, where $C_{L\Omega}$ denotes the purely rotational contribution; see also Sec. 2.1.3.

Depending on the particle shape and the flow, the lift force can be orders of magnitude stronger than the drag. However, this is only the case for high Reynolds number flows (e.g. around airfoils) and is typically not the case for $Re \leq \mathcal{O}(1)$.¹⁵

The Faxén Force

As written by Mazur & Bedeaux (1974), Faxén derived in his thesis¹⁶ his well-known theorem for the force on a body

$$\mathbf{F} = \frac{6\pi\eta R_P}{4\pi R_P^2} \iint_{\partial S} \mathbf{u}_F(\mathbf{r}) dS \quad (2.25)$$

resting in a non-homogeneous stationary flow \mathbf{u}_F . The somewhat strange way of writing the constant factor in Eq. (2.25) shall indicate that the

¹⁵For many types of flows, though, the human mind seems to intuitively attribute certain effects to the wrong force: e.g. in rowing, the concept is widespread that the propulsion is realised by the drag of the blades in the water. However, it has been observed (see Kleshnev, 1999; Caplan & Gardner, 2007) that the blades leave the water at the end of the stroke (“release”) some distance in the direction of motion of the boat relative to the position of the start of the stroke (“catch”). It was also shown by William C. Atkinson using simulations that spherical blades, which minimise the lift compared to the drag, make very inefficient rowing blades (<http://www.atkinsopht.com/row/socrball.htm>).

¹⁶Faxén, H. *Der Widerstand gegen die Bewegung einer starren Kugel in einer zähen Flüssigkeit, die zwischen zwei parallelen ebenen Wänden eingeschlossen ist.* Arkiv för matematik, astronomi och fysik, **18** (1924); this work was not available during the writing of this thesis.

2.1 Single Particle Dynamics: A Sphere in a Fluid

force is proportional to the velocity averaged over the surface of the sphere; the denominator $4\pi R_p^2$ is a result of the normalisation with the surface area of the sphere. If the fluid velocity is developed into a Taylor series around the origin and inserted in Eq. (2.25), all odd terms of the series do not contribute due to the symmetry of a spherical body.¹⁷ All terms of even order will contribute though, resulting in a series for the force

$$\mathbf{F} = c_0 \mathbf{u}_F|_{\mathbf{x}=\mathbf{0}} + c_2 \frac{\partial^2}{\partial x_i \partial x_j} \mathbf{u}_F \Big|_{\mathbf{x}=\mathbf{0}} x^2|_{|\mathbf{x}|=R_p} + \mathcal{O}(x^4) . \quad (2.26)$$

The terms higher than second order are usually neglected, and the second-order term simplifies to $\propto \Delta \mathbf{u}_F$ due to the rotational invariance. The coefficients c_i for each term of the equation of motion depend on whether Eq. (2.25) was calculated as a surface or volume average; see Gatignol (1983).

The Faxén force is therefore the second-order correction to the fluid velocity, which is present in all terms of the equation of motion that contain \mathbf{u}_F . It is also a small contribution that can be neglected if the particle size is of the order of the Kolmogorov length scale and smaller. However, Calzavarini *et al.* (2009) showed that the second order correction for both the drag and the added mass term are important for obtaining realistic acceleration statistics from numerical simulations for neutrally buoyant particles that are larger than the Kolmogorov length scale.

External Forces

External forces contain all forces like gravity, electrostatic or magnetic fields. They also include forces that are only present near boundaries (see Magnaudet, 2003) like additional resistance due to thinning films, and all short-ranged attractive or repelling forces due to electrical double layers on interfaces and van-der-Waals forces. With the exception

¹⁷The approach of Faxén (1922) is somewhat different: he develops the pressure into spherical harmonics, and decomposes the velocities into a regular and a singular part in the origin plus a constant (the component of \mathbf{u}_∞). Solving this system by using the no-slip boundary conditions at the surface of the sphere, he obtains the correction

$$\pi R_p^3 \nabla p|_{\mathbf{x}=\mathbf{0}} ,$$

which gives the correct second order term by using the Stokes formula $\mu \Delta \mathbf{u} = \nabla p$.

of the additional resistance due to thinning films, these forces do not explicitly depend on the particle or fluid velocity (implicit dependence is possible if the external field is generated by charged and/or magnetised particles). Typically, they are modelled as conservative fields, and the contributing forces are calculated as the volume integral over the point-interaction of the particle material with the external field.

2.1.3 Equations of Motion for a Spherical Particle

Basset (1888) derived the first equation of motion containing the added mass and the history terms for a sphere that is accelerated from rest. This equation was further improved by the works of Boussinesq (1903) (see Zeytounian (2003) for a modern review of the book), and Faxén (1922) and Oseen (1927) extended it to what became later known as the BBO (Basset-Boussinesq-Oseen) equation. The extension of the problem to a sphere in a non-stagnant fluid was first done by Then (1947).¹⁸ Modern derivations from first principles were published almost simultaneously by Maxey & Riley (1983) and Gatignol (1983), which will be briefly discussed in the following.

For a creeping flow around a spherical particle with the no-slip boundary condition, Maxey & Riley (1983) gave a derivation of the equation

¹⁸This thesis written under the supervision of J.M. Burgers is certainly a hidden gem, as it also contains — besides the extension of the BBO equation to a moving fluid in chapter 4 — a first analysis of the diffusivity of particles in a turbulent flow in chapter 5 and 6, notwithstanding some corrections that were pointed out by Corrsin & Lumley (1956) and Reeks & McKee (1984).

2.1 Single Particle Dynamics: A Sphere in a Fluid

of motion

$$\begin{aligned}
 \frac{4}{3}\pi R_P^3 \rho_P \frac{d\mathbf{v}_P}{dt} &= \underbrace{\frac{4}{3}\pi R_P^3 (\rho_P - \rho_F) \mathbf{g}}_{\text{gravity}} - \underbrace{6\pi\nu\rho_F R_P \left(\mathbf{v}_P - \mathbf{u} - \frac{1}{6}R_P^2 \Delta \mathbf{u} \right)}_{\text{Stokes drag}} \\
 &\quad - \underbrace{\frac{2}{3}\pi R_P^3 \rho_F \left(\frac{d\mathbf{v}_P}{dt} - \frac{D\mathbf{u}}{Dt} - \frac{d}{dt} \left(\frac{1}{10}R_P^2 \Delta \mathbf{u} \right) \right)}_{\text{added mass}} \\
 &\quad + \underbrace{\frac{4}{3}\pi R_P^3 \rho_F \frac{D\mathbf{u}}{Dt}}_{\text{fluid acceleration}} \\
 &\quad - \underbrace{6\pi\mu R_P^2 \int_0^t \frac{d/d\tau \left(\mathbf{v}_P - \mathbf{u} - \frac{1}{6}R_P^2 \Delta \mathbf{u} \right)}{\sqrt{\pi\nu(t-\tau)}} d\tau}_{\text{Basset history}}
 \end{aligned}$$

that is valid for vanishing particle Reynolds number ($Re = R_P |\mathbf{v}_P - \mathbf{u}_F|/\nu_F \ll 1$) and small velocity gradients ($(R_P^2/\nu_F)\nabla\mathbf{u}_F \ll 1$) in the continuous phase. Additionally, the size of the particle must be small compared to the length scale L_F of variations in the flow ($R_P/L_F \ll 1$).

Gatignol (1983)¹⁹ published a derivation that also includes the rotational motion. Using the dimensionless time $\tau = (R_P^2/\nu_F)t$, both equations can be written as

$$\begin{aligned}
 m_P \frac{d\mathbf{v}_P}{d\tau} &= 6\pi\eta R_P \left((\mathbf{v}_P - \overline{\mathbf{u}_F^S}) + \frac{1}{9} \left(\frac{d\mathbf{v}_P}{d\tau} - 3 \frac{d\overline{\mathbf{u}_F^V}}{d\tau} \right) \right. \\
 &\quad \left. + \int_{-\infty}^{\tau} \left(\frac{d\mathbf{v}_P}{d\tau'} - \frac{d\overline{\mathbf{u}_F^S}}{d\tau'} \right) \frac{d\tau'}{\sqrt{\pi(\tau - \tau')}} \right) + \sum \mathbf{F}_{\text{ext}} \quad (2.27)
 \end{aligned}$$

¹⁹This work is almost uncited in literature, and has only recently gained some attention. It nevertheless presents the most complete (including rotation) and mathematically rigorous derivation of an equation of motion that can be found in the literature up to this date.

2 Theory and Entrainment Model

and

$$\begin{aligned}
 I_P \frac{d\boldsymbol{\omega}_P}{d\tau} = & 8\pi\eta R_P^3 \left((\boldsymbol{\omega}_P - \overline{\boldsymbol{\omega}_F^S} - \frac{1}{15} \frac{d\overline{\boldsymbol{\omega}_F^V}}{d\tau} \right. \\
 & \left. + \frac{1}{3} \int_{-\infty}^{\tau} \left(\frac{d\boldsymbol{\omega}_P}{d\tau} - \frac{d\overline{\boldsymbol{\omega}_F^S}}{d\tau} \right) \left(\frac{1}{\sqrt{\pi(\tau - \tau')}} - e^{\tau - \tau'} \operatorname{erfc}\sqrt{\tau - \tau'} \right) d\tau' \right) \\
 & - \sum \mathbf{M}_{\text{ext}} , \quad (2.28)
 \end{aligned}$$

with the volume-averaged and surface-averaged undisturbed flow velocities $\overline{\mathbf{u}_F^V}$ and $\overline{\mathbf{u}_F^S}$ respectively. The Taylor series for the fluid velocity, including all the Faxén correction terms, is also given by Gatignol (1983). Following again the argumentation of Auton *et al.* (1988), the time-derivatives for the fluid velocity should be $D/D\tau$. The advantage of these equations over Eq. (2.27) is that the generalisation to arbitrary body shapes is simply done by the change of the integration volume or surface for determining the fluid velocity. The equations derived by Gatignol (1983) therefore represent the general equation of motion for an arbitrarily shaped body in the creeping flow regime.

Contrary to the creeping flow assumption Equations (2.27) to (2.28) are based on, Auton *et al.* (1988) derived an equation of motion for an inviscid, unsteady and non-uniform rotational velocity field. They assume that the rate of strain over the particle's dimensions is small compared to the relative velocity $\boldsymbol{w} = \mathbf{v}_P - \mathbf{u}_F$, thereby defining the small parameter

$$\epsilon = R_P \frac{\|\nabla \mathbf{u}_0\|}{w} \ll 1 , \quad (2.29)$$

and require furthermore that the time for changing \boldsymbol{w} is small compared to the time a fluid element needs to pass the particle

$$\left| \frac{\partial \boldsymbol{w}}{\partial t} \right| \ll \frac{w^2}{R_P} . \quad (2.30)$$

Under these assumptions, the force on a body becomes

$$\mathbf{F} = \rho_F V_P \left[(1 + C_M) \frac{D\mathbf{u}_F}{Dt} - C_M \frac{d\mathbf{v}_P}{dt} + C_L \boldsymbol{\omega}_F \times (\mathbf{v}_P - \mathbf{u}_F) \right] , \quad (2.31)$$

with the added mass coefficient $C_M = 1/2$ and the lift coefficient $C_L = (1 + C_M)/2 + C_{L\Omega} = 1/2$ for a sphere (Auton (1987), and where $C_{L\Omega}$

is the rotational lift coefficient. The accuracy of Eq. (2.31) is of first order in ϵ .

2.1.4 Weak-Inertia Approximation

The weak-inertia approximation

$$\mathbf{v}_P = \mathbf{u}_F + \tau_P \alpha \mathbf{g} + \tau_P (\beta - 1) \left(\frac{D\mathbf{u}}{Dt} \right), \quad (2.32)$$

is derived from Eq. (2.27) (Maxey, 1987)²⁰ and can be seen as a first-order approximation for small particle response times $\tau_P = \frac{R_P^2}{3\nu_F\beta}$, $\beta = \frac{3\rho_F}{2\rho_P + \rho_F}$, (smaller than the smallest time scales in the flow τ_F). Eq. (2.32) also defines a velocity field \mathbf{v}_P for the dispersed phase if \mathbf{u}_F is given, with $\nabla \cdot \mathbf{v}_P \neq 0$ in general. The interpretation of the particle velocity \mathbf{v}_P as the Eulerian phase velocity is not without problems, though. It neglects the possibility that two particles at the same point can have different velocities at different times; therefore, the stationary velocity field does not exist. Even in the non-stationary case, a collision-free point particle model would allow that a fast particle catches up on a slower one, resulting in two particles with different velocities at the same point and time. The latter constraint is fulfilled by the weak-inertia assumption, and Eq. (2.32) must be interpreted as a stochastic PDE with stochastic variables \mathbf{v}_P and \mathbf{u}_F that allows the treatment of stationary-state solutions.

The benefit of the weak-inertia approximation lies in the fact that an expression for the particle concentration can be obtained for a given stationary incompressible flow field. The basic idea comes from the famous Einstein paper on the Brownian motion (Einstein, 1905): “The state of dynamic equilibrium [...] can be conceived as a superposition of two processes proceeding in opposite directions, namely

1. a motion of the suspended substance under the influence of the force K which is exerted on each suspended particle,

²⁰Maxey (1987) uses a slightly different equation of motion in his paper; the added mass term is written as

$$\frac{d}{dt}(\mathbf{v} - \mathbf{u}),$$

contrary to the argumentation of Auton *et al.* (1988), and therefore his parameter R is defined differently to the β used in this work

2 Theory and Entrainment Model

2. a process of diffusion, which is to be conceived as the result of the random motions of the particles due to thermal molecular motion.”

The dynamic flux balance is taken here by analogy to Einstein’s idea between the convective transport of particles and the turbulent diffusive transport

$$0 = \rho_P \mathbf{v}_P - \nu_P \nabla \rho_P, \quad (2.33)$$

which can be rearranged to

$$\Delta \log \rho_P = \operatorname{div} (\nu_P^{-1} \mathbf{v}_P) = \operatorname{div} (\nu_P^{-1} (\mathbf{u}_F + \tau_P (\beta - 1) ((\mathbf{u}_F \cdot \nabla) \mathbf{u}_F - \mathbf{g}))) \quad (2.34)$$

by dividing by ρ_P , multiplying by the inverse of the diffusion tensor ν_P^1 and taking the divergence. As the diffusivity ν_P is a symmetric positive-definite matrix, its inverse exists and Eq. (2.34) can be solved by the Poisson integral

$$\rho_P = \exp \left(\iiint_V \frac{\nabla \cdot (\nu_P^{-1}(\mathbf{r}') \mathbf{v}_P(\mathbf{r}'))}{|\mathbf{r}' - \mathbf{r}|} d\mathbf{r}' \right). \quad (2.35)$$

Eq. (2.35) is an explicit function of the particle density in the domain as a function of the particle phase velocity. Together with Eq. (2.32), an explicit relation between the particle concentration and the fluid velocity is available.

It should be noted that there is no stationary state for the particle concentration if the fluid velocity field \mathbf{u}_F is laminar ($\nu_P = 0$). The concentration increases unboundedly at certain points where $\nabla \cdot \mathbf{v}_P < 0$. This can be solved by introducing a molecular (Brownian) diffusivity flux $D_m \nabla \rho_P$ into the continuity equation.

Eq. (2.33) is a consequence of the continuity equation for the dispersed phase.²¹ However, in a simple continuum model, the total particle flux is not necessarily zero. The continuity only implies that the longitudinal component of the flux

$$\mathbf{j}_P = \rho_P \mathbf{v}_P - \nu_P \nabla \rho_P = \underbrace{\nabla \Phi}_{\text{longitudinal component}} + \underbrace{\nabla \times \mathbf{A}}_{\text{transversal component}} \quad (2.36)$$

²¹The momentum balance is violated in the one-way coupling regime for the dispersed phase, because it is negligible compared to the momentum of a fluid element of sufficient size.

is zero. A constraint for the transverse component can be obtained from the dissipative nature of fluid flows, or the bound energy spectrum $\hat{E}(\mathbf{k})$ of the turbulent fluid. As a consequence, both the velocity spectrum $\hat{\mathbf{u}}(\mathbf{k})$ and the vorticity spectrum $\hat{\boldsymbol{\omega}}(\mathbf{k}) = \mathbf{k} \times \hat{\mathbf{u}}(\mathbf{k})$ are bound (they converge sufficiently fast in the limit $k \rightarrow \infty$), and thereby also the transverse component of the flux $\rho_P \mathbf{v}_P$ is bound in the weak inertia limit. The transverse component is hence constant in a control volume of sufficiently small dimension. It was now shown that by requiring rotational symmetry (SO(3))²² “the gauge field of a fluid flow coincides with the vorticity” (Kambe, 2003). Together with the local constant (particle phase) vorticity field²³ at small scales, the gauge invariance implies that the transverse component has no influence here; i.e. the sum of the local particle fluxes can be set zero.

2.2 A Model for the Near-Wake

Dayan & Zalmanovich (1982) assume a bubble wake of spherical shape, which consists of a spherical-cap bubble with the rim at the polar angle θ_0 and the near wake occupying the rest of the volume of the sphere (see Fig. 2.1). They furthermore assume an irrotational flow around this sphere. Balancing gravity, Stokes’ drag and inertia, they derive the radial component of the particle slip velocity at the wake boundary as

$$v_r = \frac{2 R_P^2}{9 \mu} (\rho_P - \rho_F) g_z (\sin^2 \theta - \cos \theta). \quad (2.37)$$

Supposing that $N(R_P)$ is the concentration of particles with radius R_P in the wake, Dayan & Zalmanovich (1982) solved the differential equation

$$d^2 N(R_P) = - \frac{N(R_P)}{V_{\text{wake}}} v_r dA dt \quad (2.38)$$

using Eq. (2.37) and $dA = 2\pi R_{\text{wake}}^2 \sin \theta d\theta$, and derived

$$N(R_P, t) = N_0(R_P) \exp \left(-0.573 \frac{g R_P^2 (\rho_P - \rho_F)}{R_{\text{wake}} \mu} t \right). \quad (2.39)$$

²²The special orthogonal group SO(3) represents the group of rotations in three dimensions; it should be noted that it is only required that the laws of the system (the Lagrangian) obey this symmetry, not necessarily the domain itself.

²³The system of the particle phase should obey the same symmetries as the underlying fluid flow.

2 Theory and Entrainment Model

This equation describes the change in concentration of particles with radius R_P inside the wake over time.

Our model is based on the same assumptions. Dayan & Zalmanovich (1982) do not model a stationary state though. For buoyant particles ($\rho_P < \rho_F$), Eq. (2.38) would change to

$$d^2 N(R_P) = -\frac{N_{\text{ext}}}{V_{\text{wake}}} v_r dA dt \quad (2.40)$$

with some constant external particle concentration N_{ext} and a negative (inward) v_r . The solution to this equation is a linear increase in concentration with time. This can only be the case when diffusive fluxes can be neglected at all times t and for all concentration differences, as otherwise the particle concentration would grow without bounds. Adding diffusion to their model would add a term $D(R_P)(N(R_P) - N_{\text{ext}}(R_P))dA dt$ to the right side of equation Eq. (2.38), whose contribution can be neglected in the case studied by them. With increasing $N(R_P)$ for buoyant particles, this term will however retard and finally stop any growth of the particle concentration inside the wake. In our case, when the potential flow around a sphere is used to model the time-averaged flow around the bubble and its wake of an otherwise fully turbulent flow field, the diffusion constant $D(R_P)$ is so large that the system reaches a stationary state with only a small change in particle concentration inside the wake.

2.3 A Model for Particle Entrainment

In this section, the model for the particle entrainment is derived, based on the weak-inertia approximation and the model of Dayan & Zalmanovich (1982) for the near-wake of the spherical cap.

2.3.1 Particle Entrainment in a Spherical-Cap Wake

The model derived in the following assumes a balance between the inertia-induced particle flux and turbulent diffusion from the wake region to the surrounding fluid. The inertia-induced particle flux is the result of accelerations in the time-averaged flow, which is modelled as a stationary irrotational flow around the spherical bubble-wake. This model (see Fig. 2.1) was originally proposed by Dayan & Zalmanovich

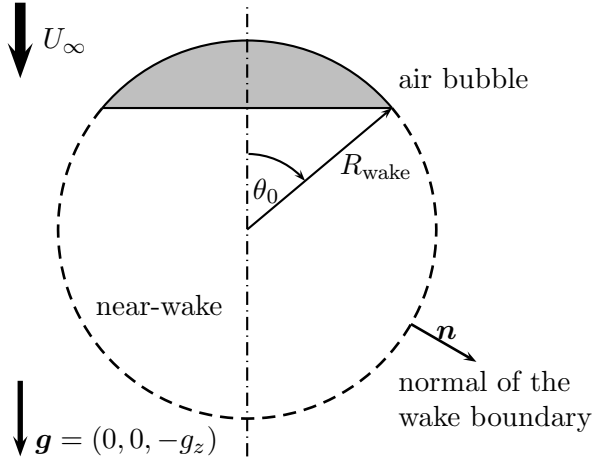


Figure 2.1: Spherical model for the near-wake behind a spherical-cap gas bubble according to Dayan & Zalmanovich (1982)

(1982). The diffusive particle transport is the result of concentration gradients and the turbulent velocity fluctuations. In other words, the model predicts the expectation value of the particle concentration in the wake of a spherical-cap bubble as a function of the statistical properties of the flow.

The equation of motion for a sufficiently small spherical particle in a fluid is given by Maxey & Riley (1983) (see also: Gatignol, 1983; Mei, 1996) and is discussed in the previous section. The Faxén correction is neglected in the Stokes drag and in the added mass term, the Basset history term and other possible forces (such as the lift force and forces due to pressure gradients). This is appropriate when the particle diameter is very small in comparison to the characteristic length scale of the velocity gradients in the flow (Saffman, 1965; Auton, 1987; Auton *et al.*, 1988; Thomas, 1992; Calzavarini *et al.*, 2009). We thus retain a simplified expression of the Maxey-Riley equation for the velocity \mathbf{v} of a small particle in a fluid that has a velocity field \mathbf{u} :

$$\frac{d\mathbf{v}}{dt} = \alpha \mathbf{g} - \frac{1}{\tau_P} (\mathbf{v} - \mathbf{u}) + \beta \frac{D\mathbf{u}}{Dt}, \quad (2.41)$$

2 Theory and Entrainment Model

with:

$$\alpha = 2 \frac{\rho_P - \rho_F}{2\rho_P + \rho_F} = 1 - \beta, \quad \text{and:} \quad \beta = \frac{3\rho_F}{2\rho_P + \rho_F}, \quad (2.42)$$

and a particle response time τ_P , defined as

$$\tau_P = \frac{R_P^2 (2\rho_P + \rho_F)}{9\nu\rho_F} = \frac{R_P^2}{3\nu\beta}, \quad (2.43)$$

where R_P is the particle radius, ρ_P the density of the particle, and ρ_F and ν the density and kinematic viscosity of the fluid respectively. The added-mass term in (2.41) is in accordance with the argumentation of Auton *et al.* (1988).

For small particle response times τ_P , the particle experiences a small slip velocity $\mathbf{v} - \mathbf{u}$ such that it undergoes nearly the same acceleration as a fluid element, i.e. $d\mathbf{v}/dt - D\mathbf{u}/Dt \cong \mathbf{0}$. This assumption is valid even for a turbulent flow provided that the particle response time τ_P is much smaller than the Kolmogorov time scale τ_K of the turbulent flow. Consequently, the averaged particle velocity can be obtained from (2.41) as

$$\langle \mathbf{v}_P \rangle_t = \langle \mathbf{u} \rangle_t + \tau_P \alpha \mathbf{g} + \tau_P (\beta - 1) \left\langle \frac{D\mathbf{u}}{Dt} \right\rangle_t, \quad (2.44)$$

where $\langle \dots \rangle$ denotes an ensemble average over many realisations of the flow. ²⁴

By means of the Reynolds decomposition $\mathbf{u}_F = \langle \mathbf{u}_F \rangle + \mathbf{u}'_F$, the fluid velocity is decomposed into a time-averaged component $\langle \mathbf{u}_F \rangle$ and a fluctuating component \mathbf{u}'_F with zero mean. This finally gives the time-averaged equation

$$\langle \mathbf{v}_P \rangle = \langle \mathbf{u} \rangle + \tau_P \alpha \mathbf{g} + \tau_P (\beta - 1) \left[\langle (\langle \mathbf{u}_F \rangle \cdot \nabla) \langle \mathbf{u}_F \rangle \rangle + \langle (\mathbf{u}'_F \cdot \nabla) \mathbf{u}'_F \rangle \right]. \quad (2.45)$$

The turbophoresis term $\langle (\mathbf{u}'_F \cdot \nabla) \mathbf{u}'_F \rangle$ is omitted from the following part of the derivation; it is treated as an additional contribution to the particle flux in Sec. 2.3.5.

It is now assumed that the time-averaged flow around the bubble and its wake in a frame of reference moving with the spherical-cap bubble

²⁴In practice, the flow conditions and turbulence statistics are assumed to be stationary, and $\langle \dots \rangle$ is determined by means of a time-average.

at a constant velocity U_∞ is described by a stationary potential flow around a sphere with a radius R_{wake} ; see Fig. 2.1. Neglecting gravity, it follows from (2.44) that a particle moving tangentially to the boundary of the sphere that defines the mean wake is experiencing a slip velocity with a radial component

$$\begin{aligned} \langle v_r \rangle|_{r=R_{\text{wake}}} &= \tau_P (\beta - 1) \left. \frac{1}{2} \frac{\partial}{\partial r} \langle u_\theta \rangle^2 \right|_{r=R_{\text{wake}}} \\ &= -\tau_P (\beta - 1) \frac{9U_\infty^2}{4R_{\text{wake}}} \sin^2 \theta, \end{aligned} \quad (2.46)$$

with: $\langle u_\phi \rangle = 0$,²⁵ $\langle u_r \rangle|_{r=R} = 0$, $\langle u_\theta \rangle|_{r=R} = \frac{3}{2}U_\infty \sin \theta$, and $\partial \langle u_\theta \rangle / \partial r|_{r=R} = -\frac{3}{2R}U_\infty \sin \theta$. The term $(\langle \mathbf{u}_F \rangle \cdot \nabla) \langle \mathbf{u}_F \rangle$ is simplified through the vector identity $(\mathbf{u} \cdot \nabla) \mathbf{u} = \frac{1}{2} \nabla u^2 - \mathbf{u} \times (\nabla \times \mathbf{u})$, where the last term can be omitted as we consider an irrotational flow. The radial component of the fluid velocity $\langle u_r \rangle$ is zero at the wake boundary (by definition), and the azimuthal component of the fluid velocity is zero due to rotational symmetry.

With Eq. (2.45), the time-averaged particle flux over the wake boundary is given by

$$\Phi_i = 2\pi \int_{\theta_0}^{\pi} \langle n_P \rangle|_{r=R_{\text{wake}}} \langle v_r \rangle|_{r=R_{\text{wake}}} R_{\text{wake}}^2 \sin \theta \, d\theta, \quad (2.47)$$

where $\langle n_P \rangle$ is the mean particle number density in the fluid. The integral is only calculated over the wake boundary, leaving out the region of the spherical-cap bubble; see Fig. 2.1. Assuming a constant particle number density $n_{P,\text{ext}}$ in the ambient fluid (and therefore over the boundary of the wake), we arrive at the following simplified relation for the inertia-induced particle flux:

$$\Phi_i = -\tau_P (\beta - 1) \frac{3\pi}{2} U_\infty^2 R_{\text{wake}} n_{P,\text{ext}} (2 - \cos^3 \theta_0 + 3 \cos \theta_0). \quad (2.48)$$

Here, the sign convention is that the flux is positive in the outward radial direction.

²⁵The velocity in the azimuthal direction u_ϕ is assumed to be zero; this dimension is therefore omitted in the following analysis.

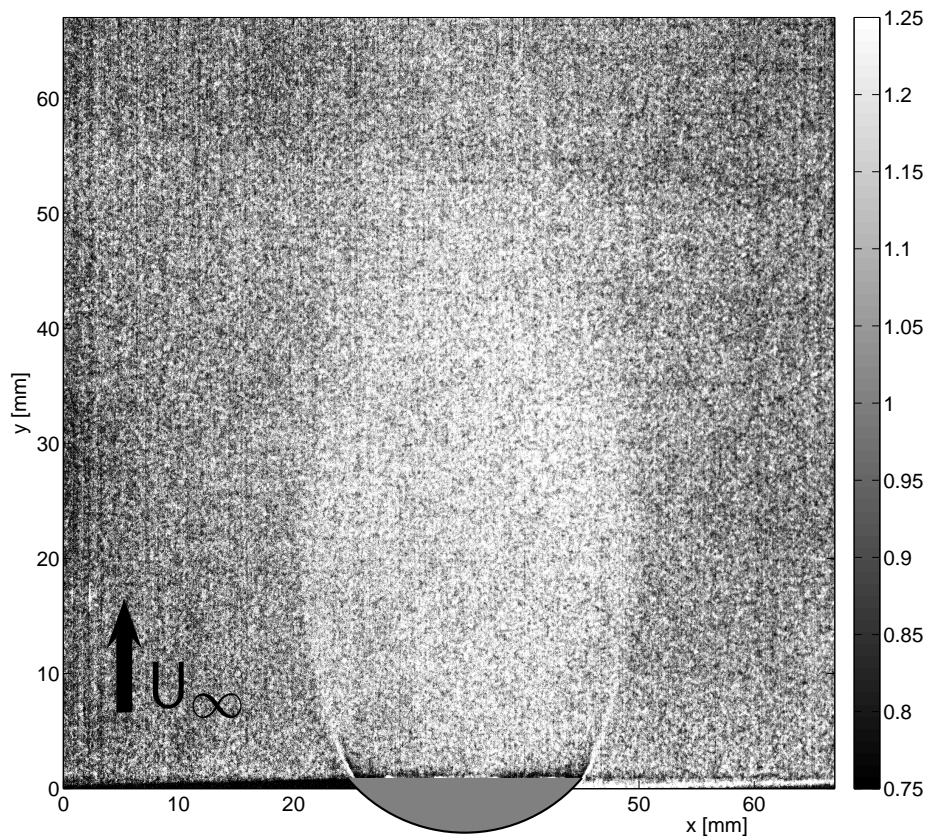


Figure 2.2: Measured particle concentration in the wake of a solid spherical cap, upward flow, corrected for inhomogeneous illumination and normalised by mean intensity. Note the local concentration increase in the free shear layers, the rather sharp boundary between the near wake and the outer flow, and the absolute concentration increase in the near wake.

2.3 A Model for Particle Entrainment

In a statistically stationary state, the inward inertia-driven flux is balanced by an outward flux due to turbulent diffusive particle transport with a diffusion coefficient D_P (see e.g. Hinze, 1975) through the bounding surface A of the wake, which is given by

$$\begin{aligned}\Phi_d &= \int_A D_P \nabla \langle n_P \rangle \cdot d\mathbf{A} \\ &\approx D_P \frac{n_{P,\text{wake}} - n_{P,\text{ext}}}{L_P} 2\pi R_{\text{wake}}^2 \int_{\theta_0}^{\pi} \sin \theta d\theta \\ &\approx C u_{\text{rms}} (n_{P,\text{wake}} - n_{P,\text{ext}}) R_{\text{wake}}^2 2\pi (\cos \theta_0 + 1).\end{aligned}\quad (2.49)$$

The sum of both contributions is zero in the stationary state. Here it is assumed that the diffusion process can be described by a gradient diffusion model. Furthermore, we assumed a uniform particle concentration $n_{P,\text{wake}}$ inside the wake and a uniform particle concentration $n_{P,\text{ext}}$ in the outer flow. This simplification is supported by experimental data, see Fig. 2.2. Hence, we can approximate the concentration gradient by the difference between these concentrations divided by a length scale L_P . In analogy to the turbulent momentum transport coefficient, the turbulent particle diffusivity coefficient $D_P = C u_{\text{rms}} L_P$ can be decomposed into the product of a velocity scale (here the scale of the turbulent velocity fluctuations u_{rms}), a length scale L_P , defined as the mixing length of the dispersed phase, and a constant C of order 1. It is assumed that the integral length scale L_P is the characteristic scale for both the particle concentration gradient and the momentum mixing length, and that L_P scales with R_{wake} . Both length scales are not necessarily identical, but any proportionality constant can be absorbed into the (unknown) constant C . This assumption however requires experimental validation. Balancing both fluxes, i.e. $\Phi_i + \Phi_d = 0$, and rearranging the terms gives the following expression for the ratio of the particle concentrations in the wake and in the external flow:

$$\frac{n_{P,\text{wake}}}{n_{P,\text{ext}}} - 1 = \frac{U_\infty}{u_{\text{rms}}} \frac{\tau_P (\beta - 1)}{R_{\text{wake}}/U_\infty} \frac{3f(\theta_0)}{4C}, \quad (2.50)$$

with:

$$f(\theta_0) = \frac{2 - \cos^3 \theta_0 + 3 \cos \theta_0}{1 + \cos \theta_0} = 2 + \cos \theta_0 - \cos^2 \theta_0, \quad (2.51)$$

2 Theory and Entrainment Model

which incorporates a Stokes number St , defined as

$$St = \frac{\tau_P(\beta - 1)}{R_{\text{wake}}/U_\infty} = \frac{\tau_P(\beta - 1)}{T}, \quad (2.52)$$

that characterises the trapping of the particle in the wake. The ratio of this characteristic Stokes number and the turbulence level $TL = u_{\text{rms}}/U_\infty$

$$St_{\text{mean}} = \frac{St}{TL} \quad (2.53)$$

is equivalent to the so-called “large eddy Stokes number” defined by Hardalupas *et al.* (1992). We use the term “mean flow Stokes number” here, as this parameter describes the scaling of the contribution of the time-averaged flow. The time $T = R_{\text{wake}}/U_\infty$ is the characteristic time scale for the wake; it only depends on the properties of the mean flow. The term U_∞/u_{rms} is the reciprocal of the relative turbulence level, and $f(\theta_0)$ is a geometrical factor that only depends on the polar angle of the edge of the spherical cap. For a spherical-cap gas bubble (with a large Weber number) the angle θ_0 is typically around 50° (see e.g. Wegener & Parlange, 1973), so that $f = 2.23$; completely ignoring the spherical cap, i.e. $\theta_0 = 0^\circ$, gives $f = 2$.

Given (2.52), we now define a modified particle response time

$$\tau_P^* = \tau_P(\beta - 1) = \frac{2R_P^2 (\rho_F - \rho_P)}{9\nu\rho_F}, \quad (2.54)$$

which is a measure for the response of the particles; it only depends on the properties of the dispersed phase. It should be noted that according to this definition, the characteristic Stokes number in (2.52) attains negative values for particles with a density that is larger than that of the surrounding fluid (for which $\beta < 1$).

2.3.2 The Influence of Gravity

In deriving Eq. (2.45) for calculating the radial slip velocity at the wake boundary, the gravity term in (2.44) was neglected. By balancing the gravity $\mathbf{g} = (0, 0, -g_z)$.²⁶ with Stokes drag on a moving spherical

²⁶The direction of gravity is here chosen according to the coordinate system of the rising bubble, see Fig. 2.1 For the comparison with the experimental data in Ch. 4, $\mathbf{g} = (0, 0, +g_z)$ will be used.

2.3 A Model for Particle Entrainment

particle, the radial component of the settling velocity, i.e.

$$v_{s,r} = -\tau_P \alpha g_z \cos \theta = \tau_P (\beta - 1) g_z \cos \theta, \quad (2.55)$$

induces an additional particle flux:

$$\begin{aligned} \Phi_g &= 2\pi \int_{\theta_0}^{\pi} n_{P,\text{ext}} \tau_P (\beta - 1) g_z \cos \theta R_{\text{wake}}^2 \sin \theta d\theta \\ &= \pi \tau_P (\beta - 1) g_z R_{\text{wake}}^2 n_{P,\text{ext}} (\cos^2 \theta_0 - 1). \end{aligned} \quad (2.56)$$

Comparing Eq. (2.48) and Eq. (2.56) gives

$$\frac{\Phi_g}{\Phi_i} = \frac{2(\cos \theta_0 - 1)}{3 \text{Fr}^2 (2 - \cos \theta_0)(1 + \cos \theta_0)}, \quad (2.57)$$

with the Froude number $\text{Fr} = U_\infty / \sqrt{g_z R_{\text{wake}}}$. The Froude number can be interpreted here as the ratio of the radial to the gravitational acceleration. Hence, the gravitational flux can be neglected if

$$\frac{3(2 - \cos \theta_0)(\cos \theta_0 + 1)}{2(1 - \cos \theta_0)} \text{Fr}^2 \gg 1. \quad (2.58)$$

Requiring that in a stationary case we have $\Phi_i + \Phi_g + \Phi_d = 0$, gives

$$\frac{n_{P,\text{wake}}}{n_{P,\text{exterior}}} - 1 = \frac{U_\infty}{u_{\text{rms}}} \frac{\tau_P (\beta - 1)}{R_{\text{wake}} / U_\infty} \frac{\tilde{f}(\theta_0, \text{Fr}^2)}{C}, \quad (2.59)$$

with a modified shape factor:

$$\tilde{f}(\theta_0, \text{Fr}^2) = \frac{3}{4}(2 + \cos \theta_0 - \cos^2 \theta_0) + \frac{1}{2 \text{Fr}^2} (\cos \theta_0 - 1). \quad (2.60)$$

The condition in Eq. (2.58) implies $\text{Fr}^2 \gg 0.107$ for $\theta_0 = 50^\circ$, i.e. $U_\infty \gg 0.11$ m/s for the spherical cap used in the experiments described in Chapters 3 and 4. The contribution to the flux due to gravitational settling to the mean transport therefore scales with $\text{St}/\text{Fr}^2 \text{TL} = \text{St}_{\text{mean}}/\text{Fr}^2$.

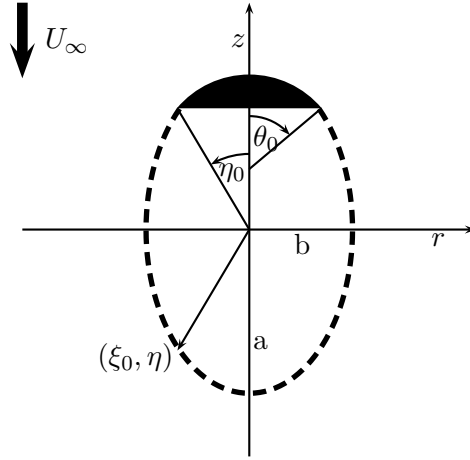


Figure 2.3: Coordinate system for the potential flow around a prolate ellipsoid with half axes $a = c \cosh \xi_0$ and $b = c \sinh \xi_0$; the spherical cap is defined by the polar angle of its rim θ_0 , which is situated at the angle η_0 of the elliptical coordinate system of the wake; a point at the wake boundary is given by the coordinates (ξ_0, η)

2.3.3 A Model for an Elliptical Wake

The experimentally measured velocity fields show that the wake does not have a spherical shape and that its boundary is better described by an ellipsoid of rotation. In the following the formula for the concentration increase is also derived for a potential flow around an ellipsoid. The derivation of a formula for the particle concentration in an elliptical wake follows the same approach as in Sec. 2.3.1. From the derivatives of the Stokes stream function of a potential flow around a prolate ellipsoid, the normal particle slip velocity at the wake boundary is calculated. The inertial particle flux follows by integration, likewise the diffusive and the gravitational fluxes. It should be noted that all dimensionless numbers are normalised with the major half axis a of the ellipse. The shape factors now depend on the eccentricity e of the elliptical wake.

The Stokes stream function for the potential flow around a prolate ellipsoid (Batchelor, 1967) in elliptical coordinates ξ, η (see Fig. 2.3) is

given by

$$\Psi = \frac{U_\infty}{2} c^2 \sin^2 \eta \left(\sinh^2 \xi - K \left(\cosh \xi + \sinh^2 \xi \log \tanh \frac{\xi}{2} \right) \right), \quad (2.61)$$

with

$$K = \frac{b^2}{ac + b^2 \log \left(\frac{a-c}{b} \right)} \quad (2.62)$$

and $e = c/a = \sqrt{a^2 - b^2}/a$. By analogy to Sec. 2.3.1, the slip velocity of a particle in direction of ξ at the boundary of the ellipsoid ($\xi = \xi_0$) is given by

$$v_{P,\xi}|_{\xi=\xi_0} = \tau_P(\beta - 1) \frac{1}{h_\xi} \frac{\partial}{\partial \xi} \frac{u^2}{2} \Big|_{\xi=\xi_0}, \quad (2.63)$$

because the velocity component u_ξ is zero at the boundary by definition. For the same reason $u^2 = u_\eta^2$ at the boundary, and one gets

$$\begin{aligned} \frac{1}{2h_\xi} \frac{\partial}{\partial \xi} u_\eta^2 &= \frac{1}{2h_\xi} \frac{\partial}{\partial \xi} \left(\frac{-1}{h_\xi r} \frac{\partial}{\partial \xi} \Psi \right)^2 \\ &= \frac{\Psi'}{h_\xi^3 r^2} \left(\Psi'' - \Psi' \left(\frac{1/2}{h_\xi^2} \frac{\partial h_\xi^2}{\partial \xi} + \frac{1}{r} \frac{\partial r}{\partial \xi} \right) \right) \end{aligned} \quad (2.64)$$

with the scale factor $h_\xi = c\sqrt{\sinh^2 \xi + \sin^2 \eta}$ and the radial distance to the z axis $r = c \sinh \xi \sin \eta$. The different terms are:

$$\frac{1/2}{h_\xi^2} \frac{\partial h_\xi^2}{\partial \xi} \Big|_{\xi=\xi_0} = \frac{c^2 \sinh \xi \cosh \xi}{c^2 \sinh^2 \xi + c^2 \sin^2 \eta} \Big|_{\xi=\xi_0} = \frac{ba}{b^2 + c^2 \sin^2 \eta}, \quad (2.65)$$

$$\frac{1}{r} \frac{\partial r}{\partial \xi} \Big|_{\xi=\xi_0} = \frac{\cosh \xi}{\sinh \xi} \Big|_{\xi=\xi_0} = \frac{a}{b}, \quad (2.66)$$

$$\frac{\partial}{\partial \xi} \Psi \Big|_{\xi=\xi_0} = \frac{U_\infty b c^3 \sin^2 \eta}{ac + b^2 \log \frac{a-c}{b}}, \quad (2.67)$$

and

$$\frac{\partial^2}{\partial \xi^2} \Psi \Big|_{\xi=\xi_0} = \frac{U_\infty a c^3 \sin^2 \eta}{ac + b^2 \log \frac{a-c}{b}}. \quad (2.68)$$

2 Theory and Entrainment Model

With these terms, the particle slip velocity normal to the wake boundary is given as

$$v_{P,\xi}|_{\xi=\xi_0} = f(e) \frac{\tau_P(\beta - 1)U_\infty^2 \sin^2 \eta}{a}, \quad (2.69)$$

with

$$f(e) = \frac{\sqrt{1 - e^2}e^6}{(e - (1 - e^2) \operatorname{artanh}(e))^2 (1 - e^2 \cos^2 \eta)^{5/2}}. \quad (2.70)$$

For $e \rightarrow 0$, Eq. (2.45) for a sphere is obtained. This can be seen by making use of the series expansion of $\operatorname{artanh}(e) = e + e^3/3 + \mathcal{O}(e^5)$, whereby the factor $f(e)$ becomes

$$\lim_{e \rightarrow 0} f(e) = \lim_{e \rightarrow 0} \frac{\sqrt{1 - e^2}e^6}{(e - (1 - e^2)(e + e^3/3 + \mathcal{O}(e^5)))^2 (1 - e^2 \cos^2 \eta)^{5/2}} = \frac{9}{4}. \quad (2.71)$$

The inertial flux can now be determined by integrating $v_{P,\xi}$ over the boundary of the wake, which gives

$$\begin{aligned} \Phi_i &= 2\pi \int_{\eta_0}^{\pi} \langle n_P \rangle_t |_{\xi=\xi_0} v_{P,\xi}|_{\xi=\xi_0} \sqrt{a^2 \sin^2 \eta + b^2 \cos^2 \eta} b \sin \eta d\eta \\ &= \pi \tau_P (\beta - 1) a U_\infty^2 n_{P,\text{exterior}} f_{\text{inertia}}(e) \end{aligned} \quad (2.72)$$

with

$$\begin{aligned} f_i(e) &= \frac{(1 - e^2)e^3}{(e - (1 - e^2) \operatorname{artanh}(e))^2} \left((e^2 + 1)(\operatorname{artanh}(e) + \operatorname{artanh}(e \cos \eta_0)) \right. \\ &\quad \left. - e \frac{\cos \eta_0 + 1}{2} \left(\frac{e + 1}{e \cos \eta_0 + 1} + \frac{e - 1}{e \cos \eta_0 - 1} \right) \right) \end{aligned} \quad (2.73)$$

and $\eta_0 = \arcsin\left(\frac{\xi}{2a\sqrt{1-e^2}}\right)$.²⁷ The diffusive flux over the boundary is

$$\begin{aligned} \Phi_d &= C u_{\text{rms}} (n_{P,\text{wake}} - n_{P,\text{exterior}}) 2\pi \int_{\eta_0}^{\pi} \sqrt{a^2 \sin^2 \eta + b^2 \cos^2 \eta} b \sin \eta d\eta \\ &= C u_{\text{rms}} (n_{P,\text{wake}} - n_{P,\text{exterior}}) \pi a^2 f_d(e), \end{aligned} \quad (2.74)$$

²⁷For conformity with the notation of Fan & Tsuchiya (1990), the base diameter of the spherical cap is denoted by the symbol ξ here; it should not be confused with the coordinate ξ of the elliptical coordinate system.

with

$$f_d(e) = \sqrt{1-e^2} \left(\sqrt{1-e^2} + \frac{\arcsin(e)}{e} + \cos \eta_0 \sqrt{1-e^2 \cos^2 \eta_0} + \frac{\arcsin(e \cos \eta_0)}{e} \right). \quad (2.75)$$

For $e \rightarrow 0$, Eq. (2.49) for a sphere is again obtained. The contribution of gravity results in a flux

$$\begin{aligned} \Phi_g &= 2\pi \int_{\eta_0}^{\pi} -n_{P,\text{exterior}} \tau_P \alpha \frac{g_z \cos \eta \sqrt{1-e^2}}{\sqrt{1-e^2 \cos^2 \eta}} \sqrt{a^2 \sin^2 \eta + b^2 \cos^2 \eta} b \sin \eta d\eta \\ &= \pi n_{P,\text{exterior}} \tau_P (\beta - 1) a \frac{U_\infty^2}{\text{Fr}^2} f_g(e), \end{aligned} \quad (2.76)$$

with

$$f_g(e) = (1-e^2) (\cos^2 \eta_0 - 1) \quad (2.77)$$

and the Froude number $\text{Fr} = U_\infty / \sqrt{g_z a}$. From the flux balance $0 = \Phi_{\text{inertia}} + \Phi_d + \Phi_g$, the elliptical wake model follows as

$$\frac{n_{P,\text{wake}}}{n_{P,\text{ext}}} - 1 = \frac{U_\infty}{u_{\text{rms}}} \frac{\tau_P (\beta - 1)}{a/U_\infty} \frac{f(e, \eta_0, \text{Fr}^2)}{C}, \quad (2.78)$$

only using a more complex shape factor

$$\begin{aligned} f(e, \eta_0, \text{Fr}^2) &= e^3 \frac{(e^2 + 1) \text{artanh} \left(e \frac{1 + \cos \eta_0}{1 + e^2 \cos \eta_0} \right) - e - \frac{e(e^2 - 1) \cos \eta_0}{(e^2 \cos^2 \eta_0 - 1)}}{(\cos^2 \eta_0 - 1) (e - (1 - e^2) \text{artanh}(e))^2} \\ &+ \frac{1}{\text{Fr}^2} \frac{\sqrt{1-e^2} + \frac{\arcsin(e)}{e} + \cos \eta_0 \sqrt{1-e^2 \cos^2 \eta_0} + \frac{\arcsin(e \cos \eta_0)}{e}}{\sqrt{1-e^2} (\cos^2 \eta_0 - 1)}. \end{aligned} \quad (2.79)$$

The parameter a is the major half axis and e the eccentricity of the ellipse, and the rim of the spherical cap bubble is located at the polar angle $\eta_0 = \arcsin \left(\frac{\xi}{2a\sqrt{1-e^2}} \right)$ with the chord length ξ of the spherical cap.

2.3.4 Convergence to the Stationary State

The treatment of the instationary case is similar to the derivation of the model of Dayan & Zalmanovich (1982). The change in concentration $dn_{P,\text{wake}}/dt$ is identical to the sum of the inertial flux

$$\Phi_{\text{inertia}} = F_I n_{P,\text{ext}} , \quad (2.80)$$

the gravitational flux

$$\Phi_g = F_G n_{P,\text{ext}} , \quad (2.81)$$

and the diffusive flux

$$\Phi_d = -F_D (n_{P,\text{wake}} - n_{p,\text{ext}}) , \quad (2.82)$$

giving the following differential equation:

$$\frac{dN_{P,\text{wake}}(t)}{dt} = V_{\text{wake}} \frac{dn_{P,\text{wake}}}{dt} = (F_I + F_G + F_D) n_{P,\text{ext}} - F_D n_{P,\text{wake}}(t) \quad (2.83)$$

with $n_{P,\text{ext}} = \text{const.}$ Under this condition and with $n_{P,\text{wake}}(t = 0) = n_{P,\text{ext}}$, the solution is given by

$$\frac{n_{P,\text{wake}}(t)}{n_{P,\text{ext}}} - 1 = \frac{F_I + F_G}{F_D} \left(1 - \exp\left(-\frac{F_D}{V_{\text{wake}}} t\right) \right) . \quad (2.84)$$

The stationary state models derived in Sections 2.3.1 to 2.3.3 are therefore the solutions for $t/T \rightarrow \infty$, with the time scale $T = V_{\text{wake}}/F_D$. For small $t \ll T$, the solution increases/decreases linearly with the slope $(F_I + F_G)/V_{\text{wake}}$.

The factor F_D for the spherical model is given as

$$F_D = 2\pi C u_{\text{rms}} R_{\text{wake}}^2 (\cos \theta_0 + 1) , \quad (2.85)$$

therefore

$$T = \frac{V_{\text{wake}}}{F_D} \propto \frac{R_{\text{wake}}}{u_{\text{rms}}} . \quad (2.86)$$

With a typical rise velocity for a 50° spherical-cap bubble in water of 0.25 m/s, a turbulence level of 0.2 and a wake radius of 10⁻² m, the time scale T is approximately 0.2 seconds. In other words, the time needed to reach the stationary state is small compared to the overall bubble rising times in facilities with sizes in the order of one meter and more. Furthermore, disturbances are damped out quickly if the flow in the wake is stable.

2.3.5 The Contribution of Turbophoresis

In the derivation of the inertial particle flux in Sec. 2.3.1, the fluctuation term $\tau_P(\beta - 1) \langle (\mathbf{u}'_F \cdot \nabla) \mathbf{u}'_F \rangle$ was omitted. It represents another contribution to the particle slip velocity relative to the fluid, and therefore induces a particle flux. The flux due to this term is called *turbophoresis*.

Writing the advection term in conservative form

$$\langle (\mathbf{u}'_F \cdot \nabla) \mathbf{u}'_F \rangle = \nabla \cdot \langle \mathbf{u}' \mathbf{u}'^T \rangle \quad (2.87)$$

shows that this term scales with u_{rms}^2/L (Tennekes & Lumley, 1972), with the integral length scale $L = R_{\text{wake}}$. After integration over the wake boundary, the turbophoresis term scales with $\tau_P(\beta - 1)R_{\text{wake}}u_{\text{rms}}^2$, yielding a scaling relative to the diffusive flux of

$$\frac{\Phi_t}{\Phi_d} \propto \frac{\tau_P(\beta - 1)R_{\text{wake}}u_{\text{rms}}^2}{u_{\text{rms}}R_{\text{wake}}^2} = \frac{\tau_P(\beta - 1)}{R_{\text{wake}}/U_\infty} \frac{u_{\text{rms}}}{U_\infty}. \quad (2.88)$$

The contribution of turbophoresis relative to the transport induced by the time-averaged flow is thus smaller by a factor TL^2 that is of order $\mathcal{O}(10^{-2})$, and can therefore be neglected.

However, looking at *local* contributions to the turbophoresis reveals a different scaling. Converting the surface integral over the wake boundary into a volume integral and separating terms using vector identities gives

$$\begin{aligned} \Phi_t &= \tau_P(\beta - 1) \int n_P(\mathbf{x}) \nabla \cdot \langle (\mathbf{u}'_F \cdot \nabla) \mathbf{u}'_F \rangle dV \\ &\quad + \tau_P(\beta - 1) \int \nabla n_P(\mathbf{x}) \cdot \langle (\mathbf{u}'_F \cdot \nabla) \mathbf{u}'_F \rangle dV \\ &= \tau_P(\beta - 1) \int n_P(\mathbf{x}) \left[\frac{1}{2} \Delta \langle u_F'^2 \rangle - \langle \omega_F'^2 \rangle - \langle u_F' \Delta u_F' \rangle \right] dV \\ &\quad + \tau_P(\beta - 1) \int D_{\text{turboph}} \nabla n_P(\mathbf{x}) dV \end{aligned} \quad (2.89)$$

for the flux induced by turbophoresis. The enstrophy term $\langle \omega_F'^2 \rangle$ scales with $u_{\text{rms}}^2/\lambda^2$ with the Taylor microscale λ (see Tennekes & Lumley, 1972, p. 89), such that

$$\frac{\Phi_t}{\Phi_d} \propto \frac{\tau_P(\beta - 1)R_{\text{wake}}^3 u_{\text{rms}}^2/\lambda^2}{u_{\text{rms}}R_{\text{wake}}^2} = \frac{\tau_P(\beta - 1)}{R_{\text{wake}}/U_\infty} \frac{u_{\text{rms}}}{U_\infty} \frac{R_{\text{wake}}^2}{\lambda^2}. \quad (2.90)$$

2 Theory and Entrainment Model

For homogeneous isotropic turbulence, the ratio of the integral length scale and the Taylor microscale can be expressed as

$$\frac{L^2}{\lambda^2} = \frac{A}{15} \text{Re}_L = \frac{A}{15} \text{TL Re} , \quad (2.91)$$

with $\text{Re}_L = u_{\text{rms}}L/\nu$, $L \approx R_{\text{wake}}$ and the constant A of order one (see Tennekes & Lumley, 1972, p. 67). The contribution of the enstrophy term of the turbophoresis to the mean particle transport therefore scales with a factor TL^3Re relative to the mean flow contribution. For $\text{TL} \approx \mathcal{O}(10^{-1})$ and $\text{Re} \approx \mathcal{O}(10^3)$, it is of order one and therefore comparable to the contribution of the mean flow. It should be noted though that the high-enstrophy regions are situated in the free shear layers only, which is considerably smaller than the near wake itself.

3 Experiments on Particle Entrainment

Table 3.1: Legend to Fig. 3.1

1	main pump	10	test section	19	filter valve
2	flow straightener	11	spherical lens	20	filter
3	pressure tap	12	cylindrical lens	21	filter valve
4	diffusor	13	end mirror	22	bypass valve
5	grid	14	field-of view	23	bypass/2nd pump
6	pressure tap	15	pressure tap	24	mirror
7	contraction	16	free surface	25	Nd:YAG laser
8	pressure tap	17	flow meter	26	spherical cap
9	porous rings	18	platform	27	opt. coarse grid

3.1 Experimental Setup

3.1.1 Vermeer-Setup

All two phase measurements were done in a vertical water tunnel, the VerMeer (Verticale Meerfase) facility built by (Poelma, 2004), see Fig. 3.1. The facility was used without major changes. The system for the boundary layer suction was not used during this work, instead a second pump was installed in the bypass to allow measurements with reversed flow direction, although at a reduced flow rate. This was done to allow calibration measurements of the intensity distribution in the absence of a wake, these calibrations however turned out to be of in general insufficient quality due to quickly settling particles. One porous ring was replaced to mount the spherical-cap bubble model made of brass. Another porous ring and two glass cylinders were replaced by a single, longer glass cylinder to allow for unobstructed measurements downstream of the wake.

The main centrifugal pump is powered by an ABB general purpose AC controller; the second, smaller centrifugal pump in the added bypass is throttled by an inline ball valve. Leaving the pump, the flow passes a flow straightener made of drinking straws (\varnothing 3mm) to reduce swirling motion and enters a diffusor with the rectangular grid. The sudden contraction with an area ratio 10:9 corrects for the anisotropy in the velocity fluctuations at the inlet of the test section. There, the weakly turbulent flow has a fairly flat mean velocity profile in the centre of the

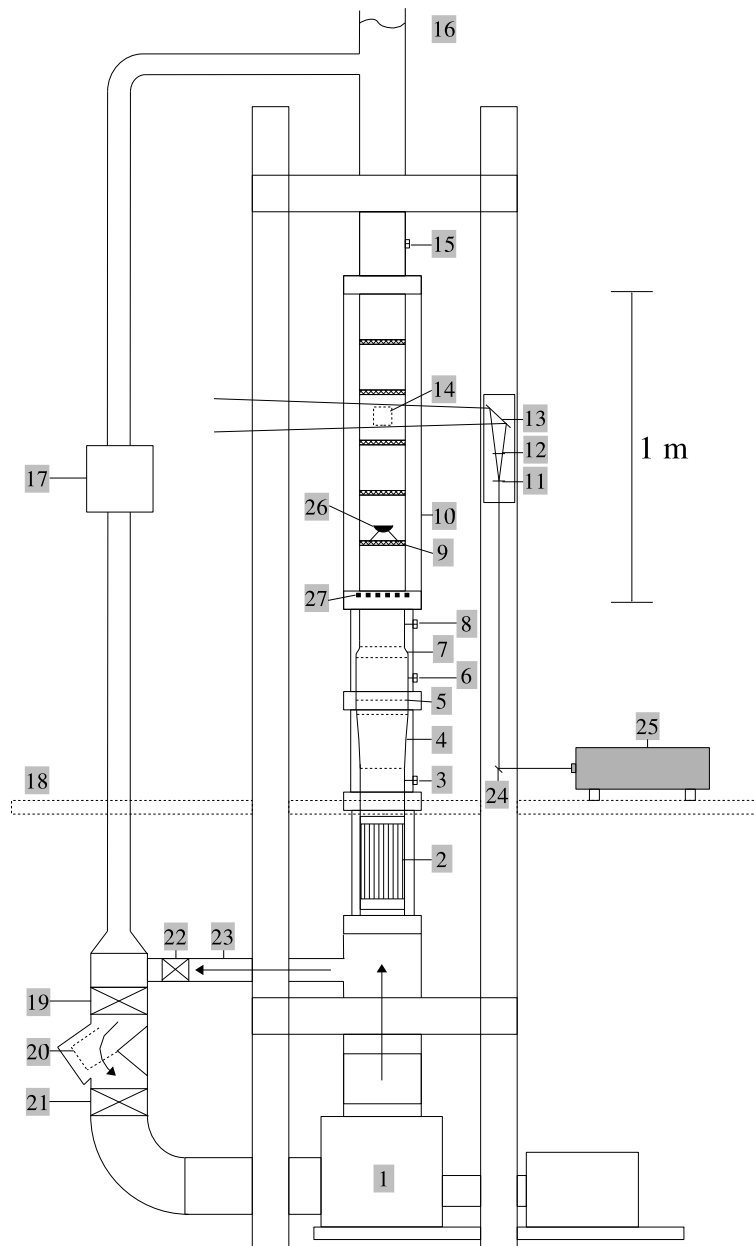


Figure 3.1: Schematic drawing of the VerMeer facility: A vertical water tunnel used for the wake measurements (by courtesy of Ch. Poelma)

3 Experiments on Particle Entrainment

pipe, and it is weakly accelerating in the centre due to the boundary layer growth at the pipe walls. After leaving the test section, the flow passes the top of the facility (the only free surface is located there at the overflow pipe), and flows back to the pump via a flow meter and a filter. The bypass and the pump mounted there were used to lower flow speeds at the minimal pump speed, for “flushing” the facility and re-entrain settled particles into the flow, and for the reversal of the flow direction in the test section.

The test section is a cuboid with square footprint made of four glass plates. It is filled with water together with the rest of the piping. The flow inside the stacked glass cylinders is thereby optically accessible without the strong distortions induced by curved interfaces. The index-matching is not perfect, though, but own calibrations have shown that the difference in horizontal and vertical magnification is less than 0.1%, see Sec. 3.2.1.

Inside the test section, glass cylinders of different lengths were used to place the spherical cap model at different distances to the inlet. An additional (hexagonal) grid was mounted at the inlet of the test section for the measurements with a high turbulence level in the flow approaching the spherical cap.

The cameras were mounted on a traverse allowing for the observation at all positions of the test section. Initially, both cameras were mounted in parallel, with the field of view of the second camera aligned to that of camera one (direct view) by an additional mirror and a beam splitter. As the image can be flipped horizontally in software, a T-shaped camera mount with only the beam splitter cube was used, gaining space in the optical path that was previously occupied by the mirror. The latter is also easier to align, as the degrees of freedom in the alignment of the mirror are no longer available and also not needed.

In general, all experiments with a new particle type were started with fresh water that was provided via an ion exchanger to avoid the formation of lime deposits in the facility. The test section, the flow straightener and the section with the grid were dismantled and cleaned to remove residues of formerly used test particles. The whole facility was flushed several times at maximum pump speed and re-filled with fresh water. The particle concentration was optimised for approximately $2 \cdot 10^4$ visible particles in each frame, therefore it was confirmed by measurements without added particles that the concentration of un-

wanted particles is less than about 200 (1% of the total concentration). The different particles used were dispersed in de-ionised water and, using a syringe, injected via a pressure tap upstream of the first grid.

3.2 Data Correction and Analysis

3.2.1 Image Alignment for 2-phase PIV

When comparing the flux of a dispersed phase over a boundary with the flux of a continuous phase, see Sec. 3.2.3, it is necessary that both flow field measurements are well-aligned. In the case of a small misalignment, the detected wake boundary (see Sec. 3.2.2) would be at different positions in the field-of-view, and the subsequent integration of the velocities would effectively be done over different boundaries with a small displacement, leading to systematic errors. A test with recorded velocity fields revealed that small displacements in the position of the wake boundary can cause significantly different results for the total flux, see Fig. 3.3. As shown in the following, these small displacement errors can already be introduced by adding or removing a filter to the optical path.

The alignment of the two cameras is done by careful adjustments of the beam splitter and/or additional mirrors, but practically an alignment with sub-pixel accuracy is difficult to achieve. Therefore, an image alignment step is done during the preprocessing step, before the PIV analysis. It is necessary to determine the mapping function that transforms the coordinates of the reference frame of camera 1 to that of camera 2 at the time of the measurement (directly before and after, to avoid accidental misalignments). This can be done in two ways: Either with an external calibration target installed in the second light path of the beam splitter, or — the so-called autoalignment — by taking the same image with both cameras (colour filters for two-phase PIV have to be removed in this case). In both cases the local displacement field can be determined by cross-correlating sections of both images (practically done by a PIV correlation analysis with a sufficient large interrogation window size). The use of the external target requires that the image is flipped horizontally to account for the beamsplitter now acting as a mirror for camera 1 and as a transparent object for camera 2. More importantly, due to the position of the beam splitter and possibly an

3 Experiments on Particle Entrainment

Table 3.2: Selected parameters of the VerMeer facility

Test section	Diameter	0.1 m
	Length	0.66 m
Spherical cap	field of view	$46 \times 46/67 \times 67$ mm
	Material	brass
	Mount	3 wires (stainless steel), 0.4 mm
	Radius R_{sphere}	=12.5 mm
	Angle θ_0	50°
	Volume-eq. diameter	11 mm
	Chord length ξ	19 mm
Medium	Type	Tap water, filtered and softened via an ion-exchanger
	Temperature	$20 - 40^\circ\text{C}$
	Viscosity ν	$(1.0 \dots 0.66) \times 10^{-6} \text{ m}^2/\text{s}$
	Flow rate	$\leq 4.81/\text{s}$
	Flow velocity U_∞	$\leq 0.63 \text{ m/s}$
Tracer	Name	EBM Fluostar, Carboxy-modified acrylate resin
	Dye	Rhodamine B
	Density	1.1 g/cm^3
	Diameter	$13.5 \mu\text{m}$
Grid 1 (fixed)	Type	squared, PVC, mounted in a diffuser/contraction of 10%
	Solidity σ_1	0.44
	Mesh spacing M_1	7.5 mm
Grid 2 (remov.)	Type	hexagonal, PVC, mounted directly in the pipe
	Solidity σ_2	0.51
	Mesh spacing M_2	15 mm
PIV settings	Interrogation window	32×32 pixel
	Overlap	50%
	Laser	200 mJ Nd:YAG, 532 nm
	Filter	OG570 570 nm low pass (tracer) 570 nm high pass (disp. phase)
	Cameras	Megaplug ES 4.0, 4MP CCD
	Lenses	Micro-Nikkor 105mm 2.8D, used at $N_A = 5.6 \dots 16$

additional mirror, the path lengths from each camera to the external target differ somewhat from that to the position of the light sheet in the test section, causing a small difference in magnification and a blurred (out of focus) external target for one camera. On the contrary, the internal calibration (autoalignment) is only affected by the removal of the filter from the optical path, whose influence on magnification and defocus is very small, see Fig. 3.2 (f). It must be ensured though that the filters are not mounted to the objective lenses itself; the misalignment introduced by the installation and removal of the filters was significantly larger than the desired (sub-pixel) accuracy allowed. Using separate filter mounts, the only systematic error in the alignment remaining is in the small displacements induced by filters which were not mounted perfectly orthogonal to the optical axis. Any rotation and magnification errors could be eliminated, see Tab. 3.3.

After the coarse mechanical alignment, the fine alignment was done by means of image processing before the PIV analysis. From the average displacement vector field of several auto-alignment measurements, an affine mapping function can be calculated from the system of equations

$$\mathbf{r}_{II} = \mathbf{r}_I + \Delta\mathbf{r} = (\mathbb{1} + A)\mathbf{r}_I. \quad (3.1)$$

In homogeneous 2D coordinates $\mathbf{r} = (x, y, 1)^T$, this system has only six free parameters. The entries of the affine map are

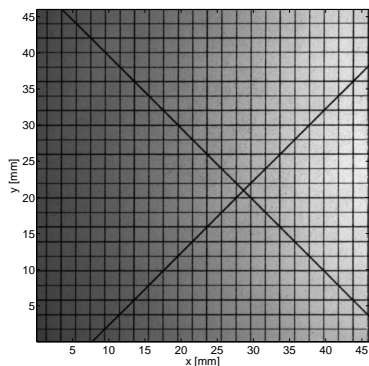
$$A = \begin{pmatrix} a & b & c \\ d & e & f \\ 0 & 0 & 1 \end{pmatrix}; \quad (3.2)$$

they can be obtained from the normal equation

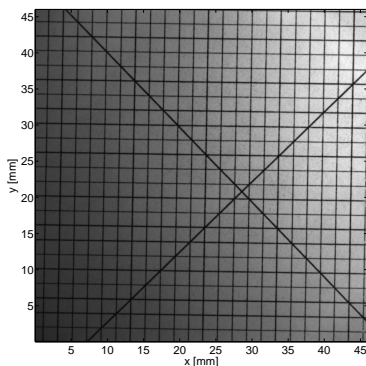
$$\{\Delta r_{ij}\}\{r_{jk}\} = \begin{pmatrix} a & b & c \\ d & e & f \end{pmatrix} \{r_{ij}\}\{r_{jk}\}. \quad (3.3)$$

The matrix $\{r_{ij}\}\{r_{jk}\}$ contains the components (row index) of all reference points (column index), multiplied by its transpose. Therefore, the solution is given by calculating the inverse of this 3×3 matrix, multiplied to the left side of Eq. (3.3). A robust fit approach that iteratively reweights the contribution of each displacement vector was found to be less sensitive to outliers than the standard least squares method; see Fig. 3.2 (c) for an example.

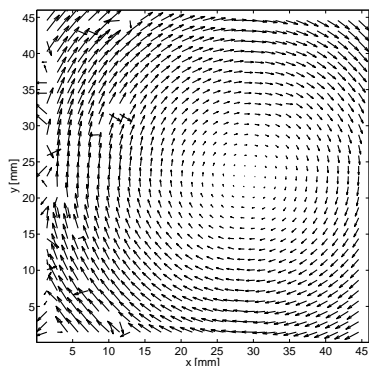
3 Experiments on Particle Entrainment



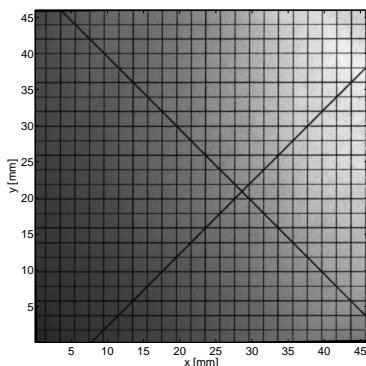
(a) original image, camera 1



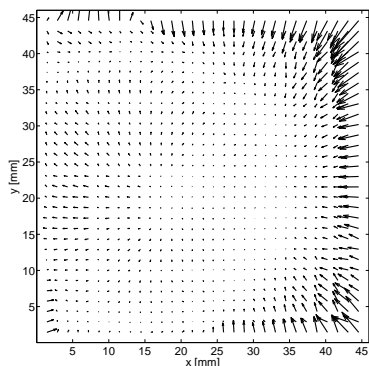
(b) original image, camera 2



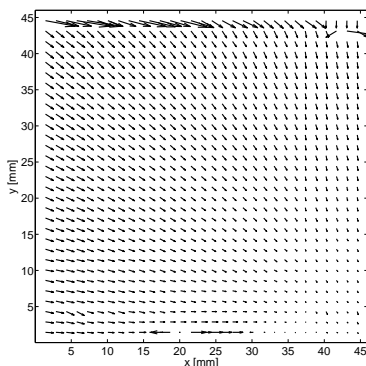
(c) local displacement of camera 2 relative to camera 1; scaling factor 5



(d) realigned image, camera 2; regions previously outside are zero-padded



(e) remaining local alignment error; the arrows were scaled with factor 100



(f) alignment error induced by a mounted filter, scaling factor 10

Figure 3.2: Correction of camera misalignments for an external target

Table 3.3: Alignment matrix coefficients and coefficient errors (mean μ and standard deviation σ for two data sets, recorded with filters removed (autocalibration))

	a	b	c	d	e	f
μ	-6.63E-4	1.59E-2	-1.54E+1	-1.62E-2	-6.77E-4	2.17E+1
σ	3.50E-5	5.41E-5	1.29E-1	2.43E-5	2.82E-5	3.54E-1
μ	-1.93E-3	1.59E-2	-1.10E+1	-1.61E-2	-2.06E-3	2.46E+1
σ	3.06E-5	3.38E-5	1.74E-1	2.00E-5	2.12E-5	3.68E-1

The effect of the fine alignment using this method is shown in Fig. 3.2. The parameters for two alignment data sets with 32 recording pairs each are shown in Tab. 3.3, whose data was obtained by calculating the mapping function for each image pair. The parameter errors result in an overall statistical alignment error over the whole image frame of $\sigma_x = 0.18 \dots 0.36$ and $\sigma_y = 0.13 \dots 0.35$ pixel for the first data set, and $\sigma_x = 0.2 \dots 0.37$ and $\sigma_y = 0.17 \dots 0.37$ pixel for the second. These statistical errors are mainly caused by vibrations of the setup, and to a some degree also by the image correlation, which has a finite error of approximately 0.1 to 0.2 pixel (Adrian & Westerweel, 2010).

An indication about the magnitude of the flux uncertainties induced by misalignment can be obtained from Fig. 3.3, where the resulting integrated flux is plotted over the magnitude of an artificial misalignment of the wakeboundary for a single phase time-averaged flow field. Despite some visible noise that is smaller than the statistical measurement uncertainty (shaded area), there is a distinct trend visible. The resulting flux changes by approximately $-0.2\text{cm}^3/\text{s}$ per pixel displacement. A displacement of a few pixel can therefore alter the result of the integration by a value that is comparable to the magnitude of the observed flux difference in Fig. 4.6 for particles with a small response time. The alignment error should therefore be smaller than one pixel.

The estimate for the systematic error induced by the mounting of the filters, a series of images was taken from an internal and an external target with alternately mounted and unmounted filters. One local displacement vector field is shown in Fig. 3.2 (f), the statistics of the

3 Experiments on Particle Entrainment

Table 3.4: Systematic alignment errors (mean μ and standard deviation σ) due to installed filters: This error is a result of installing filters that changes the length of the optical path (magnification error, $\det(T) = 1$ if there is no error of this type); filters that are not aligned normal to the optical axis cause a small displacement (Δx and Δy) of the image; image rotation (Ω_z), relative axis scaling (S_{xx}/S_{yy}) and shear (S_{xy}) are not affected by the installation of filters (coefficients comparable to self-alignment)

internal calibration target, green filter (high-pass)						
	a	b	c	d	e	f
μ	-2.31e-3	-1.87e-5	2.35e-3	-2.06e-5	-2.04e-3	-2.37e-3
σ	5.30e-5	2.50e-5	2.24e-4	1.32e-5	3.69e-5	1.98e-4
	$\det(T) - 1$	Ω_z	S_{xy}	$S_{xx}/S_{yy} - 1$	Δx [px]	Δy [px]
μ	-4.34e-3	-9.24e-7	-1.96e-5	-2.75e-4	2.41	-2.42
σ	3.86e-5	1.31e-5	1.51e-5	8.29e-5	0.23	0.20

internal calibration target, orange filter (low-pass)						
	a	b	c	d	e	f
μ	-1.16e-3	6.59e-5	1.18e-3	1.90e-6	-1.24e-3	-5.55e-4
σ	3.32e-4	7.86e-5	2.75e-4	1.49e-5	2.20e-4	8.24e-4
	$\det(T) - 1$	Ω_z	S_{xy}	$S_{xx}/S_{yy} - 1$	Δx [px]	Δy [px]
μ	-2.41e-3	-3.20e-5	3.39e-5	8.16e-5	1.21	-0.568
σ	4.87e-4	4.20e-5	3.80e-5	2.85e-4	0.282	0.844

for reference: internal calibration target, no filter (self-alignment)						
	a	b	c	d	e	f
μ	1.08e-5	3.12e-5	-1.24e-5	1.62e-5	7.06e-5	2.25e-5
σ	8.11e-5	7.90e-5	1.78e-4	6.03e-5	9.28e-5	1.28e-4

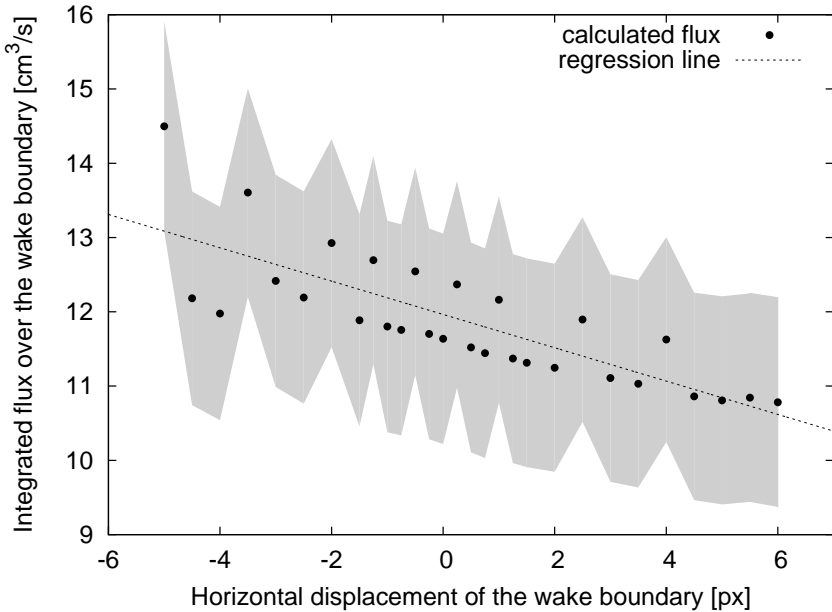


Figure 3.3: Effect of artificial displacements of the wake boundary: small horizontal displacements are sufficient to alter the outcome of the integration; the trend indicates an error of approximately $-0.2\text{cm}^3/\text{s}$ per pixel displacement

systematic alignment errors are given in Tab. 3.4. Adding a filter to the optical path does not induce any noticeable rotation or shear in the image, nor an anisotropy in the scaling of the axes. The magnitude of these misalignments are of order $\mathcal{O}(10^{-4})$ and smaller, which causes sub-pixel displacements for an image with $\mathcal{O}(10^{-3})$ pixels in one dimension, and the standard deviation is typically of the same order. However, it also induces a noticeable change in magnification (the determinant of the transformation matrix is not unity), and it typically induces a small displacement due to tilted filters. The two latter contributions cause local displacements in the order of a few pixels, but stay well below the size of a PIV interrogation window (32 pixel).¹

¹This uncertainty can nevertheless have an influence on the flux measurements, as a 2 pixel displacement of the wake boundary in the reference image might change the measured flux; see also Sec. 4.2.2.

3 Experiments on Particle Entrainment

The particle response time is fairly low for all particles used for the dispersed phase, and thereby its velocity vector fields are strongly correlated to those of the continuous phase. Therefore, it is possible to test the alignment by maximising the correlation for small displacements. It is thereby also possible to correct for the remaining displacement due to the alignment with removed filters. It is nevertheless a method with larger statistic uncertainties than the alignment described above.

Summarising, the alignment of two-phase PIV images by means of an affine mapping completely eliminates any shear and rotation in the images, and reduces the local deviations to fractions of pixels. In principle, non-linear effects like lens distortions can be corrected in a similar way; however, the remaining systematic errors found were sufficiently small. Using an external calibration target in the second light path of the beam splitter has the advantage that no changes to the optical system are needed (no filters need to be removed), though care must be taken that the optical distance is identical for both light paths of both cameras to avoid changes in magnification. The autocalibration method avoids this problem, the removal of the filters for the calibration however induces a small but well-defined change in magnification and a small displacement of the image. Even these small misalignments were sufficient to make a comparison of calculated fluxes over a boundary impossible. By maximising the correlation of the two measured velocity fields, the displacement can be corrected after the PIV analysis.

3.2.2 Detection of Wake Boundaries

The boundary of the near-wake is defined by the separating streamline in the time-averaged flow field from the rim of the spherical cap to the rear stagnation point. However, this definition is practically useless, even for hypothetical data free of all measurement uncertainties. The ubiquitous fluctuations in a turbulent flow make it in general impossible to track the separating stream line e.g. with the Runge-Kutta method in the time-averaged flow field from the rim of the spherical cap to the rear stagnation point. Therefore, an approximation to the wake boundary is needed. As the stream line plot in Fig. 3.4 suggests, the wake boundary is approximately described by an ellipsoid of rotation, with a deformation towards an egg-like shape for Reynolds numbers at the lower end of the measurement range ($Re < 10^3$).

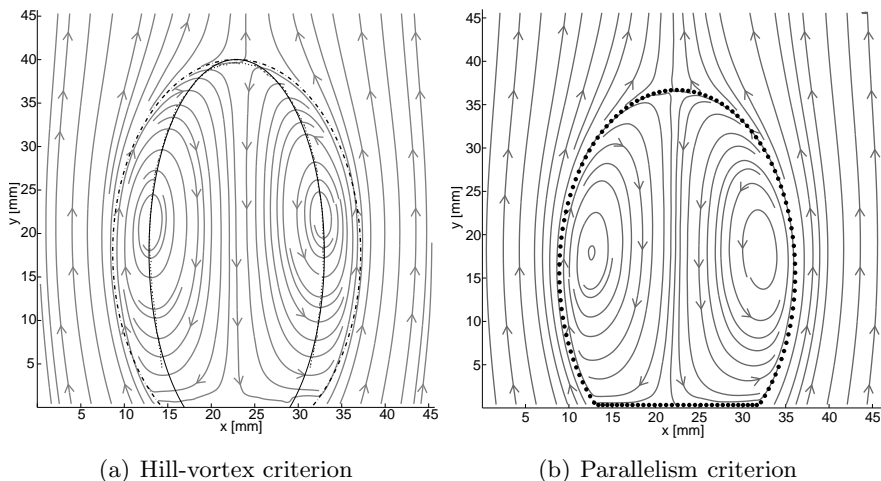


Figure 3.4: Methods for determining the wake boundary

The choice of an ellipsoid of rotation can be motivated analytically as well. The wake behind spherical caps has been found to be similar to a Hill vortex (Wegener & Parlange, 1973; Brücker, 1996). From the Stokes stream function of a Hill vortex with radius R , the velocity can be derived as

$$\mathbf{v}(\mathbf{x}) = 1.5 \left((2x^2 \mathbf{u}_\infty - (\mathbf{u}_\infty \cdot \mathbf{x}) \mathbf{x}) / R^2 - \mathbf{u}_\infty \right). \quad (3.4)$$

Requiring that the velocity component parallel to \mathbf{u}_∞ is zero gives $0 = \mathbf{u}_\infty \cdot \mathbf{v}$, and using the simplification $\mathbf{u}_\infty = (0, 0, u_z^\infty)$ in cylindrical coordinates gives

$$1 = \frac{r^2}{R^2/2} + \frac{z^2}{R^2}, \quad (3.5)$$

an equation for an ellipse with the half axes $a = R/\sqrt{2}$ perpendicular and $b = R$ parallel to \mathbf{u}_∞ . Therefore, the wake boundary can be found by fitting an ellipse to the zero-crossings of the axial component of the mean flow velocity and subsequent rescaling of the smaller half axis by the factor $\sqrt{2}$.

Alternatively to the similarity with a Hill vortex, the wake boundary can be determined by finding the ellipse that minimises the angle between the tangent to the boundary and the flow. There is no obvious

3 Experiments on Particle Entrainment

advantage of one fitting method over the other. However, it turned out that it was easier to implement the additional constraints (enforcing the ellipse to pass through the points at the rim of the spherical cap) for the *parallelism criterion*.

The sought-for ellipse is a general conic

$$F(x, y) = ax^2 + bxy + cy^2 + dx + ey + f = 0 \quad (3.6)$$

with the ellipse-specific constraint $b^2 - 4ac < 0$ (see Halir & Flusser, 1998, for details about the fitting method) and two additional constraints from the requirement that the edges of the spherical cap lie on the ellipse. The remaining free parameters were found iteratively by minimising the cost function

$$\sum_i \left| \operatorname{atan} \left(\frac{v_i^\perp}{v_i^\parallel} \right) \right| A_i . \quad (3.7)$$

Equation (3.7) minimises the sum of area-weighted absolute angles between the local tangent to the boundary and the time-averaged flow field. It is therefore equivalent to choosing the boundary *as parallel as possible* to the local mean flow velocity. This criterion was found to be more robust than the minimisation of the total absolute flux over the boundary. The latter tends to converge to solutions in close vicinity to the spherical cap, where the magnitude of the fluid velocities is almost zero.

3.2.3 Flux Measurements

Measurement Principle

Measuring the preferential concentration of particles in a wake can either be done directly via a concentration measurement, (see Sec. 3.2.4), or by analysing the particle flux into or out of a volume, see Sec. 3.2.3. The latter method is based on the same local flux balance idea that was described in Sec. 2.1.4: In the stationary state, a time-independent particle concentration in the domain requires that all contributions to the local particle flux density cancel each other. If only the mean particle transport and turbulent diffusion are considered, then the flux balance reads

$$0 = \overline{\rho_P \mathbf{v}_P} + \nu_P \nabla \overline{\rho_P} . \quad (3.8)$$

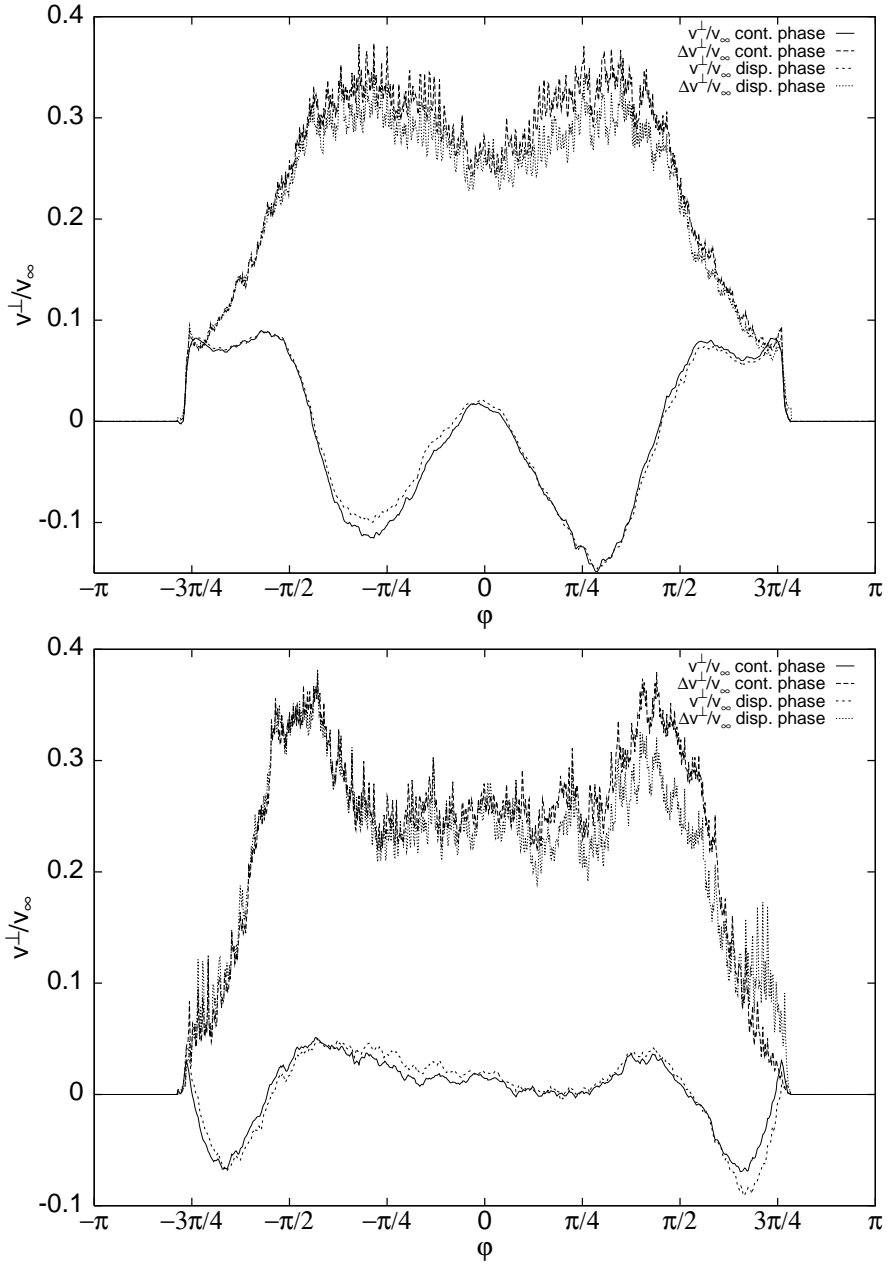


Figure 3.5: Velocities normal to the elliptic boundaries, fitted ellipse (top) and scaled ellipse (bottom), $Re = 2300$

3 Experiments on Particle Entrainment

Rearranging, taking the divergence and integrating over a control volume V then results in

$$\iint_{\partial V} \overline{\mathbf{v}_P} d\mathbf{A} = - \iint_{\partial V} \nu_P \nabla \log \overline{\rho_P} d\mathbf{A} , \quad (3.9)$$

whereby the Gauss theorem is used to transfer the volume integral into a surface integral over the boundary ∂V of the control volume. The diffusivity ν_P is a symmetric and positive definite matrix, therefore a non-vanishing left-hand side implies that there is a mean gradient in $\log \overline{\rho_P}$ over the boundary of the control volume, and therefore a preferential concentration.

Algorithm

The volume flux through the surface of the ellipsoid defined in Sec. 3.2.2 is assumed to be axis-symmetric (the wake boundary is a body of revolution) around the z -axis, and can therefore be obtained by integration of the normal velocity v^\perp over the wake boundary:

$$\overline{V} = 2\pi \int_{-\pi}^{\pi} v^\perp r(\phi) \sqrt{\left(\frac{dr}{d\phi}\right)^2 + \left(\frac{dz}{d\phi}\right)^2} d\phi \approx \sum_i v_i^\perp A_i/2 = 1/2 \mathbf{v}^\perp \cdot \mathbf{A} \quad (3.10)$$

The sum on the right is the used approximation for this integral, with $A_i/2$ being the surface area of point i of the elliptic boundary, taking into account that only half of the ellipse must be rotated to get an ellipsoid. Similarly,

$$\sigma_{\dot{V}} \approx 1/2 \sqrt{\mathbf{A}^T \text{COV}(\mathbf{v}^\perp) \mathbf{A}} \quad (3.11)$$

gives an estimate for the standard deviation of the volume flux according to the propagation of uncertainty, including turbulent fluctuations of the normal velocity as well as statistical measurement errors. The variance-covariance matrix of the normal velocities is defined as

$$\text{COV}(\mathbf{v}^\perp)_{kl} = \frac{1}{M} \sum_{j=1}^M \left(v_{k,j}^\perp - \overline{v_k^\perp} \right) \left(v_{l,j}^\perp - \overline{v_l^\perp} \right) . \quad (3.12)$$

Assuming M statistically independent velocity fields, the standard error of the ensemble-averaged volume flux \overline{V} can then be obtained from

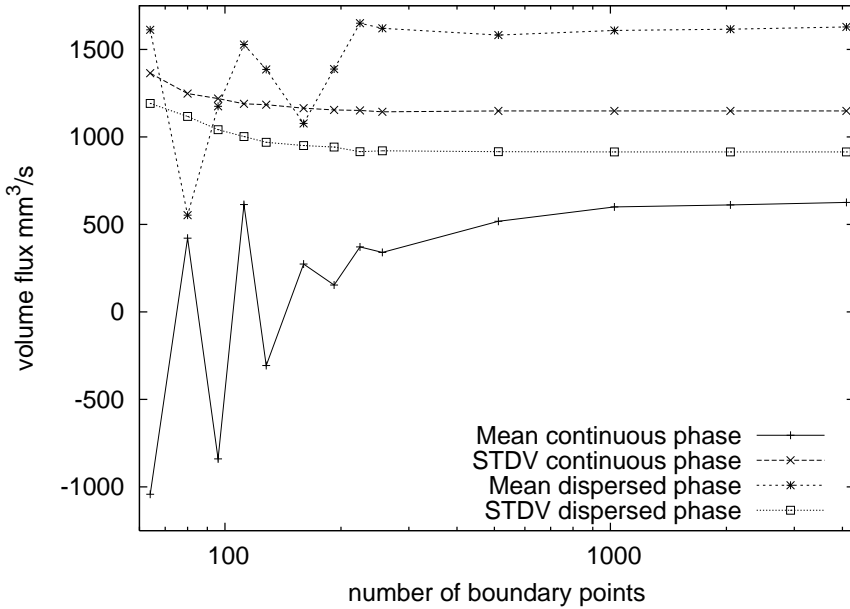


Figure 3.6: Dependence of the flux error estimate on the number of interpolation points at the wake boundary

Eq. (3.11) by

$$SE_{\bar{V}} \approx \frac{\sigma_{\dot{V}}}{\sqrt{M}}, \quad (3.13)$$

which represents the statistical uncertainty for the flux measurements. The normal component of the velocity v_i^\perp is interpolated from the instantaneous velocity fields by linear interpolation for every point of the boundary. To do this, the boundary is approximated by a number N of discrete points, for which the normal vector and the area element are calculated from the two neighbouring points. By taking into account the correlation between velocities at neighbouring boundary points, the calculated values for the mean volume flux and its fluctuations was found to be independent of the total number of points N , provided that it was sufficiently large.

Convergence of the Method

The total number of points needed to approximate the elliptical wake boundary can be determined by plotting the standard error of the mean (SEM) of the calculated flux for different point counts. Fig. 3.6 shows this plot; the mean becomes independent of the number of interpolation points for a point count of at least 512. The standard deviation (STDV) converges with about 256 points and more. A point count of 128 is approximately equivalent to a sampling of the boundary with a PIV interrogation window size between each sample, therefore 512 point are approximately equivalent to a fourfold oversampling. The graph also shows that the method for determining the error is independent of the number of interpolation points beyond a sufficient number, a result of the fact that correlations between data points are taken into account in the error propagation.

The development of the ensemble-averaged flux and its uncertainty (standard error of the mean) is shown in Fig. 3.7. A sufficiently high number of statistically independent flow fields (> 200) is needed to obtain a statistically meaningful flux at the level of the velocity fluctuations in the experiment. For most particle types, data sets with 512 and 1024 PIV images were recorded, and several sets of 256 for those particle types that lead to a fast loss of concentration of the dispersed phase. Also shown is that there is a small systematic error in the flux measurements: the flux of the continuous phase does not converge to zero, as one would expect for an incompressible fluid. This is related to the fact that the wake is not perfectly axisymmetric; the errors induced by the 2D approximation of the integral over the wake boundary are therefore large compared to the obtainable statistical uncertainties.

A last source of uncertainty stems from the alignment between the two cameras: The wake boundary is determined by an ellipse fit to the continuous phase (see Sec. 3.2.2), therefore uncertainties in the mapping function between both cameras cause an integration of the dispersed phase flux over a marginally different boundary, as it can be seen by comparing the bootstrapping results for two different datasets in Fig. 3.8.

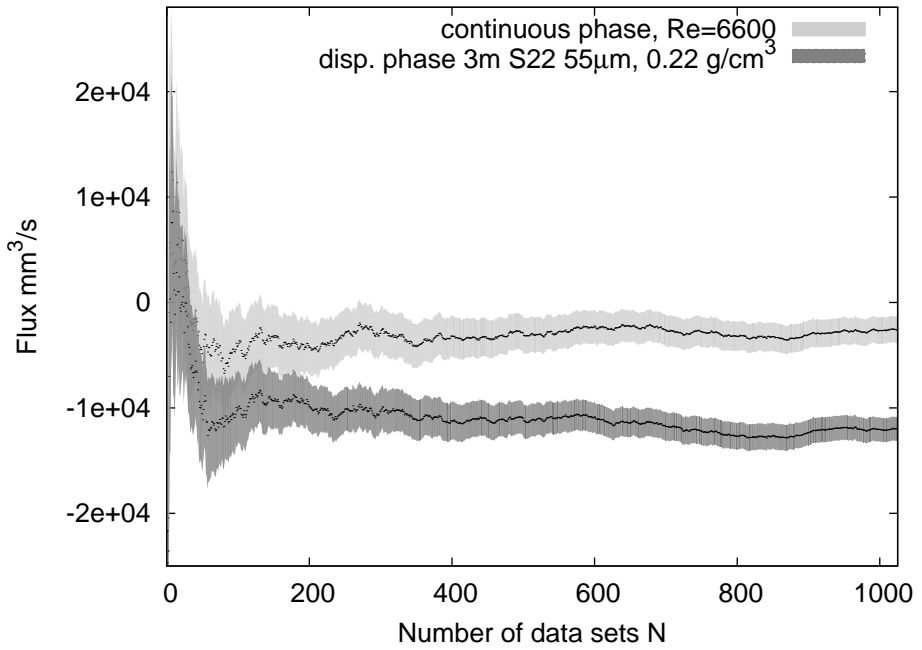
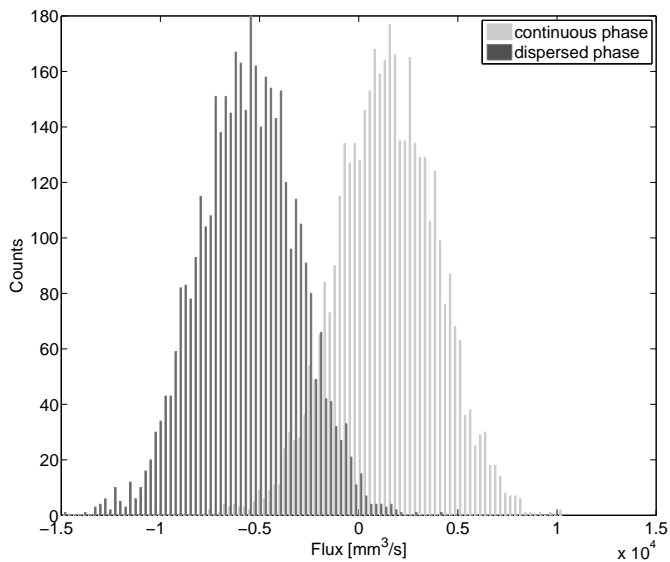
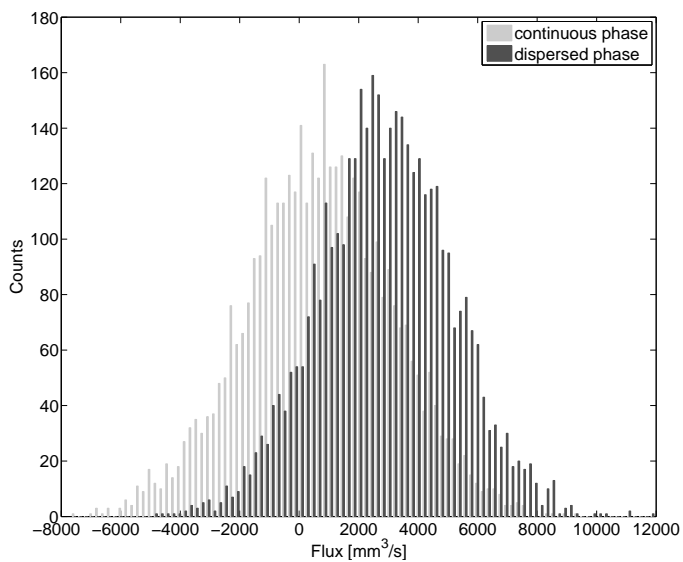


Figure 3.7: Convergence of the flux measurement: approximately 200 flow fields are necessary that the flux difference becomes statistically significant; however, a small systematic error can also be observed (flux of the continuous phase differs from zero)

3 Experiments on Particle Entrainment



(a) 3m S22 particles, $55\mu\text{m}$, 0.22 g/cm^3



(b) 3m K1 particles, $110\mu\text{m}$, 0.125 g/cm^3

Figure 3.8: Histograms of the 4096 mean fluxes calculated from 256 randomly selected velocity fields out of a dataset of 1024 fields

Uncertainty Estimation by Bootstrapping

To validate the estimated standard deviations for the flux measurements, the distribution of the calculated means for a sub-sample of the whole data set was calculated. Fig. 3.8 shows this distribution; the time-averaged fluxes were calculated over 256 velocity fields which were selected randomly from a data set of 1024 PIV records. The mean of all estimated fluxes is $1.5 \cdot 10^3 \text{mm}^3/\text{s}$ with a standard deviation of $2.5 \cdot 10^3 \text{mm}^3/\text{s}$. The average estimated standard deviation of each subset of 256 samples is $3.9 \cdot 10^4 \text{mm}^3/\text{s}$, which is almost identical to the estimated standard deviation from the error propagation of $3.8 \cdot 10^4 \text{mm}^3/\text{s}$. The standard deviation of the means is furthermore almost identical to the standard error of the mean ($3.8 \cdot 10^4 / \sqrt{256}$) $\text{mm}^3/\text{s} = 2.4 \cdot 10^3 \text{mm}^3/\text{s}$. Therefore, the distribution of the estimated average flux values is for all practical aspects well-described by a normal distribution, and the error analysis delivers results that agree well with the bootstrapping test.

The histogram in Fig. 3.8 also shows that the centre of the distribution of the calculated time-averaged fluxes deviates a bit from zero (for the continuous phase). Possible causes are misalignments in the spherical cap and the light sheet (not aligned with the axis of symmetry), and also slightly higher noise in the PIV vectors in areas with less contrast in the recorded image. In the following, the presented flux values are always taken relative to the continuous phase, which means the difference between the two phases.

3.2.4 Concentration Measurements

The concentration of particles have not been determined in separate experiments, the concentration analysis was limited to the available records taken for the PIV analysis. A PIV image is a spatial measurement proportional to the total scattered light intensity of dispersed particles, if factors like light absorption on the optical path from the particle to the sensor can be assumed to be homogeneous. The local inhomogeneities in the transmission of the imaging optics (vignetting) must be neglectable as well, an assumption that is typically fulfilled if the chosen aperture is sufficiently small (F/5.6 to F/16) and the sensor diagonal is smaller than the imaging circle of the lens (21.5 mm versus 43.3 mm). Under these circumstances, the local light intensity of the

3 Experiments on Particle Entrainment

image can be modeled as

$$I(x, y) = M(x, y)L(x, y)n_P(x, y) + N(x, y), \quad (3.14)$$

with the local effect of the anisotrope Mie scattering $M(x, y)$, the local luminosity $L(x, y)$, the particle number density $n_P(x, y)$ and a noise term $N(x, y)$. The noise term can be eliminated by averaging sufficiently many images. The following subsections discuss all contributions and methods that have been used to deal with the Mie scattering and local inhomogeneities in the luminosity, with the aim to determine the local particle number density as a function of the local light intensity.

Mie scattering

The anisotropy of Mie-scattering is shown in Fig. 3.9 for a $55\mu\text{m}$ gas bubble and green light with $\lambda = 532\text{nm}$. For particles with a certain size dispersion and at sufficiently large apertures of the objective lens used, the graphs show a smooth curve with a decrease of the scattered light intensity towards larger scattering angles, something that is not necessarily the case for other particles. It was found that the intensity drop over the imaging frame (factor 2.6) can be considerably larger than the light falloff due to both light absorption and the divergence of the light sheet. Mie scattering is therefore the dominant contribution to the inhomogeneity of the recorded light intensity over the frame. Furthermore, it is also the most difficult one to correct; there is no simple functional relation, such that it must be estimated using a software package (MiePlot) with known particle size distribution. An advantage is that Mie scattering — if the absolute concentration is sufficiently low that multiple scattering is negligible — is independent of particle concentration, its correction can therefore be applied before the correction of other inhomogeneities.

Correction for Mie Scattering

The influence of the Mie scattering can be corrected, if the angular scattering intensity distribution is known for the particles, and the angles of observation from the setup of the imaging system. A particle whose image is recorded on the sensor of the camera is observed under an angle defined by the light ray from the particle towards the object-side

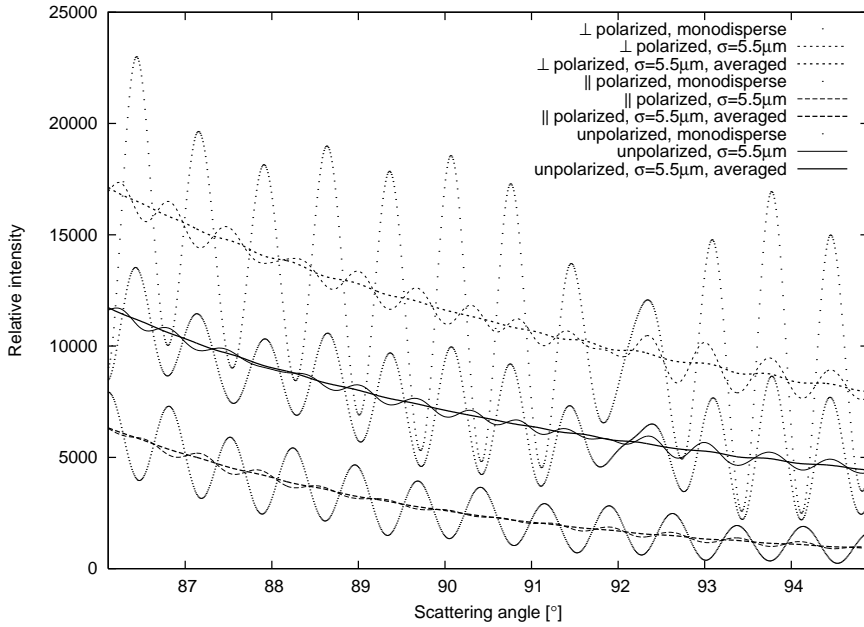


Figure 3.9: Mie-scattering for a $55\mu\text{m}$ gas bubble (monodisperse, with normal distributed diameter ($\sigma = 5.5\mu\text{m}$) and averaged over the entering pupil at F8), field-of-view of a Micro-Nikkor 105mm 2.8D, $15.4 \times 15.4\text{mm}$ sensor, $M = 1 : 3$

3 Experiments on Particle Entrainment

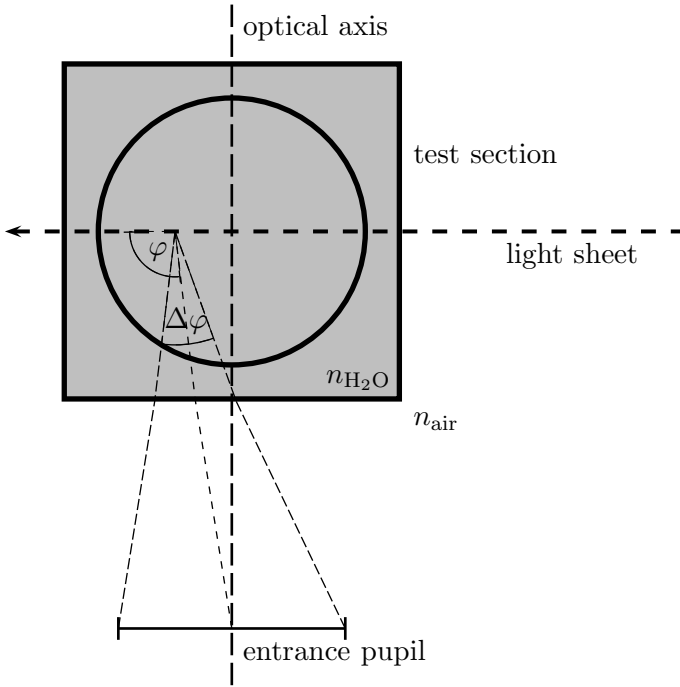


Figure 3.10: Schematic drawing of the imaging of the particles; the light recorded from a particle by the camera was scattered under the angle φ and the scattered light intensity is averaged over the angle $\Delta\varphi$ (not to scale)

principal point (the intersection of the entrance pupil with the optical axis). The rays used for creating the particle image on the sensor are those within the cone with opening angle $\Delta\varphi$.

With known particle size distribution and refractive index, the angular scattering intensity distribution is calculated using a software package (Mieplot) and subsequently filtered with a box filter of width $\Delta\varphi$. The angle ϕ can be determined from either the focal length of the lens or from the position of the entrance pupil.

The attempts to correct for the inhomogeneity due to the Mie scattering were only successful for certain data sets. The method depends strongly on well-determined particle properties (refractive index) and size distributions. Uncertainties in these parameters can lead to over-

and undercorrections that introduce significant systematic errors to the concentration analysis.

Absorption

According to the Lambert-Beer law for light absorption by dispersed absorbers, the loss of light intensity is exponential with the absorption coefficient

$$\alpha = \sigma_A \rho \quad (3.15)$$

with the absorption cross section σ_A of the absorber and its number per unit volume $\rho = N/V$. The term absorption is used somewhat ambiguous here, it is de facto the loss of light intensity in the light sheet plane due to scattering in all directions. Nevertheless, the light absorption model is independent of the underlying mechanism causing the loss in intensity, therefore it can be used here as a phenomenological model.

Using the particle volume load $\Phi = N \cdot V_P/V$ and assuming spherical absorbers yields

$$\alpha = \frac{\pi/4d_P^2\Phi}{\pi/6d_P^3} = \frac{3\Phi}{2d_P} \quad (3.16)$$

For the conditions used in the experiments, the light intensity loss over the frame width of $l = 46\text{mm}$

$$1 - \frac{I(l)}{I(0)} = \exp(-\alpha l) = \exp\left(-\frac{3\Phi l}{2d_P}\right) \quad (3.17)$$

is approximately 12% ($d_P = 55\mu\text{m}$, $\Phi = 10^{-4}$) to 47% ($d_P = 110\mu\text{m}$, $\Phi = 10^{-3}$) for a perfect absorber (isotropic scatterer). Including the absorption due to the tracer phase ($d_P = 13\mu\text{m}$, $\Phi = 5 \cdot 10^{-5}$) gives an intensity loss of 32% to 49%. As forward scattering is by far the dominant direction, the calculated values are overestimating the real amount of light absorption. The light absorption by the water can be neglected for this analysis, the absorption coefficient for $\lambda = 532.5\text{nm}$ light $\alpha = (0.0447 \pm 0.0011)\text{m}^{-1}$ (Pope & Fry, 1997) is too small to contribute significantly over distances of several centimetres (<1%).

Light Sheet Divergence

For a PIV measurement, a quasi-2D illuminated volume is needed with dimensions of several centimetres or even more in width and a thickness of less than 1 millimetre. However, light sheet optics with good coatings for the use with high-energy laser beams are expensive and typically limited to sizes of up to 2 inch. Therefore, often a divergent light sheet is used (only one concave cylindrical lens), as the size of the mirror or the last lens limits the maximum width of a parallel light sheet (created with a concave and a convex cylindrical lens with aligned focal points). The closer it is installed to the measurement volume, the more apparent the divergence will be in the image; the focal length of the cylindrical lens only determines the part of the beam that is used to illuminate the measurement volume.

Angular Beam Profiles

Another source of inhomogeneity is due to the non-constant intensity profile of the laser beam itself. For optimising output intensity, the resonators of the lasers are aligned such to allow for higher modes (TEM_{xy}) than only the lowest, Gaussian mode (TEM_{00}). This results in a superposition of the lower modes and in a non-Gaussian beam profile. With an adequately aligned light sheet, the relative deviation from the mean intensity could be kept below 15%, but the deviations are visible as an angular modulation of the light sheet intensity.

Finding the Focal Point of the Light Sheet

Determining the focal point (or virtual origin) of the light sheet is necessary for the correction of both the divergent light sheet and the angular beam profile. Due to the beam profile, the image dimension which is orthogonal to the incoming light (i.e. the columns for a horizontal light sheet) are correlated. By correlating two columns x_1 and x_2 with a scaling parameter a and an offset Δy

$$h(a, \Delta y) = \int_{y \in Y} I(x_1, y) I(x_2, ay + \Delta y) dy \quad (3.18)$$

and subsequently finding the maximum of $h(a, \Delta y)$, each pair of columns gives one parameter pair $(a, \Delta y)$ that maximises the correlation. By

calculating these for many columns, the focal point of the light sheet can be determined with a (robust) fitting method. For an accuracy of about 1% in the determined coordinates of the focal point, typically 4000 correlations of random column pairs had to be calculated. This method works better if a strong beam profile is visible in the light sheet intensity, and it is furthermore improved by averaging many records to obtain a smooth intensity image with less noise. Somewhat surprisingly, a low-pass filtering step for smoothing the intensity image before the correlation step did not improve the accuracy of the determined focal point coordinates.

Luminosity Models

The light absorption can be corrected together with the inhomogeneities due to the divergent light sheet and the laser beam with a model derived from the Poynting theorem

$$\nabla \cdot \mathbf{S} = -\frac{\partial U_{\text{EM}}}{\partial t} - \mathbf{j} \cdot \mathbf{E} \quad (3.19)$$

for a constant absorber density $\partial U_{\text{EM}}/\partial t = \alpha$ and in the absence of currents \mathbf{j} and electric fields \mathbf{E} . Furthermore, for a radially expanding wave, the Poynting vector \mathbf{S} has only a component in radial direction, which allows to solve for S_r in cylindrical coordinates. As the intensity of the wave is given by $|\mathbf{S}| = S_r$, this gives the formula for the distribution of the light intensity

$$L(r, \phi) = S_r(r, \phi) = C(\phi) \frac{\exp(-\alpha r)}{r}, \quad (3.20)$$

with the scaling constant C dependent on the polar angle ϕ due to the non-constant laser beam profile. This model can now be fitted to the averaged measured intensity, after applying the correction for the Mie scattering. The absorption coefficient α is global, whereas the scaling constants $C(\phi)$ must be determined separately for each angular segment of the light sheet.

Fitting the absorption model naturally implies that the average particle concentration (which are the absorbers) is homogeneous over the domain. This is of course not fulfilled if there is preferential concentration. The Poynting theorem still allows to derive a more general

3 Experiments on Particle Entrainment

model by assuming the concentration of absorbers is proportional to the concentration of particles. Then,

$$\operatorname{div} \mathbf{S} = \frac{\partial u}{\partial t} = -\gamma \rho_P = \kappa \tilde{I} = \kappa(I_{\text{ideal}} + N), \quad (3.21)$$

assuming that the recorded intensity and the ideal intensity (that is expected theoretically for a smooth particle concentration, the limit of infinitely many averaged PIV records) only differ by an additive noise term ($\tilde{I} = I_{\text{ideal}} + N$). From

$$L(r, \phi) = S_r = \frac{1}{r} \int_{r_0}^r -\kappa I_{\text{ideal}}(\tilde{r}, \phi) \tilde{r} d\tilde{r} + C(r_0(\phi), \phi) \quad (3.22)$$

follows the noise term

$$N(r, \phi) = \tilde{I}(r, \phi) - n_P(r, \phi) \left(\frac{1}{r} \int_{r_0(\phi)}^r -\alpha n_P(\tilde{r}, \phi) \tilde{r} d\tilde{r} + C(r_0(\phi), \phi) \right) \quad (3.23)$$

and thereby the particle concentration

$$n_P(r, \phi) = \frac{\tilde{I}(r, \phi) - N(r, \phi)}{\frac{1}{r} \int_{r_0}^r -\kappa(\tilde{I}(\tilde{r}, \phi) - N(\tilde{r}, \phi)) \tilde{r} d\tilde{r} + C(r_0(\phi), \phi)}. \quad (3.24)$$

This algorithm however was not implemented. Eq. (3.24) represents a system with an integral equation for each point in the image, with the absorption constants κ and α , the values of the line integrals at the border of the domain $C(r_0(\phi), \phi)$ and the concentration $n_P(r, \phi)$ as unknowns, and is therefore underdetermined. It can only be solved with additional assumptions about e.g. the local uniformity or symmetry of the particle concentration.

Normalisation with a Reference Data Set

A disadvantage is that the illumination is not homogeneous due to (i) the non-isotropic Mie scattering of the particles, (ii) the light loss due to cumulative scattering, and (iii) the divergent light sheet. All these effects can be corrected by means of a proper normalisation of the recorded images with a reference data set taken under the same conditions of illumination, imaging and particle concentrations.

It was therefore decided to normalise the measured light intensity with a reference data set which was recorded under identical conditions of illumination, typically recorded at a lower flow speed, which eliminates the need of a Mie correction. The time-averaged intensity of the first dataset $I_1(x, y)$ was — after background subtraction — divided by the time-averaged intensity of the reference dataset $I_2(x, y)$, and averaged using the geometric mean (Fleming & Wallace, 1986)

$$\frac{n_{\text{wake},1}/n_{\text{ext},1}}{n_{\text{wake},2}/n_{\text{ext},2}} = \frac{GM((I_1(x, y)/I_2(x, y))|_{(x,y)\in\text{wake}})}{GM((I_1(x, y)/I_2(x, y))|_{(x,y)\in\text{ext}})}. \quad (3.25)$$

This method works best if the absolute mean particle concentration — and therewith the light falloff due to absorption — is identical for both data sets. The latter condition is not always fulfilled, therefore the differences in absorption introduce a small systematic error. The main disadvantage is that due to the normalisation of noisy intensity values with noisy intensity values, the uncertainties in the concentration measurements increase significantly. For normal distributed time-averaged intensities, the ratio distribution is a Cauchy distribution, for which the sampling variability of the mean does not decrease with increasing sample size Rothenberg *et al.* (1964). The geometric mean is similarly affected by the long tails of the (almost) Cauchy-distributed intensity ratios. The statistical error due to the blown-up noise was found to be significantly larger than the systematic error introduced by any differences in absorption. Fig. 3.11 shows a comparison of both normalisation methods.

Compared to the method based on a luminosity model with a large systematic uncertainty and a small statistical uncertainty, this normalisation method has opposite properties, with small systematic errors but significant statistical uncertainties. Based on these properties, it was however chosen for the data analysis presented in Sec. 4.3, as statistical uncertainties are more easily dealt with by increasing the number of measurements. It is nevertheless the explanation for the large errorbars in Fig. 4.7.

Alternative Methods for Concentration Analysis

There exist many more methods for concentration measurements, both experimentally as well as more sophisticated approaches to data analy-

3 Experiments on Particle Entrainment

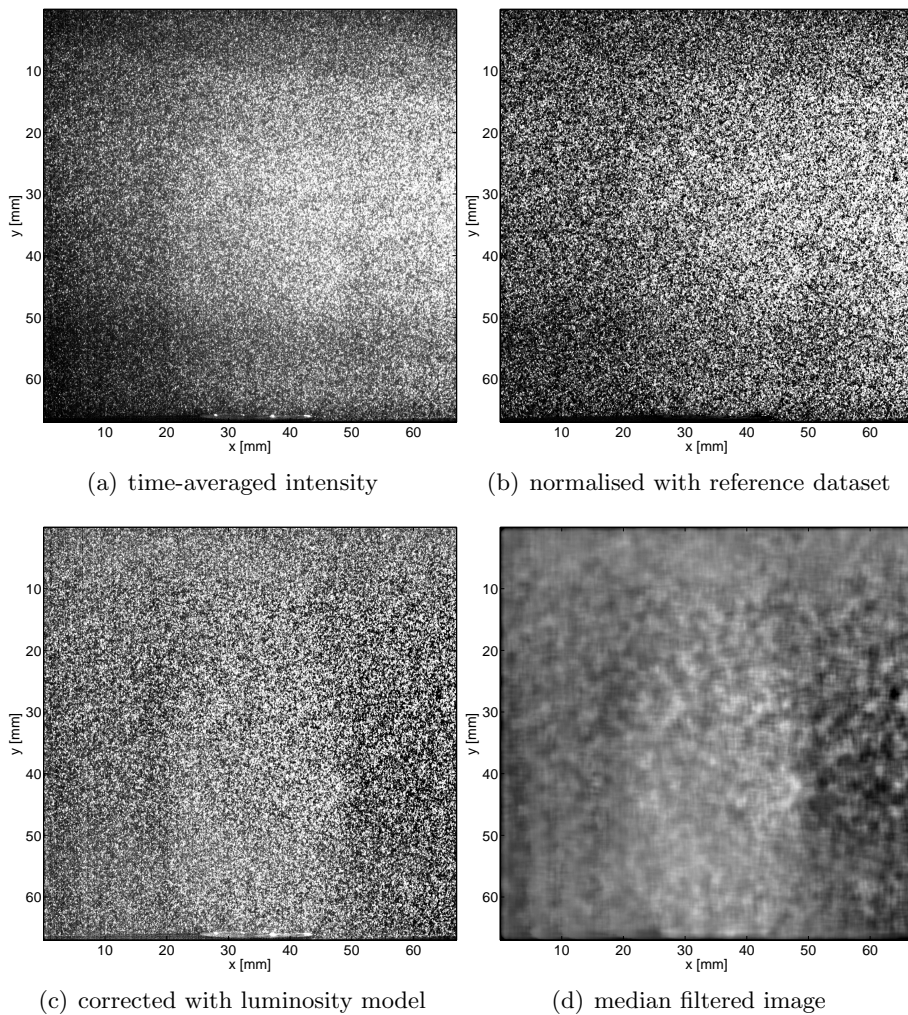


Figure 3.11: Illustration of the data processing steps: original time-averaged intensity image, taken at $U_\infty = 61$ cm/s (a); after normalisation with a reference dataset, taken at $U_\infty = 21$ cm/s, increased contrast (b); original image after correction with the luminosity model, increased contrast (c); filtered luminosity corrected image, increased contrast (d)

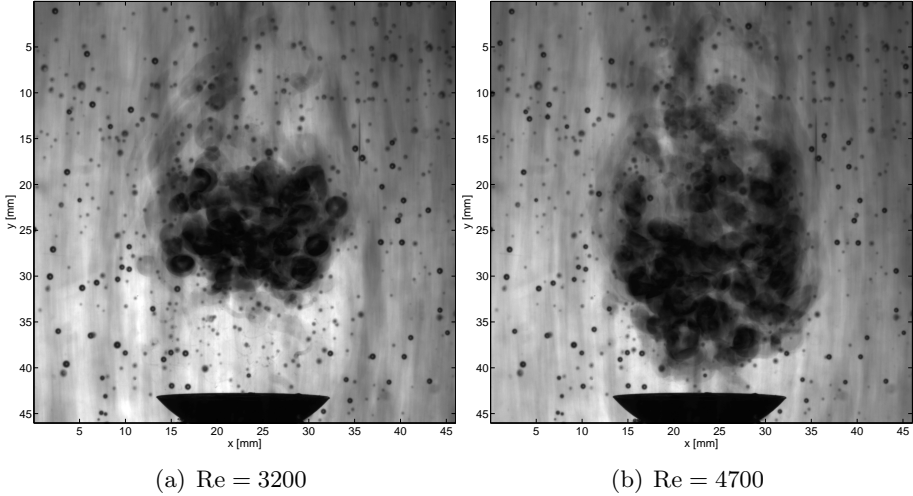


Figure 3.12: Concentration of gas bubbles in the wake of the spherical cap, measured with Shadowgraphy; note the weaker effect of buoyancy in the high Reynolds number case

sis. These methods were either too difficult to implement in the VerMeer facility, or the quality of the data obtained in several tests was not sufficient for a subsequent data analysis. Some more data analysis methods were also tried but gave insufficient results.

Small angle forward scattering is also a technique based on the light scattering of particles, but it uses a different angle to obtain higher scattering intensities and thereby a better signal. This method was not used with the VerMeer facility, but was used in collaboration with M. Dauda, A. Giffard and F. Zwaan, see Dauda (2011); Giffard (2011); Zwaan (2010).

Shadowgraphy is another technique to measure the concentration of a dispersed phase by recording the shadow of an object illuminated from a uniformly lit and diffuse light source. It worked well for visualising gas bubbles in the flow, see Fig. 3.12. The shadows of very small objects like the dispersed particles however gave too weak of a signal to do a meaningful data analysis. It was therefore only used for visualisation purposes.

An alternative way of correcting the inhomogeneities in luminosity

3 Experiments on Particle Entrainment

by making use of the intensity distribution of the fluorescent tracer particles. The fluorescence of the tracer particles is isotropic, but influenced by saturation. Close to the beam waist where the photon density is highest, integrating over the light sheet thickness gives lower values than further away from it. This is the result of fewer illuminated particles (the illuminated volume is smaller), with a saturated fluorescence due to the high light intensity. The images of the tracer particles were therefore without any use for the normalisation of the light intensity of the dispersed phase. Monchaux *et al.* (2010) used a method based on the counting of detected particles for their analysis of preferential concentration of particles in a flow. Despite the elegance of the method and its potential to allow for measurements of the fluctuations in the concentration, the strong inhomogeneities in the illumination hampered the particle detection to a degree that a homogeneous detection probability over the frame was unachievable.

4 Results on Particle Entrainment

4.1 The Wake of a Spherical Cap

4.1.1 Qualitative Description

Over a wide range of Reynolds numbers ($1500 < Re < 11600$), the boundary of the near wake is approximately an ellipsoid of rotation, see Fig. 4.2. Coppus *et al.* (1977) observed different types of wakes; they named the wakes measured in this work an *open turbulent* wake. The ellipsoidal shape is therefore only visible in the time-averaged flow fields; the instantaneous velocity fields do not show a closed stream line, see Fig. 4.1.

The time averaged velocity field of the near-wake behind a spherical cap at high Re is similar to a laminar one, which agrees with the observation made by Wu & Faeth (1994); Wu & Faeth (1995); Bagchi & Balachandar (2004) for wakes behind spheres. Parlange (1969) writes that the analytic flow solution for a laminar wake (constant vorticity ω_ϕ over the wake volume) is the so-called Hill-vortex (Hill, 1894), surrounded by a potential flow. Early experiments by Davies & Taylor (1950) supported that assumption, but Maxworthy (1967) pointed out correctly that this model implies a vanishing drag. The qualitative similarity to a spherical recirculation zone behind the spherical-cap bubble was also observed by Wegener & Parlange (1973) for bubbles and solid spherical caps in various fluids. The images of spherical-cap bubbles and their wakes taken by Bhaga & Weber (1981) also show this characteristic recirculation zone.

In the measurements at lower Reynolds numbers ($30 < Re < 250$), the average velocity field becomes increasingly asymmetric, see Fig. 4.3. In this range, the roll-up of the free shear layers happens locally at isolated locations only, leading to one (or few) helical vortex tube(s) separating from the shear layers. This leads to strong oscillations in the wake that were also observed and described by Coppus *et al.* (1977); Brücker (1996); Bagchi & Balachandar (2004).

The approximately elliptical shape of the flow pattern for the mean wake was found to change only marginally in the Reynolds-number range of $Re = 840 \dots 6600$ (based on the volume-effective diameter which is typically used for gas bubbles, $1500 < Re < 11600$ if the chord length of the spherical cap $\xi = 19$ mm is used as length scale) used for the present experiments, see Fig. 4.4. Slightly larger differ-

4.1 The Wake of a Spherical Cap

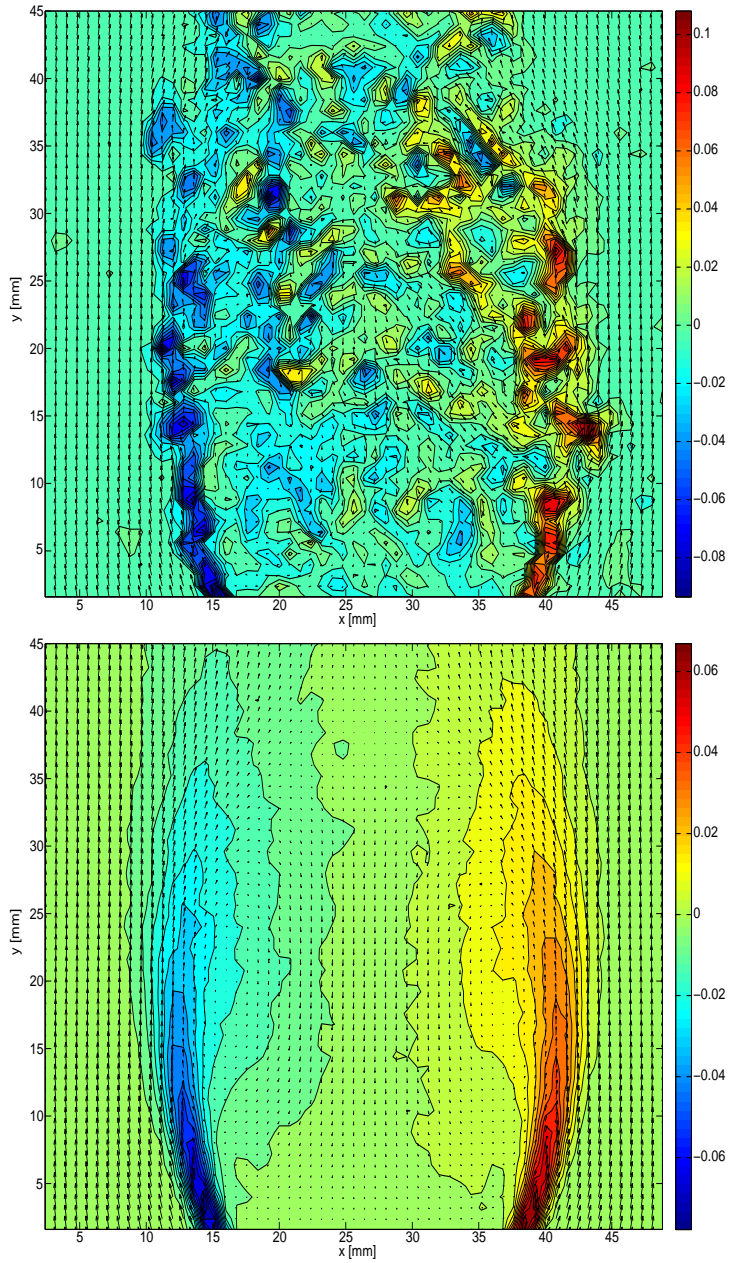
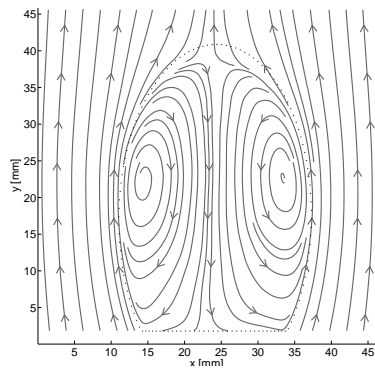
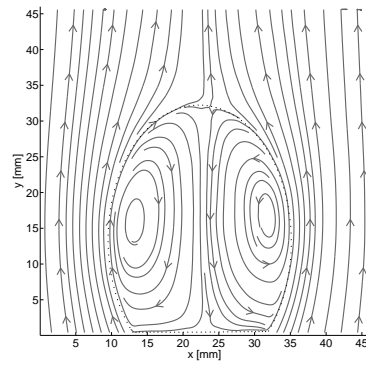


Figure 4.1: Instantaneous and time-averaged velocity field; background colour: vorticity

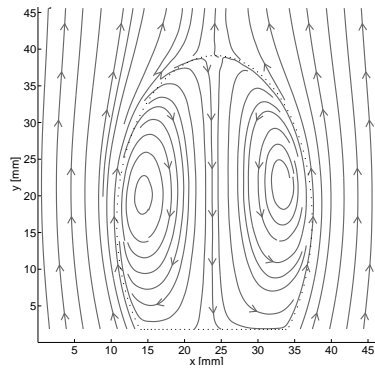
4 Results on Particle Entrainment



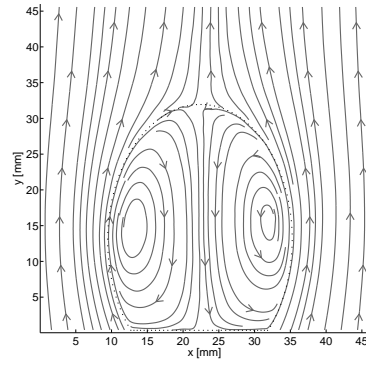
(a) $Re=1500$, low turbulence



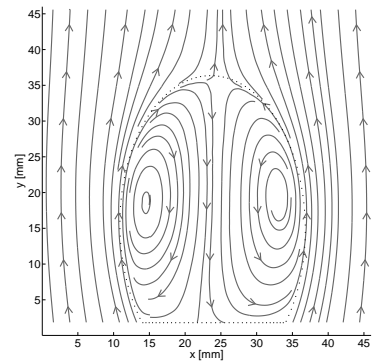
(b) $Re=1500$, high turbulence



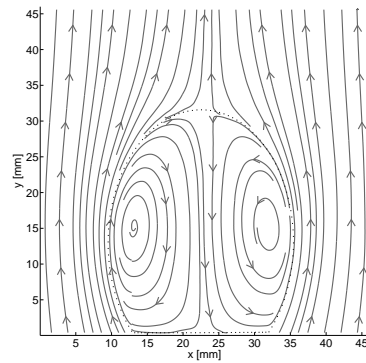
(c) $Re=4100$, low turbulence



(d) $Re=4100$, high turbulence



(e) $Re=11600$, low turbulence



(f) $Re=11600$, high turbulence

Figure 4.2: Comparison of the near wake for different Reynolds numbers and turbulence levels of the approaching flow (dotted line: fitted wake boundary)

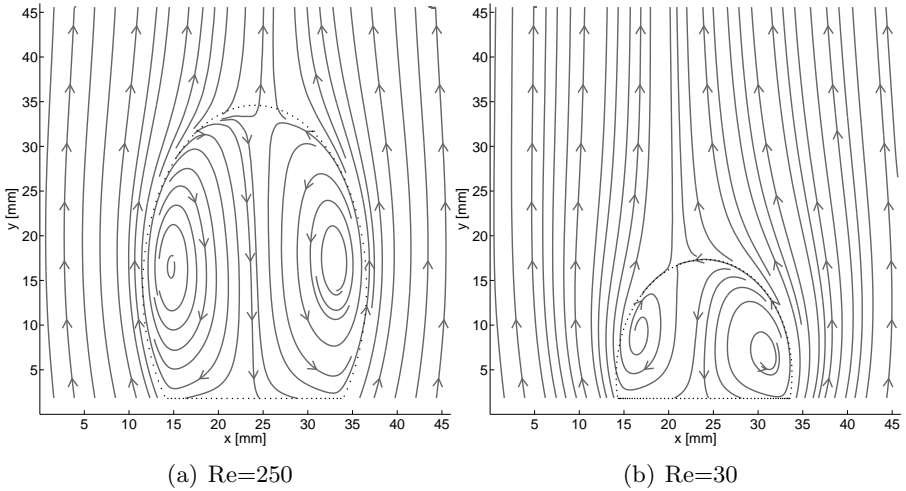


Figure 4.3: Deformation of the near-wake from the elliptical shape for low Reynolds numbers (dotted line: fitted wake boundary)

ences were found for the measurements done with the additional coarse grid #2 inserted (see Table 3.2), i.e. where the approaching flow has a relatively high turbulence level.

The main qualitative difference of the time-averaged flow fields is the longer downstream extension of the wake for a flow of low ambient turbulence approaching the spherical cap. In the high turbulence case, the wake is considerably shorter, whereas the difference in width can be neglected. There is no measurable change in the width of the wake for Reynolds numbers in the range $1500 < Re < 11600$. The downstream length of the wake is also almost constant, only a small decrease at $Re=11600$ can be observed. The relative size of the wake, h_{wake}/ξ , is defined as the ratio of the length of the near-wake h_{wake} (determined from the fit) and the chord ξ of the spherical cap ($\xi = 19$ mm). The relative size of the wake is either 2.0 or 1.66, for the low or the high turbulence case of the external flow, respectively. The width of the wake relative to the chord length is 1.44 in the low turbulence case and 1.36 in the high turbulence case.

The elliptical region defined by the closed streamlines is referred to as the ‘near wake’. However, for the range of Reynolds numbers

4 Results on Particle Entrainment

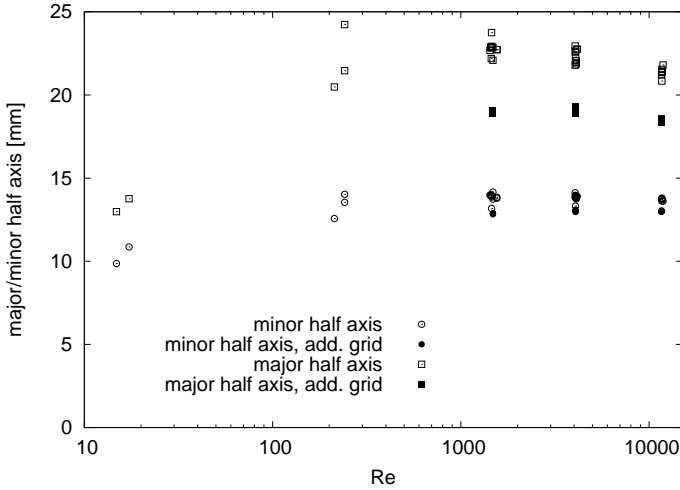


Figure 4.4: Wake size parameters over Reynolds number: Both the major and the minor half axis of the detected ellipsoidal wake boundary vary only weakly in the range $1500 < \text{Re} < 11600$.

($1500 < \text{Re} < 11600$) used in the present measurements, the flow behind a spherical-cap obstacle is an open turbulent wake. Therefore the instantaneous velocity fields differ considerably from their time-average. From the rim of the spherical cap, free shear layers evolve that become unstable and break up almost instantaneously. This is the main source of turbulence in this flow. The turbulence is transported into the near and far wake of the spherical cap. So, we divide the observed flow volume into three main parts: the near-wake, the shear layers, and an outer flow region. Note that only a small portion of the far wake is located inside the observation volume.

4.1.2 Flow Length and Time Scales

The width of the wake gives only a rough estimate of the largest scales in the flow. The integral length scale L of the wake turbulence was estimated by using the integral of the longitudinal autocorrelation function of the streamwise velocity component. It was found to be approximately constant over the flow velocity range. The integral length scale is estimated at $L = 4.5 \pm 1.1$ mm for the centre of the wake, and at L

Table 4.1: Estimates of relevant turbulent length and time scales, based on the expressions for isotropic turbulence and an integral length scale of 5.5 mm (see text) and a relative turbulence level of 0.2

Re	U_∞ [m/s]	Re_L	λ [mm]	Re_λ	ϵ [mm ² /s ³]	η_K [μ m]	τ_K [ms]
1500	0.08	85	2.3	36	$6.9 \cdot 10^2$	195	38
4100	0.21	235	1.4	59	$1.4 \cdot 10^4$	91	8.4
11600	0.61	670	0.8	100	$3.3 \cdot 10^5$	42	1.7

= 5.8 ± 0.6 mm for the rear stagnation point of the wake. An integral length scale of $L = 5.5$ mm (i.e., $0.22R_{\text{sphere}}$ and 0.29ξ) is used for the estimates presented in Tab. 4.1. It should be noted that these estimates are valid for the region occupied by the open turbulent wake (including the boundary of the near wake), and not for the outer flow region and the shear layers.

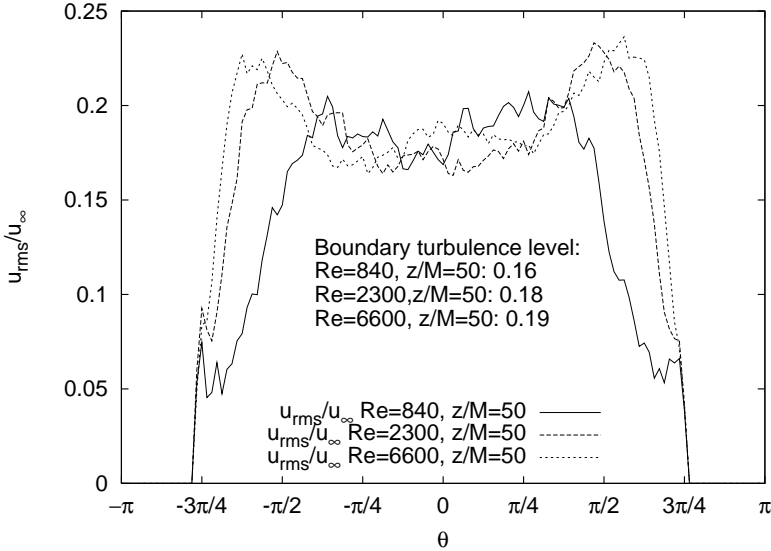
The Taylor length scale λ and Kolmogorov length scale η_K are estimated from (Tennekes & Lumley, 1972)

$$\frac{\lambda}{L} = \sqrt{\frac{15}{A}} Re_L^{-1/2}, \quad \epsilon = 15\nu \frac{u_{\text{rms}}^2}{\lambda^2}, \quad \eta_K = \left(\frac{\nu^3}{\epsilon}\right)^{1/4}, \quad (4.1)$$

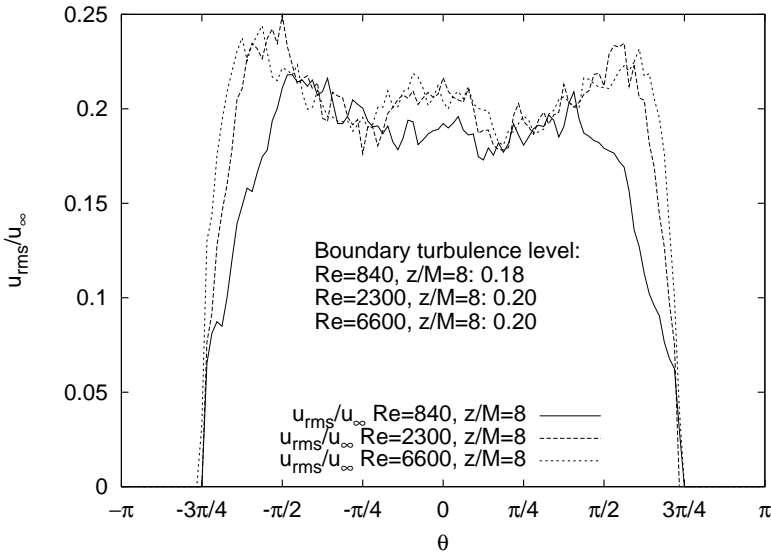
with: $Re_L = u_{\text{rms}}L/\nu$, and where it is assumed that the turbulence in the wake is nearly isotropic ($A \approx 1$).

The turbulence properties of the external flow approaching the spherical cap are only of limited importance for the mixing in the conical region of the open turbulent wake behind the spherical cap, which includes the boundary of the near wake. The turbulence there is dominated by the shedding of vortices from the free shear layers. Qualitatively, the stronger momentum exchange between the outer flow and the wake causes wider shear layers and a smaller velocity difference, thereby weaker velocity gradients and weaker vortex shedding. The turbulent kinetic energy (and thereby the rms of the velocity) was still found to be of similar level (Warncke *et al.*, 2009). The fluctuating component of the velocity normal to the boundary is directly proportional to the local turbulent transport over the boundary. Fig. 4.5. shows that it

4 Results on Particle Entrainment



(a) low upstream turbulence level



(b) high upstream turbulence level

Figure 4.5: Standard deviation u'_n of the velocity normal to the wake boundary relative to the free-stream velocity U_{∞} as a function of the polar angle θ , for an approaching flow with: (a) low turbulence level (less than 3%) and (b) high turbulence level (15–21%). The rear stagnation point is located at $\theta = 0$; the shear layers are found at $|\theta| > \frac{\pi}{2}$. The rim of the spherical cap is at $|\theta| = 13\pi/18 (\approx 3\pi/4)$

is nearly constant at the downstream side of the wake ($|\theta| \leq \frac{\pi}{2}$). The weaker fluctuations for $|\theta| > \frac{\pi}{2}$ for the lower flow velocities are explained by the more stable shear layers, with the vortex shedding starting further downstream from the rim of the spherical cap. The graph shows slightly higher fluctuations near the rear stagnation point and in the shear layers for the high turbulence level flow case.

4.2 Particle Transport over the Wake Boundary

4.2.1 Analysis of the Flux Data

Based on the continuity equation in the stationary state (see Sec. 3.2.3 for more details), the existence of a concentration gradient in the wake implies a negative (inward) particle flux if the concentration is higher in the near-wake than in the outer flow. In other words, the particle velocity has, although it is strongly correlated to the fluid velocity for low inertia particles with a small response time, a component normal to the wake boundary. The integrals of the measured dispersed phase velocities over the wake boundary should therefore be negative if there is a preferential concentration of particles in the wake.

The measurement data given in Tab. 4.2 shows that a statistically significant inward particle flux can indeed be observed for the measurements done with the 3M S60 particles. With increasing flow velocity, the magnitude of the flux also increases approximately linearly, contrary to the quadratic increase suggested by Eq. (2.48). The results obtained from the measurements with other particle types are less consistent: the magnitude of the measured fluxes is of the order of the measurement uncertainty, which also explains the occurrence of positive signs for the flux (outward flow). In these cases, the measurement uncertainties are too high to draw a conclusion. It should be noted that the values given in Tab. 4.2 are averaged from several data sets that were measured under identical conditions. The large uncertainties therefore reflect the scatter among the different measurements.

Fig. 4.6 shows the graphs obtained by plotting the measured flux values against the predictions from the spherical and ellipsoidal wake model. Each point in the graph represents one single dataset here. The linear line is obtained from a least-square fit to the data sets in the small boxes in each graph, thereby excluding 6 data sets as “outliers”. For

4 Results on Particle Entrainment

u_∞	turb. level	\dot{V} [mm ³ /s]	$SE_{\dot{V}}$ [mm ³ /s]
3M S60 55 μ m, 0.6g/cm ³			
9.09E-04	0.5545	-3.72E+1	1.27E+1
7.79E-04	0.4897	-4.79E+1	5.74E+0
1.12E-02	0.1192	-4.42E+2	3.01E+1
7.66E-02	0.1623	-2.92E+3	2.48E+2
2.14E-01	0.1818	-5.05E+3	6.85E+2
6.13E-01	0.1882	-2.33E+4	1.93E+3
3M S22 55 μ m, 0.22g/cm ³			
1.27E-02	0.1179	1.69E+02	3.46E+2
7.62E-02	0.1632	-9.79E+02	1.01E+3
2.13E-01	0.1822	-2.03E+03	2.89E+3
6.15E-01	0.1876	-2.09E+03	8.30E+3
3M K1 110 μ m, 0.125g/cm ³ low turbulence case			
7.79E-02	0.1596	-3.22E+2	4.27E+2
2.14E-01	0.1997	-2.96E+3	2.42E+3
6.12E-01	0.2044	-1.22E+3	1.71E+3
3M K1 110 μ m, 0.125g/cm ³ high turbulence case			
7.99E-02	0.1558	-7.20E+2	5.40E+2
2.17E-01	0.1794	-1.60E+3	1.25E+3
6.20E-01	0.1862	+1.84E+3	1.58E+3

Table 4.2: Summary of the particle flux measurements; a positive sign means outward flow

4.2 Particle Transport over the Wake Boundary

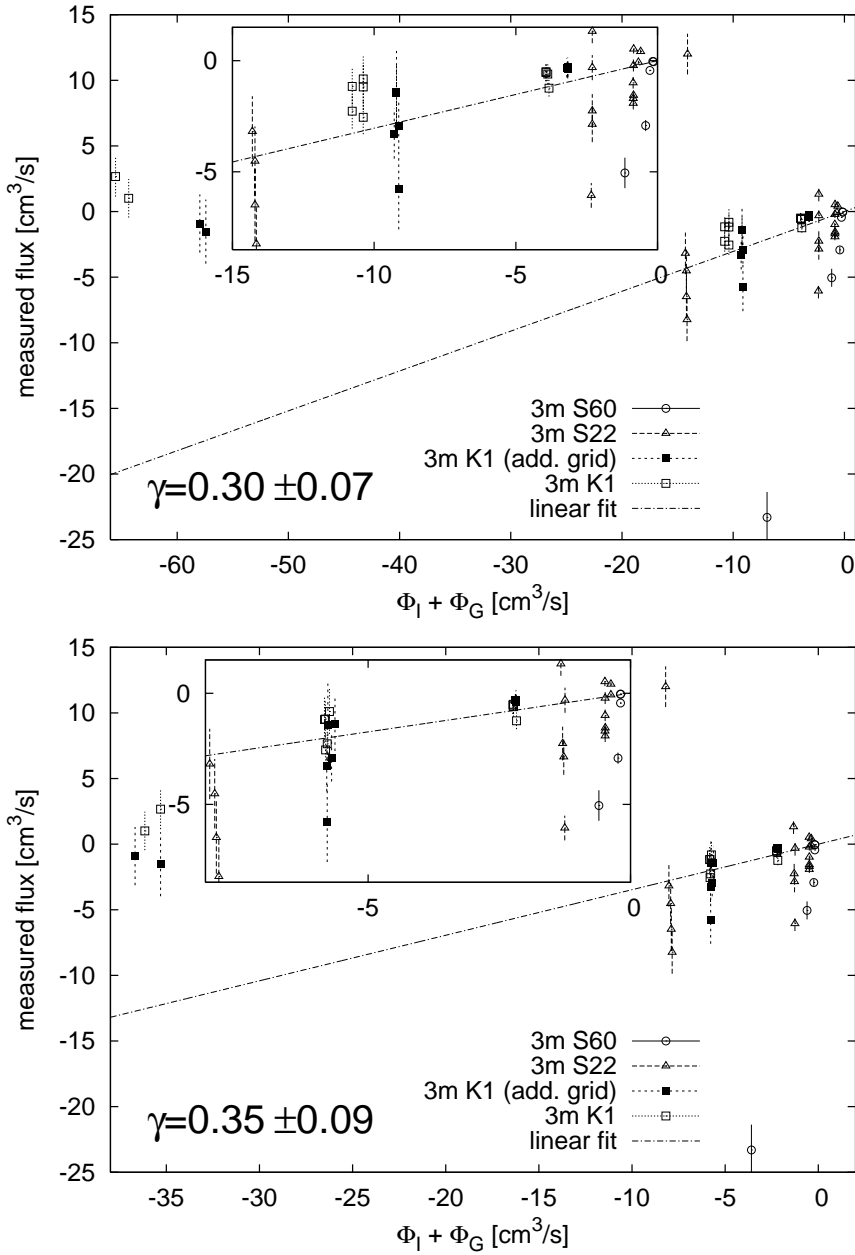


Figure 4.6: Measured particle flux versus the estimated flux from Eq. (2.48) and Eq. (2.56), spherical wake model (top) and ellipsoidal wake model (bottom). The linear fit is obtained from the data in the insets.

4 Results on Particle Entrainment

both models there is a weak correlation with the experimental results. The variance of the residuals of the fit is approximately 22 and 17, showing that the scatter in the data is approximately a factor of 4 to 5 higher than expected from the statistical uncertainties. A comparison with a perfect model should reveal a slope near unity; therefore both models overpredict the experimental outcome by approximately a factor of 3. If the outliers are included into the fit, a slope around zero is obtained in both cases.

4.2.2 Discussion of the Flux Measurement Results

In conclusion, the uncertainties of the performed particle flux measurements are too high to allow a meaningful comparison with and a validation of the particle entrainment model. This is not a result of the statistical uncertainties, yet there remain systematic errors in the measurements. One likely source of errors is in the alignment of the two cameras: An alignment error, despite being small, would cause a comparison of the particle fluxes integrated over different wake boundaries, see Sec. 3.2.1. This error, for the obtained accuracy in the alignment, is of the order of the flux difference for measurements with particles with a small response time. It can nevertheless be larger in combination with other systematic errors, namely the assumption of a symmetric near-wake for the time-averaged flow. An integration over an asymmetric wake (e.g. due to a misalignment of the spherical cap) can cause non-zero fluxes even in the continuous phase, because the weighting applied for the surface area is based on the assumed symmetry. These non-zero fluxes are indeed obtained for the continuous phase.

4.3 Preferential Concentration

4.3.1 Dependency of Particle Concentration on the Particle Properties

According to the model described in Sect. 2.3, the concentration increase in the wake can be expected to be of the order of a few percent for the particles in Table 4.3. For such small changes in the concentration it is challenging to perform quantitative measurements. Variations in the particle-image exposure, due to angle-dependent Mie-scattering,

Table 4.3: Overview of the properties of the particles that were used for the dispersed phase, where d_P is the particle diameter, ρ_P the density of the particles, τ_P the particle response time, β the density ratio with respect to the working fluid as defined in (2.42), and v_P the particle terminal velocity (where a negative value means the particles are buoyant).

particle type	material	d_P [μm]	ρ_P [g/cm^3]	τ_P [ms]	β [-]	v_P [mm/s]
SiLi	glass spheres	55	2.5	0.50	0.5	+0.25
3M S60	hollow glass sph.	55	0.6	0.19	1.36	-0.067
3M S22	hollow glass sph.	55	0.22	0.12	2.08	-0.13
3M K1	hollow glass sph.	110	0.125	0.42	2.4	-0.59
QCel 7014	hollow glass sph.	125	0.14	0.56	2.34	-0.75
Cennasphere	ceramic spheres	300	0.6	5.5	1.36	-1.50

a diverging light sheet, and the light blockage of particles were found to be of the same order of magnitude (if not larger) as the anticipated variations in the particle concentration. This makes it impossible to base any quantitative concentration measurements on the directly recorded image intensities. Therefore, the average scattered light intensity for a given particle type at one free-stream flow speed was normalised with the recorded scattered light intensity recorded at a lower free-stream flow speed. The rationale behind this is that both data sets have been recorded at nearly identical optical conditions (provided that the relative change in concentration is small) and that the relative change in concentration is always smaller for the lower free-stream flow speed, cf. (2.50) where the relative change in concentration is proportional to U_∞ (for a constant turbulence level). In practice this means that we use the data set recorded for $\text{Re} = 840$ to normalise the data taken at $\text{Re} = 2300$ and $\text{Re} = 6600$. It is also possible to use the data taken at $\text{Re} = 2300$ to normalise the $\text{Re} = 6600$ data; this was occasionally done when no measurement data was available for $\text{Re} = 840$.

Table 4.4 shows a summary of results from concentration measurements for different particle types. The values represent the relative

4 Results on Particle Entrainment

Table 4.4: Overview of selected measurement results for the relative change (in %) of the mean particle concentration in the near wake compared to the concentration in the external flow, for different flow Reynolds numbers. The results are for the low turbulence level flow data. Uncertainty margins indicate the standard error of the measurement result.

	R_P [μm]	ρ_P [g/cm^3]	Re = 840 [%]	Re = 2300 [%]	Re = 6600 [%]
SiLi	55	2.5	-1.5 ± 1.5	0.6 ± 1.6	-0.7 ± 3.7
3M S60	55	0.6	0.0 ± 0.4	0.0 ± 0.7	0.1 ± 0.7
3M S22	55	0.22	-0.6 ± 0.8	0.6 ± 1.2	1.6 ± 2.1
3M K1	110	0.125	-1.4 ± 0.7	1.4 ± 0.9	3.8 ± 1.8
QCel 7014	125	0.14	–	3.2 ± 0.7	9.6 ± 1.7
Cennasphere	300	0.6	–	–	21.0 ± 7.5

increase in concentration over the outer flow, obtained with the normalisation method and subsequent correction described in Sec. 3.2.4. One can conclude that small particles show hardly any measurable effect, whereas increasingly higher concentrations could be measured for buoyant particles with larger diameters. For particles with a density that is larger than that of the fluid a small decrease of the particle concentration in the wake was found, in accordance with our model.

Figure 4.7 shows the scaling of the change in particle concentration relative to the outer flow as a function of the Stokes number defined in (2.52) divided by the turbulence level $\text{TL} = u_{\text{rms}}/U_\infty$. The error bars denote the standard deviation of concentration increase for a number of measurements done under identical conditions, and normalised with the same reference data set. Filled symbols are measurements with a strongly turbulent flow approaching the spherical cap; and the inset in Fig. 4.7 shows a magnified version of the plot close to the origin. Buoyant particles (i.e., with a positive characteristic Stokes number according to our definition) show an increase in particle concentration in the near wake, as it is predicted by our simple model. For particles with a density that is higher than that of the fluid (i.e., the “SiLi” particles in Table 4.4, for which $\tau_{P^*} < 0$ and thereby $\text{St} < 0$, see Eq. (2.54)

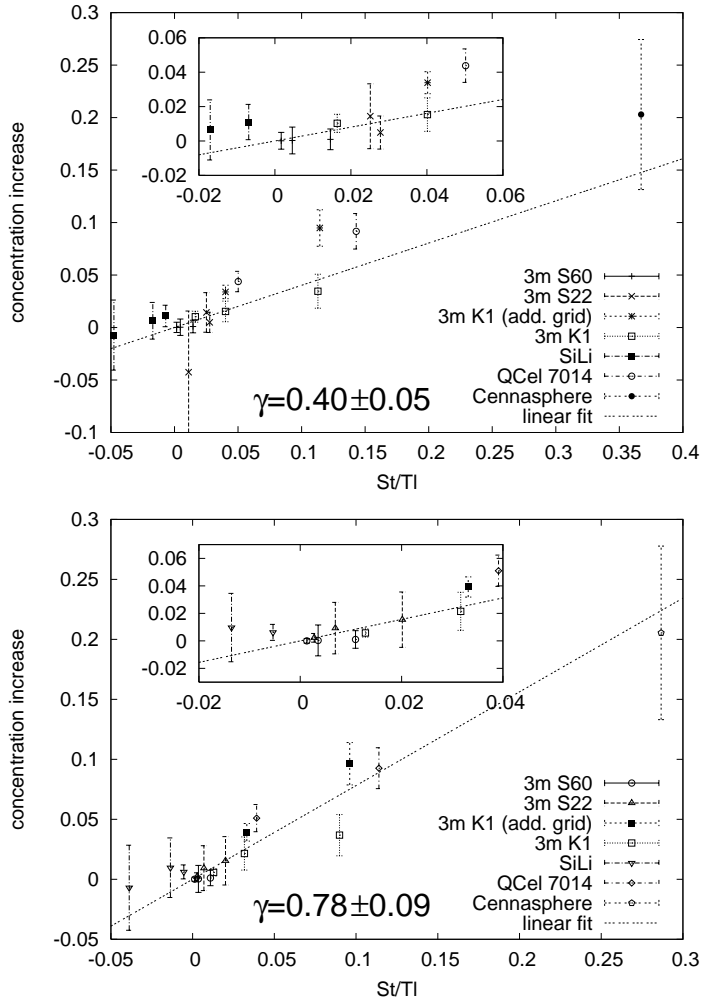


Figure 4.7: Increase in particle concentration inside the near-wake relative to the outer flow over the ratio of the characteristic Stokes number and the turbulence level; the concentration increase is corrected for the contribution of Fr^2 (see text); spherical wake model (top) and ellipsoidal wake model (bottom); note the different definitions of the St and Fr for the spherical wake (characteristic length scale R_{wake}) and the ellipsoidal wake (characteristic length scale major half-axis a)

4 Results on Particle Entrainment

in Sec. 2.3.1), two data sets support the predictions of the model with a decrease in concentration, whereas the other data set shows a slight increase. Neither the increase nor the decrease found in these four data sets is statistically significant, though. Please note that the measurement uncertainty, as indicated by the error bars, is relatively large in comparison to the magnitude of the relative change in concentration. This is due to the rather small changes in concentration that occur for small particles, and the systematic errors resulting from the normalisation method. Nevertheless, the line fitted to the experimental data in Figure 4.7 reveals that the experimental data correlates reasonably well with our simple model within the estimated statistical uncertainty of the experimental data. The value of the proportionality constant γ , which absorbs a number of unknown constants, is found to be $\gamma = 0.78 \pm 0.09$. A similar fit gives $\gamma_{\text{spherical wake}} = 0.40 \pm 0.05$ for the spherical wake model, with the change in slope resulting in the differences of the definition of the characteristic Stokes and Froude number. The rms of the normalised residuals is 1.24 ($\chi^2 = 1.54$) for the spherical wake model and 1.14 ($\chi^2 = 1.30$) for the elliptical wake model, which shows that the linear fit describes the data sufficiently well.

It should be noted that the condition in (2.58), i.e. a high Froude number, is generally not fulfilled for most of the measurements. This implies that the gravitational term cannot be omitted in Eq. (2.41–2.44). Note that for the correction of the experimental data with the Froude number Fr^2 in Fig. 4.7, the sign of the gravitational acceleration was changed. This is necessary, as for the present measurements gravity was pointing in a direction that is opposite to the direction of the incoming flow. (Please note that the model has been derived for a rising spherical-cap gas bubble in a frame of reference moving with the bubble, for which the gravitational acceleration is in the direction of the fluid motion.)

The model derived for an elliptical wake shows a marginally better agreement with the experimental data than the spherical wake model, although the difference is small and statistically not significant (relative errors of the fit of 10.9% for the elliptical versus 12.0% for the spherical wake model).

4.3.2 Discussion of the Concentration Measurements

Contrary to the flux measurements in Sec. 4.2, the preferential concentration of particles is visible in the data, despite still high measurement uncertainties. There is a clear linear trend in the experimental results that supports the prediction of the elliptic wake model, although the model still somewhat overpredicts the preferential concentration found in the experiments. The spherical wake model shows the same linear trend, but overpredicts the experimental data to an even higher degree.

The measurement uncertainties of the concentration data are certainly higher than desirable. This is a result of the normalisation of each data set with a (also measured) reference data set to remove the contribution of the anisotropic Mie scattering. This normalisation amplifies the measurement uncertainties of each data set, though the nature of the uncertainties is still statistical. An increase in the number of measurements would therefore reduce these uncertainties. The normalised residuals of the linear fit (reduced χ^2) close to unity further support the statistical nature of these uncertainties. Increasing the number of samples was limited by the loss of dispersed particles in the flow over the total duration of the experiment (approximately 40 minutes for 1024 records) and by the sampling rate of the image acquisition system (1 record per 2 seconds). For an average Signal-to-Noise-Ratio of 10 for a single data set (the geometric mean of the SNR in Tab. 4.4 is 0.8), approximately 150,000 records are needed if a Gaussian distribution of the uncertainties is assumed. The convergence is still much worse even for such a high number of samples, as the ratio distribution of two Gaussians is a Cauchy distribution.

The results can also be improved by using longer integration times, as sharply imaged particles are only required for a subsequent PIV analysis and not for the analysis of time-averaged concentrations. The raw data was intentionally optimised for measuring the particle transport over the wake boundary via PIV instead for concentration measurements, a circumstance which takes its toll here. There are in principle also other possible methods for the concentration analysis that are based on detected particles (e.g. Monchaux *et al.*, 2010) instead of averaging the scattered light intensity. However, these methods require a careful normalisation for a homogeneous detection probability over the frame, something that turned out to be too difficult to achieve during this

4 Results on Particle Entrainment

work.

5 Surface Attachment

5 Surface Attachment

Dispersed particles are not only transported due to the local entrainment in the bubble wake, but also — and potentially much more efficiently — by collision and attachment to the bubble surface. Historically, this part has been studied much more thoroughly than the wake entrainment, inasmuch that there is a considerable amount of literature dating back to the beginning of the 20th century (see e.g. the chapter on the “Mechanism of Collection” in Gaudin, 1957).

The following chapter contains a description of the measurements of the attachment rates on a single bubble trapped in a decelerating downward flow. It contains of two parts: Sec. 5.1 summarises the theoretical background needed to understand how particles can attach to the surface of the bubble, namely the particle-bubble encounter, the attachment and the possible detachment processes. The (turbulent) encounter is in particular relevant for the derivation of the attachment model in Sec. 5.1.4 that is later compared to the data obtained from the experiments. The theory of the attachment and the detachment process are not directly needed for the derivation of this model, but are required for the interpretation of the results, as the attachment probability strongly depends on particle properties. The detachment is also not relevant to the performed experiments,¹ but the detachment theory in Sec. 5.1.3 gives an indication of the influence of turbulence on the attachment process, a field that not well-understood yet. The second part of the chapter describes the experiment in Sec. 5.2 and the results in Sec. 5.2.4 and Sec. 5.2.5.

5.1 Models for Particle-Bubble Attachments

According to modern understanding (Nguyen *et al.*, 1997; Nguyen & Schulze, 2004), the whole flotation process can be divided in to three stages:

- the process of the approach of the particle towards the bubble surface is called the encounter or collision,
- the attachment describes the physical contact between the particle and the gas-liquid interface, and

¹Only bubbles were studied where no detachment can be observed; otherwise, it is not possible to interpret the increase in surface concentration as attachment rate

- after a successful attachment, the particle might become detached again.

The particle-bubble attachment is a process that in itself consists of three steps:

- the thinning of the liquid film between the particle and the gas-liquid interface to a critical thickness,
- the rupture of the film with the formation of a three-phase contact (TPC) line, and
- the expansion of the TPC line from the critical radius and stabilisation of the TPC at the equilibrium position.

The probability P_{float} of a particle being transported by the bubble (excluding wake effects and assuming statistical independence) is therefore described with the product (Yoon & Luttrell, 1989)

$$P_{\text{float}} = P_{\text{enc}}P_{\text{att}}(1 - P_{\text{det}}) , \quad (5.1)$$

with

$$P_{\text{att}} = P_{\text{thin}}P_{\text{rupt}}P_{\text{tpc}} . \quad (5.2)$$

Eq. (5.1) is generally accepted in the flotation literature, see e.g. Nguyen & Schulze (2004). There are possible doubts about the validity of this equation, as P_{enc} and P_{att} are not completely independent (e.g. the end of the encounter process is equal to the beginning of the attachment process, a somewhat arbitrary border). However, for the purpose of this work, only the combined probability of both the encounter and the attachment is relevant for the measurements, and the detachment was excluded using air bubbles without smooth surfaces and without a sharp rim.

In the following section, an overview is given over each part of the process, including a discussion of models from the literature.

5.1.1 Particle-Bubble Encounter

General Idea

The particle encounter describes the approach of the particle to the bubble, and in particular the coordinates — the so-called collision angle — at which this interaction occurs. There is some ambiguity in this

5 Surface Attachment

definition (see chapter 9 of Nguyen & Schulze, 2004, for an extended discussion), as there is no sharp limit at what distance this encounter occurs. It is generally accepted to use a distance of R_P to the undeformed interface. At this stage, the interface is slightly deformed and a thin liquid film is created.

Historically, the oldest system studied consisted of a single, spherical bubble rising in a quiescent fluid. In this geometry, a stationary particle in the path of the bubble collided with it at a certain polar angle (in spherical coordinate system of the bubble), the so-called *collision angle* ϕ_C . In a potential flow (see 9.3 of Nguyen & Schulze, 2004), this collision angle is only a function of the radial distance of the initial particle position from the future path of the bubble, the so-called *encounter radius*. The maximum encounter radius at that a collision can occur is the *grazing radius* R_C . The encounter efficiency can then be defined by the ratio of the swept area (the circular disc around the future path of the bubble) to the interception area (the circular disc of maximal radius that is swept by the bubble)

$$E_C = \left(\frac{R_C}{R_B + R_P} \right)^2 . \quad (5.3)$$

Using the collision angle and the fact that the collision radius can be written as $R_C = (R_B + R_P) \sin \phi_C$, the encounter efficiency is solely a function of the collision angle

$$E_C = \sin^2 \phi_C . \quad (5.4)$$

Empirical Theories and Heuristics

For fully deterministic processes, the encounter efficiency would equal the encounter probability P_{enc} , in more realistic cases (turbulent flows, complex bubble shapes) it is very difficult to determine an encounter efficiency from purely geometrical reasoning. In general, an effective collision angle ϕ_C can be found such that Eq. (5.4) gives an approximate description of the collision probability over the polar angle. According to Dobby & Finch (1987), the probability P_{enc} can be related to the encounter rate $N_{\text{enc}}(\phi)$ as a function of the collision angle by

$$N_{\text{enc}}(\phi) \propto \left(\frac{\sin \phi}{\sin \phi_C} \right)^2 \quad \text{for } \phi \leq \phi_c , \quad (5.5)$$

and $N_{\text{enc}} = 0$ for $\phi > \phi_c$. This heuristic relation for the number of colliding particles over the polar angle was obtained from numerical tracking of particles (Stokes drag only) and a potential flow around a sphere, as well as experimental data (see Dobby & Finch, 1987, for more details).

Yoon & Luttrell (1989) and Nguyen (1994) specify relations of the type

$$P_{\text{enc}} = A \left(\frac{R_P}{R_B} \right)^n \quad (5.6)$$

for the particle collision probability as a function of the particle and bubble radius, and give the scaling factor A and the exponent n for different flow conditions. Yoon (2000) gives a more extensive historical overview on models of this type.

Turbulent Particle-Bubble Encounter

The flotation literature on the particle-bubble encounter in a turbulent flow is limited, see chapter 11 of Nguyen & Schulze (2004). In oceanography on the contrary, the problem of predator-prey encounters has been studied extensively for almost two decades (MacKenzie *et al.*, 1994; MacKenzie & Kiorboe, 2000). The standard model for this problem is a perfectly absorbing sphere in a turbulent flow. It is assumed that the turbulent particle flux over the boundary of the sphere is equivalent to the particle encounter problem. The following discussion is — unless otherwise noted — based on Mann *et al.* (2005); Pécseli & Trulsen (2010); Pécseli *et al.* (2012).

Using scaling arguments only, Pécseli & Trulsen (2007) derive an expression for the turbulent particle flux. The dispersed phase is treated as a passive scalar. The diffusion equation for the particle density in spherical coordinates is

$$\frac{\partial}{\partial t} n(\xi, \tau) = \frac{1}{\xi^2} \frac{\partial}{\partial \xi} \xi^2 D(\xi) \frac{\partial}{\partial \xi} n(\xi, \tau), \quad (5.7)$$

using normalised coordinates $\xi = r\epsilon^{1/4}/\nu^{3/4} = r/\eta_K$ and $\tau = t\sqrt{\epsilon/\nu} = t/\tau_K$. With the boundary condition $n(R, t) = 0$ (perfectly absorbing sphere with radius R) and a vanishing left-hand side (stationary state),

5 Surface Attachment

Eq. (5.7) can be rearranged to

$$n(\infty) - n(R/\eta_K) = \int_{R/\eta_K}^{\infty} \frac{dn(\xi)}{d\xi} d\xi = \int_{R/\eta_K}^{\infty} \frac{J_0}{\xi^2 D(\xi)} d\xi. \quad (5.8)$$

The constant $J_0 = 4\pi R^2 \left. \frac{dn}{dr} \right|_{r=R}$ represents the total diffusive particle flux. In the inertial subrange, the diffusion coefficient is modelled as $D = C_1 \epsilon^{1/3} r^{4/3}$ (the model of Richardson, 1926), resulting in the turbulent encounter rate (more exactly, the steady-state flux into a perfectly absorbing sphere of radius R) as

$$\frac{J_0}{n_0} = \frac{28\pi}{3} C_1 \epsilon^{1/3} R^{7/3} \quad (5.9)$$

for the inertial range $\eta_0 < R < L$. In the viscous subrange $0 < R < \eta_0$, the same analysis gives

$$\frac{J_0}{n_0} = 12\pi C_2 R^3 \sqrt{\frac{\epsilon}{\eta}} \quad (5.10)$$

using the diffusivity $D = C_2 r^2 \epsilon / \nu$. On a per-unit-area basis, this is equivalent to a scaling $\propto R$ in the viscous and $\propto R^{1/3}$ in the inertial range.

By translating these results to the encounter rates of bubbles in a turbulent flow, it can be seen that the result for the viscous subrange is not relevant, as bubbles smaller than η_K are not very common in the relevant applications. Nevertheless, the result for the inertial range can be directly applied; see Sec. 5.1.4. The scaling $\propto R_B^{1/3}$ implies here that smaller bubbles are considerably more efficient ($\propto R_B^{-8/3}$) due to higher possible numbers if the total gas volume $V = N_B 4/3\pi R_B^3$ is constant. Using $\epsilon \propto u_{rms}^3 / L$ also shows that there is a linear scaling with the standard deviation of the turbulent velocity fluctuations, a result that qualitatively agrees with the observations made in Sections 5.2.4 and 5.2.5. It should be noted that — by the nature of the passive scalar assumption made in the derivation — no scaling relations can be obtained for the size and other properties of the dispersed particles.

5.1.2 Particle Attachment

According to current understanding, the attachment process is further split into sub-parts, which are the collision period (involving a deformation of the gas-liquid interface and possible oscillations of the particle)

and the contact period (the particle sliding along the interface), after which the thin film ruptures and a stable three-phase contact line is created. Following this scheme, Nguyen & Schulze (2004) give a comprehensive overview of models for each step.

In the following part the models are discussed that either simplify the process by describing drainage times (the induction time in contact time theories) or try to solve a system of differential equations containing the equation of motion of a particle and a PDE for the thin film. The collision step subsequent to the encounter is not discussed here; it is however implicitly solved in the latter type of models. Nguyen *et al.* (1997) discusses the influence of the simplifications $P_{\text{rupt}} = P_{\text{tpc}} = 1$ (the attachment probability is therefore only related to the probability of the liquid film thinning to a critical thickness). For a discussion of all other problems the reader is referred to Nguyen & Schulze (2004). The thin-film drainage problem is also discussed in the frame of general coalescence problems.

Contact Time Theories

Due to the complexity and large range of scales of the processes involved in the particle attachment, so-called *contact time theories* have been developed that introduce the *induction time* t_I . It is assumed that this time is representative for the mean time needed from the encounter (the particle approaches the bubble surface to a certain distance) to the successful attachment. It is further assumed that a particle attaches to the gas-liquid interface if the *sliding time* t_S is larger than t_I . The sliding time is the time between the first geometric contact between bubble and particle (the moment of encounter) until the particle trajectory separates² from the bubble surface again.

The sliding time can be derived from the geometry of the problem: By integrating the tangential particle velocity $v_{P,\phi} = u_\phi + \tau_P g \sin \phi$ (which excludes all terms from the equation of motion besides Stokes drag and gravity), the resulting formula (Sutherland, 1948)

$$t_S = (R_P + R_B) \int_{\phi_C}^{\phi_m} \frac{d\phi}{v_{P,\phi}(\phi)} \quad (5.11)$$

²If the particle attaches to the surface, this trajectory is of course mere theoretical

5 Surface Attachment

gives a relation for the sliding time t_S as a function of the collision angle ϕ_C and the angle of separation from the bubble surface ϕ_m (the minimum and the maximum angle of contact).

To solve equation Eq. (5.11), an analytical expression is needed for the tangential particle velocity $v_P(\phi)$. The first approach was done by Sutherland (1948), assuming inertia-less particles travelling on the stream lines of a potential flow around a spherical gas bubble. More sophisticated models with also more assumptions and/or including empirical correlations have been presented by Nguyen *et al.* (1998) and Yoon & Luttrell (1989). A good overview of even more contact time models is given by Nguyen & Schulze (2004).

The drawback of the contact time models is that the unknown solution of the film drainage problem is replaced by an unknown parameter ϕ_m , the angle of attachment (similar to the modelling of the encounter by an effective collision angle ϕ_C), or the unknown induction time t_I . For a spherical bubble, both parameters are equivalent; for more general shapes the induction time is typically used. The unknown parameters potentially also contain all the bubble and particle properties (contact angle) and must be determined for each set of parameters (bubble size and shape, particle properties) separately, either by experiment or by the use of other models or empirical correlations. Contact time theories are therefore not closed. However, effective induction times are often determined for a particular experiment from the measured attachment rates, and are subsequently used for other cases.

Nguyen & Schulze (2004) also describe *collision contact time* theories. Contrary to the *sliding contact time* theory presented above, these models are used for the impact of a high-inertia particle on the front of the bubble's surface, which typically attend strong local deformations of the surface. The sliding contact time models are more appropriate for gentle collisions with weak-inertia particles.

Models solving a film drainage equation

Schulze (1992) presents a model that is based on a system of two coupled linear differential equations, the equation of motion for the polar angle ϕ of the particle and the thin-film equation with the film thickness h_F as the parameter. He assumes that particles follow trajectories $(r(t), \phi(t))$ with $r(t) = h_F(t) + R_B + R_P$ along the bubble surface and that the

thin film ruptures when the film thickness reaches a critical value $h_F = h_{\text{crit}}$. This critical thickness $h_{\text{crit}}(\theta_P, \sigma)$ is modelled as a function of the contact angle θ_P and the surface tension σ , and is therefore limited to cases for which such a relation is known.

From the force balance in tangential and normal direction, Schulze (1992) obtains the system of equations

$$\frac{dh_F}{dt} = -h_F c_B \left(\frac{\tau_P(\beta - 1)}{R_P} \overbrace{\left(g \cos \phi - \frac{v_{P,\phi}^2}{R_B + R_P + h_F} \right)}^{\text{gravity + centrifugal acceleration}} + \underbrace{\frac{|u_r| - 0.1714 v_{P,\text{rel}} \sqrt{\text{Re}_B}}{R_P}}_{\text{drag and lift}} \right) \quad (5.12)$$

and

$$\frac{d\phi}{dt} = \frac{\overbrace{u_\phi}^{\text{angular velocity}} + \frac{15}{8} \frac{\tau_P g \sin \phi}{\log(h_F/R_P)}}{R_B + R_P + h_F} \quad (5.13)$$

The force balance includes Stokes drag, the (Saffman) lift force, centrifugal force (particle inertia) and gravity. The resistance to a change of the thickness h_F of the thin film is modelled with the Taylor equation (coalescence of two solid spheres)

$$F = -\frac{6\pi\mu a^2}{h_F} \frac{dh_F}{dt}, \quad (5.14)$$

with the reduced radius $a = R_P R_B / (R_P + R_B)$, that is further simplified by assuming $R_P \ll R_B$.

Thereby the model of Schulze (1992) is an example of a model that consist of solving a simple PDE for the draining film next to the equation of motion of the particle. This concept is considered to be the “modern” approach to the problem of flotation, as it avoids any assumptions about contact and attachment angles or induction times³ and the model can

³The only remaining unknown parameter is the critical film thickness at which the rupture occurs

be easily implemented and solved numerically. It has been successfully extended by using more complex thin-film equations and possibilities for the particle rebound, see Ralston *et al.* (2002) for a review.

Both the contact time models and the more modern theory based on a simulation of the drainage process are widely used in industry and in flotation research. Nevertheless, their use is limited for predicting the outcome of the performed experiments. The contact time models require the knowledge of the induction time t_I , which can itself only be obtained from attachment rate or bulk flotation rate measurements with similar particles and bubbles. Furthermore, even the sliding time t_S is not always well-defined for strongly deforming bubbles (wobbling-ellipsoidal). The models based on the coupled system of an equation of motion for the particle and an equation for the thin liquid film can only be solved numerically.

5.1.3 Particle Detachment

As the forces holding a particle to the gas-liquid interface are finite, particle detachment is possible and occurs⁴. In the past many efforts were made to describe this phenomenon by models based on the balance of the forces of the three-phase contact line adhering to the particle and shear and drag forces of the flow trying to resuspend it. Alternatively, thermodynamic models based on an analysis of the free energy of the particle in the attached and detached state have been proposed. An extensive summary of these models can be found in Nguyen & Schulze (2004).

Another type of detachment models has been evolved from the study of particle resuspension from solid walls by a turbulent flow. These are kinetic/statistical models based on both the force-balance and/or the energy accumulation idea, see Ziskind *et al.* (1995); Reeks & Hall (2001) for reviews. A somewhat special model was proposed by Reeks *et al.* (1988): The adhesive particle can oscillate in the attractive potential near the wall, and the energy transfer is done by fluctuations in the lift force exerted by the turbulent flow that are close to the resonance frequency of the particle, leading to an easier detachment than in the

⁴Although the experiments were designed to avoid particle detachment, Fig. 5.12 shows clusters of particles and small bubbles that detached from the cusp-like rims of a Taylor bubble, whereas this was not observed for other bubble types

case of a steadily applied force. This “Rock’n’Roll” model (it is often called “Rock’n’Roll” model in the literature, as it also incorporates the influence of drag forces resulting in rolling particles; the latter is not relevant for particle detachment from a gas-liquid interface, as the particle can slide and rotate freely in case of an empty interface, only limited by the stick-slip motion of the three-phase contact line on the particle surface itself), which is apparently unreferenced in the flotation literature so far, is intriguing because it can incorporate the random forcing of a turbulent flow together with a clean microscopic description of the attachment forces in form of an attractive potential near the gas-liquid interface.

The essence of the “Rock’n’Roll” model is an exponential probability distribution for the detachment rate p

$$p = n \exp\left(-\frac{Q}{2\langle PE \rangle}\right), \quad (5.15)$$

with a “typical frequency of particle-surface deformations within the adhesive potential well” (Reeks & Hall, 2001). Q represents the height of the potential wall that needs to be overcome; in the flotation case it therefore depends on the increase in the free energy from the attached to the detached state. The quantity $\langle PE \rangle$ is the averaged potential energy of a particle “rocking” in the potential well near the interface. In the original model, it is a linear function of the variance of the fluctuating component $(1 + \eta)\langle F' \rangle^2$ of the time-dependent total force $F(t) = 1/2F_L + R_P/aF_D$, the sum of the lift and drag force, with the radius of the contact area a . The quantity η in the pre-factor $(1 + \eta)$ is the ratio of the near-resonance part of $\langle PE \rangle$ to the off-resonance part, it describes the overlap of the attenuation spectrum with the eigenspectrum of the particle attached to the interface. To summarise, this model contains all necessary quantities to describe the particle detachment in a turbulent flow, namely

- the binding energy in form of the height of the potential well Q ;
- the kinetic energy of the oscillations of the particle in the potential well $\langle F' \rangle^2$; and
- the coupling strength η due to the overlap of the oscillation spectrum with the spectrum of the attenuating forces.

Particle detachment cannot be quantitatively measured in the performed experiment, but it can be observed in some cases, see Sec. 5.2.4. The idea of a resonant energy transfer is however very intriguing for future research on the influence of turbulence on the thin-film drainage process. Dynamical systems like the film drainage models by Schulze (1992) described in Sec. 5.1.2 typically have a spectrum of eigenmodes including instable modes. It is obvious that an attenuation of an instable mode by resonant coupling can lead to a much faster rupture of the thin liquid film than what is found by quasi-steady simulations.

5.1.4 Modelling the time-development of the Surface Coverage of a Bubble

In the case of a semi-spherical bubble, there are two possibilities for an increase in the number of particles attached to the bubble surface:

1. particles attach on the front side of the bubble after a certain sliding time; and
2. particle attachment occurs at random positions and is dominated by turbulent particle transport towards the gas-liquid interface.

The first case can be modelled using the various contact time theories (see Sec. 5.1.2). The aim of the present section is to investigate the second idea.

The hypothesis is to assume that the particle attachment rate is proportional to some attachment flux j_P and the total area $A(t)$ that is uncovered and thereby available for attachments

$$\frac{dN(t)}{dt} = j_{\text{att}} A(t). \quad (5.16)$$

The attachment flux j_{att} has the dimension of particles per unit time and area, and is assumed to be a linear function of the particle concentration in the surrounding flow⁵ and also depends (non-linearly) on the flow itself (it incorporates all the attachment efficiencies and the turbulent transport towards the interface). It is also chosen to be independent of time and viscosity, although this simplifying assumption

⁵This assumption is valid for low particle concentrations where particle-particle interactions are negligible

is not necessarily fulfilled due to the change in boundary conditions from a free-slip gas-liquid interface to a (partial) no-slip interface with increasing coverage. It is nevertheless a reasonable assumption for a bubble size in the inertial range of the turbulence (Pécselel *et al.*, 2012) and particles larger than the thickness of a possible boundary layer.

Assuming furthermore that each attached particle covers a certain area A_P of the bubble surface, the equation changes into

$$\frac{dN(t)}{dt} = j_{\text{att}} (A_0 - A_P N(t)) = j_{\text{att}} A_0 \left(1 - \frac{A_P}{A_0} N(t) \right). \quad (5.17)$$

The solution is given by

$$N(t) = \frac{A_0}{A_P} \left(1 - \exp \left(-A_P j_{\text{att}} t - C_0 \frac{A_P}{A_0} \right) \right). \quad (5.18)$$

The integration constant represents the choice of a reference/starting time $C_0 = j_{\text{att}} A_0 t_0$ and can be chosen equal to zero. The model for the covered surface area can therefore be written as

$$A_{\text{covered}}(t) = A_P N(t) = A_0 (1 - \exp(-t/T_{\text{att}})) \quad (5.19)$$

with the time scale $T_{\text{att}} = \frac{1}{A_P j_{\text{att}}}$ for the coverage reaching 1-1/e of its final value A_0 . This time scale T_{att} was measured in the performed experiments, see Sec. 5.2.2.

It should be noted that this approach to the attachment problem is completely different from the contact time theories and the simulations based on solving thin-film equations. It assumes that the whole flotation process is controlled by the “random bombardment” of the interface by a turbulent particle flux and therefore by the mechanisms of turbulent particle encounter described in Eq. (5.6). It shows a good agreement with the experimental data presented in Sections 5.2.4 and 5.2.5. Nonetheless, the complete complexity of the attachment process is incorporated in the attachment flux j_{att} .

5.2 Measurements of Particle Attachment Rates

The aim of the experiment is to measure the rate of flotation of particles on a single bubble only. The advantage of this approach is that the flow

5 Surface Attachment

Table 5.1: Parameters for the particle attachment measurements

Particle type		fluorescent Polyethylene (PE)
Dye		Rhodamine B
Particle size	d_P	27-45 μm 53-63 μm 75-90 μm 106-125 μm
Density	$\rho_{\text{H}_2\text{O}}$	$1000 \frac{\text{kg}}{\text{m}^3}$ at 20°C
Viscosity	$\mu_{\text{H}_2\text{O}}$	$10^{-3} \frac{\text{kg}}{\text{m}\cdot\text{s}}$ at 20°C
Surface tension	$\sigma_{\text{H}_2\text{O}-\text{Air}}$	$7.310^{-2} \frac{\text{kg}}{\text{s}^2}$ at 20°C
Morton number	Mo	$2.5 \cdot 10^{-11}$
Semi-spherical bubbles	v_{rise} V Re Eo	15...16cm/s $\approx 5\text{cm}^3$ 3400 60
Wobbling- ellipsoidal bubbles	v_{rise} V Re Eo	14...16cm/s $1 \dots 2\text{cm}^3$ 2000 20...30
Small spherical & ellipsoidal bubbles	v_{rise} V Re Eo	$\leq 11\text{cm/s}$ $\leq 0.1\text{cm}^3$ ≤ 600 ≤ 5
Taylor bubbles	v_{rise} V	14cm/s $\geq 15\text{cm}^3$

around this bubble can be studied and the build-up of particle coverage of the bubble's surface can be measured over time. The disadvantages are that a single rising bubble is rather uncommon for industrial applications. More commonly, plumes of thousands of bubbles are used, with bubble collisions, coalescence and break-up in a highly complex flow. A single bubble experiment avoids complex bubble-bubble interactions, and the approaching flow is well-defined. In flows with a small volume load $< 10^{-3}$ (Elghobashi, 1994), objects like particles or bubbles are typically not influenced by other objects, and single-bubble experiments are a valid simplification. To increase the observation time, the bubble is trapped in a conical pipe at a position where the rising velocity is cancelled by the velocity of the approaching flow. As a consequence, the pipe walls have a certain influence on the bubble shape when the bubble volume becomes too large (see Sec. 5.2.4 for a discussion of observed bubble shapes). For further simplification, the only fluids used were water for the liquid and air for the gaseous phase, resulting in the dimensionless numbers presented in Tab. 5.2.

Most experiments were performed using a semi-spherical bubble (effectively a spherical-cap bubble, but due to the wall effects the polar angle is close to 90° instead of the $\approx 50^\circ$ typically observed for freely rising bubbles of that volume (Wegener & Parlange, 1973). These bubbles have a stable toroidal wake, therefore oscillations are minimal and sudden variations in the bubble position are largely avoided.

Although the experimental facility is not limited to this type of particles, only fluorescent Polyethylene particles of different sizes were used for the measurements, see Tab. 5.1. Polyethylene particles are weakly hydrophobic (contact angle 96°), and are therefore good candidates for this type of experiments as attachments are sufficiently likely (large critical thickness for the rupture of the thin liquid film) and the detachments are unlikely (the energetically preferred state is the attached state) if sharp rims, skirts and cusps of the bubble are avoided. The fluorescence of the particles was initially required for the observation with a high-speed camera under exposure with the 532nm light of a Nd:YAG laser, as in this case the strong reflections from the surface can be avoided by means of an optical low-pass filter, similar to the one used for the two-phase flow measurements in Chapters 3 and 4

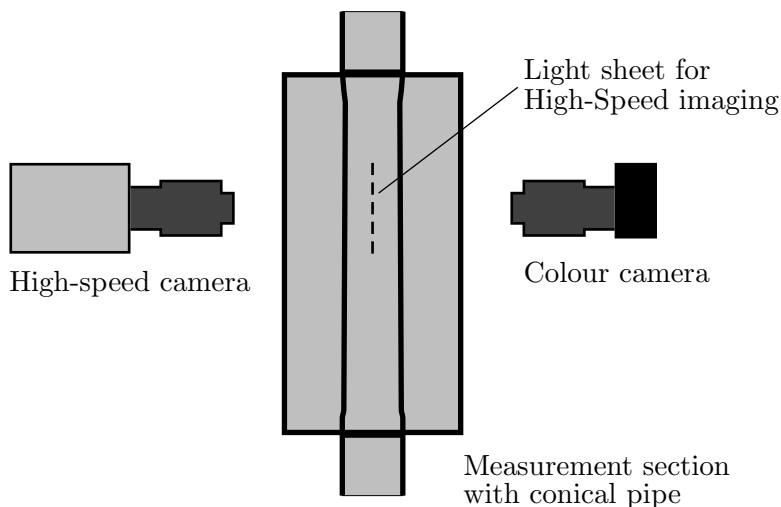


Figure 5.1: Imaging setup for taking High-speed and colour records; the light sheet for the high-speed PIV is aligned perpendicular to the sketched plane

5.2.1 The DABuT Facility

Measurements on gas bubbles in water require either a mechanism that follows the trajectory of a rising bubble over time, or some method to keep a bubble in a certain volume of observation. The DABuT (Dynamic Air Bubble Trap) facility is based on the latter principle; the bubble is kept stationary in a conical pipe by adjusting the flow rate such that the rise velocity of the bubble is countered by the flow velocity. The facility consists of a rectangular test section that contains the conical pipe from a Rotameter volume flow meter, which furthermore allows an almost distortion free optical access to the central pipe from all four sides. The flow enters the test section via a turbulence settling chamber consisting of a 20 cm long flow straightener to remove any swirl resulting from the inlet, as well as two additional grids to further suppress large scale turbulence. The outlet of the test section is connected to a wye junction with the straight end connected to the bubble injector, the out-bound end leading to the pump. The flow loop is completed by the pump and a flow meter. The bubble injector consists of a turnable



(a) High-Speed camera (left) and the conical pipe of the (b) Bubble injector with measurement section (right); the mirror in the front is the needle and the turnable spoon ($V=2\text{cm}^3$)

Figure 5.2: Test section and bubble injector of the DABuT setup

spoon mounted on top of an injection nozzle, see Fig. 5.2.

The imaging system contains of a high-speed camera for particle tracking and a conventional digital SLR camera for the colour imaging. The latter camera is triggering two flashlights, one connected to the hot-shoe of the camera itself, and the second one in slave mode by a photo diode that triggers on the light of the first flash. At the magnifications ($M \approx 0.4$) used, an aperture of F/22 was used to achieve a compromise between depth of field and a reasonably sharp imaging of the bubble. The high-speed camera was used with an aperture of F/8 to F/16 for a sufficient exposure at different frame rates and laser pulse energies. The power of the used flashlights was set to low values of 1/16 of the maximum power output to obtain a sufficiently short pulse duration (10^{-4} seconds) for avoiding motion blur of the moving particles.

5.2.2 Measurement Principle

The working principle of the flotation measurements with trapped bubbles is explained in the following. By the conservation of the particle number, the attachment flux of particles towards the bubble surface

5 Surface Attachment

Table 5.2: Selected parameters of the measurements in the DABuT facility

Test section		$14.5 \times 14.5 \times 39.5$ cm
	Tube \varnothing	34–40mm, conical
	Tube length	300mm, 260mm conical
Imaging systems	Cameras	Photron Fastcam APX RS with Micro-Nikkor 105mm 2.8D Pentax K10D with Tamron 90mm 2.8

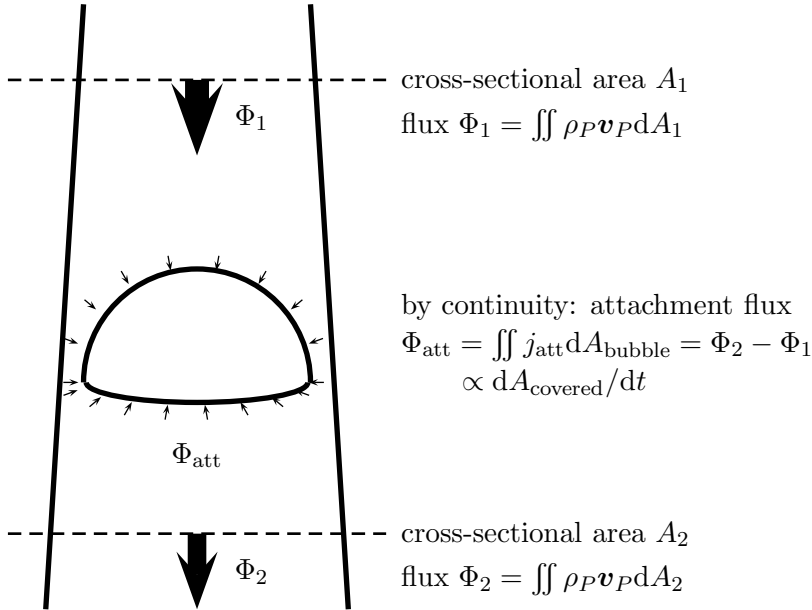


Figure 5.3: Measurement principle: the attachment rates cannot be measured directly, but under identical experimental conditions, they can be compared for different bubbles by determining the rate in the build-up of surface coverage

must be the difference between the particle flux over cross-sectional areas upstream and downstream of the bubble, hence

$$\Phi_{\text{att}} = \iint j_{\text{att}} dA_{\text{bubble}} = \Phi_2 - \Phi_1, \quad (5.20)$$

if the particle concentration in the fluid does not change (steady state assumption). As shown in Sec. 5.1.4, the magnitude of the total attachment flux is related to the change of the number of attached particles over time. The number of attached particles is proportional the covered surface area, as particles can only attach in form of a mono layer; see Sec. 5.2.5. Putting everything together, the attachment flux is proportional to the change of the covered area

$$\Phi_{\text{att}} \propto \frac{dA_{\text{covered}}}{dt}. \quad (5.21)$$

The measurement of the covered area therefore only represents a relative measurement of the attachment flux Φ_{att} , up to a multiplicative constant. In reality, however, even for very stable bubbles (see Sec. 5.2.4) this cannot be achieved, and the wobbling introduces a bias to the measurements that is discussed in Sec. 5.2.3. Nonetheless, the measurement of the covered area, independently of the normalisation, over time allows to access the timescale of the flotation problem, as the timescale of the attachment model (Sec. 5.1.4) is independent of the total absolute or relative coverage. The remaining systematic uncertainties are mainly due to the wobbling of the bubble and its consequences for the projection on the sensor of the camera.

5.2.3 Methods for Image Analysis

The recorded images of the bubble are analysed to obtain information about the number of attached particles (bubble coverage) over time. Furthermore, the concentration of particles in the free flow must be determined to eliminate this parameter from the rate of flotation. This way, the effect of the shape of the bubble and the properties of the flow around it can be studied.

Owing to the simplicity of the design of the experiments, there are two issues that must be dealt with: Firstly, the usage of a standard digital single lens reflex camera (SLR) for recording colour images of the gas

bubble, which requires the minimisation of any influence of the white balance setting and the internal processing on the final result. Secondly, a full reconstruction of the 3D bubble surface is not possible with a single camera only, therefore the instability in the bubble's position causes different projected bubble shapes and an unknown bias to the measured coverage of the bubble.

Bubble coverage

Although the counting of individual particles that are attached to the bubble is in principle possible, there are practical difficulties with that approach due to a low contrast at particle boundaries in a covered zone and in particular for smaller particles due to the general diffraction-limited imaging (an aperture of F/22 was used to maximise depth-of-field, which also causes a reduction of small-scale contrast as a result of an increased diffraction-limited spot size in comparison to imaging with a lower F-number). The presence of a mono layer of particles (see Sec. 5.2.5) however simplifies the particle counting, as it is simpler to detect the total covered area, rather than counting individual particle images.

The algorithm consists of the following steps:

1. Proper Orthogonal Decomposition (POD) of the colour space to find the colour (RGB) eigenvector that corresponds to the 'pink' particle images;
2. calculating the pink component (saturation) and its histogram;
3. fitting a bimodal distribution function to the histogram; and
4. determining the integral under the Gaussian part.

The POD is done by calculating the eigenvalues and -vectors for the covariance matrix

$$COV = \begin{pmatrix} \langle \mathbf{r}, \mathbf{r} \rangle & \langle \mathbf{r}, \mathbf{g} \rangle & \langle \mathbf{r}, \mathbf{b} \rangle \\ \langle \mathbf{g}, \mathbf{r} \rangle & \langle \mathbf{g}, \mathbf{g} \rangle & \langle \mathbf{g}, \mathbf{b} \rangle \\ \langle \mathbf{b}, \mathbf{r} \rangle & \langle \mathbf{b}, \mathbf{g} \rangle & \langle \mathbf{b}, \mathbf{b} \rangle \end{pmatrix}, \quad (5.22)$$

with $\mathbf{r} = \mathbf{R} - \text{mean}(R, G, B)$ being the vector of the red colour channel of the image corrected by the grey value (mean of all three components),

and equivalently for the green (g) and blue (b) colour channels. The individual off-diagonal components of Eq. (5.22) therefore represent the cross-covariance of two different colour channels, and the whole 3×3 matrix is the colour covariance matrix of the image. The eigenvector of such a covariance matrix are the so-called *principal components* (the POD is also often called Principal Component Analysis); they describe the directions in RGB space in which the data varies with the corresponding eigenvalue as variance. The eigenvectors therefore each correspond to a base vector of the colour space, and they all span the ellipsoid which gives the best approximation to the point cloud of the image in the colour space in a least-square sense. The eigenvalues are usually interpreted as the energy content of the image belonging to the associated mode or eigenvector. Subtracting the mean grey before the POD gives effectively a decomposition of a 2D subspace of the whole colour space. In the present case of having pink particle images, we find pink eigenvector and one vector orthogonal to pink. The magnitude of the corresponding eigenvalue to pink changes in time with increasing coverage; the eigenvalue itself is yet an insufficient measure for the coverage.

The advantage of this approach is that any bias introduced by colour mapping functions in the image processing in the camera as well as the influence of white balance settings can in principle be eliminated. For unchanged camera settings and exposure, the found eigenvectors should be constant over the measurement time of one data set. As shown in Fig. 5.4, this is indeed the case after a sufficient time. For small times, the number of particles that have attached to the bubble are small and hence the number of pixels that are pink, leading to higher uncertainties in the vector components. To avoid these uncertainties and their influence on the analysis of the saturation histograms, the whole data set was analysed with a constant colour vector that was chosen identical to the converged values.

From the pink eigenvector, the pink signal is determined by taking the scalar product with the colour vector at every pixel. The subsequently calculated histogram is shown in Fig. 5.5. It shows the bimodal distribution with a nearly Gaussian part for the pixels that can be associated with particles covering the bubble surface. The main part (background) is similar to a Laplace distribution (double exponential distribution), although a better fit to the histogram is obtained for posi-

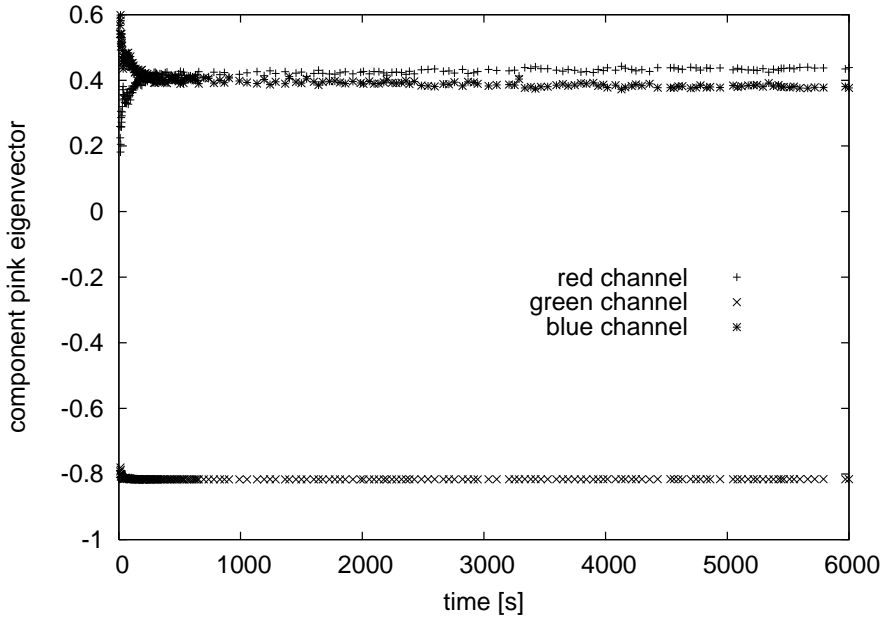


Figure 5.4: Stability of the POD colour space decomposition for a selected data set; coefficients of the eigenvectors over time (left) and eigenvalues over time (right)

tive pinkness values by using a Cauchy distribution in combination with the Gaussian distribution. The time development of the histogram (the Gaussian part changes in expectation value and magnitude, see Fig. 5.5) also shows that detection strategies based on binarisation are not suitable for the problem. Any near-optimal threshold for the whole data set would underpredict the coverage for low values (at the beginning of the experiment) and overpredict it later on. Therefore, only the Otsu method was tested more extensively (automatic thresholding based on the maximisation of the inter-class variance in the histogram, see the section on “clustering thresholding” in Sezgin & Sankur (2004)), but was found to fail if one class (the covered part) is very small.

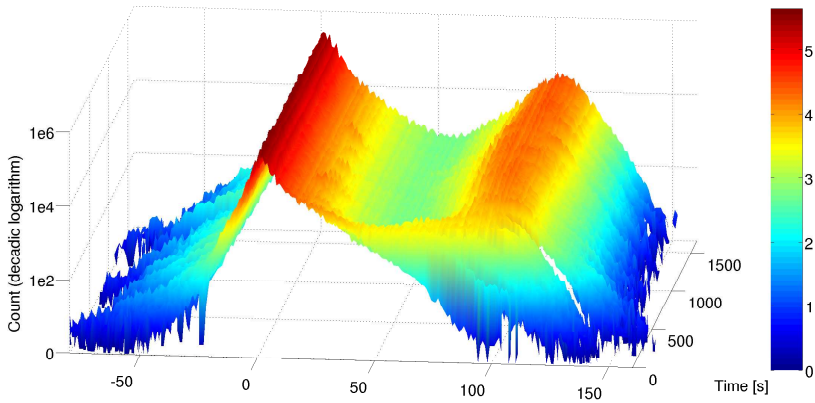


Figure 5.5: Bimodal distribution of the pink signal (saturation) and its time development

Particle concentration in the flow

Determining the amount of particles dispersed in the flow is necessary to allow a normalised comparison of the determined time scales. As the particle concentration changes in an uncontrollable way due to settling, particles sticking to walls, and due to collisions with the bubble, the amount of injected particles is not a reliable quantity. The average concentration of particles was therefore determined by image processing as well.

A convenient method to count particle images is to detect local maxima in the image colour field (the pink colour component calculated by the POD). To avoid counting maxima that are related to the image noise, the image is blurred with a binomial filter of given standard deviation, which is an often used and computationally efficient discrete approximation to a Gaussian smoothing filter (Haddad & Akansu, 1991). This approach (scale-space decomposition, see e.g. Lindeberg (1993)) is a very common method in image processing to extract features like points and edges from noisy images. In the case of the recorded data sets, a complete scale-space decomposition is not needed and too time

5 Surface Attachment

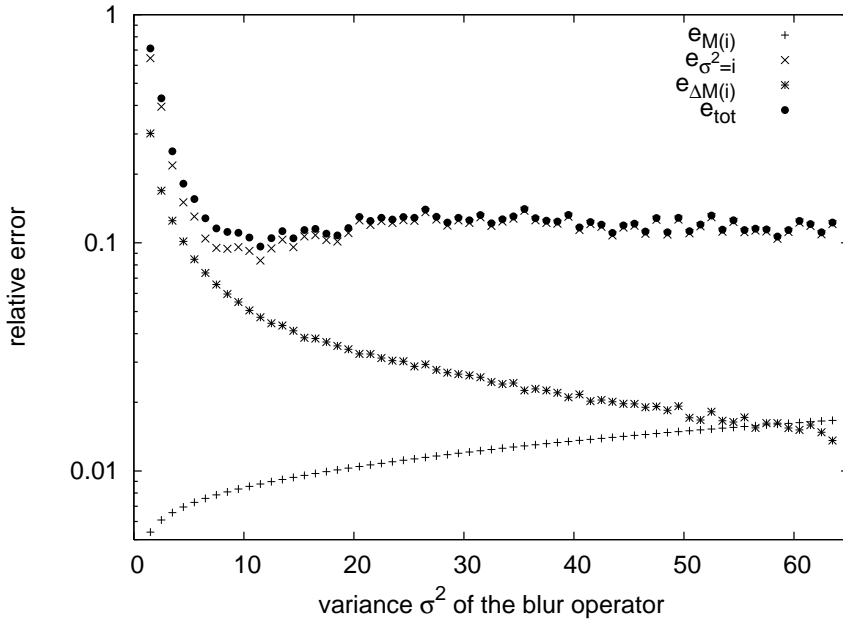


Figure 5.6: Uncertainties in the particle counting (concentration measurements) as a function of the variance of the blur operator

consuming, as all particle images are of a similar size⁶. It is therefore sufficient to choose an optimal second centred moment (denoted as “variance” in the following) of the size of the blur operator, see Fig. 5.6.

The optimal choice of the variance of the blur operator is a compromise between the relative error in the counting of $M(i)$ maxima

$$e_{M(i)} \cong \frac{\sqrt{M(i)}}{M(i)} = \frac{1}{\sqrt{M(i)}}. \quad (5.23)$$

This error is typically smaller than the systematic error induced by choosing a too small or too large variance, which can be estimated by

$$e_{\Delta M(i)} \cong \frac{\partial M(i)}{\partial i}, \quad (5.24)$$

⁶For the performed experiments, this is not a result of the diffraction-limited imaging (the particle size is about twice to four times as large as the diffraction spot size), but a consequence of all images being recorded at almost identical magnification

and the error induced by filtering potentially relevant information in the image. The latter is more difficult to access, but it can be estimated by the correlation in the detection rates after applying filters with similar standard deviation. Near the optimum filter width, the result of the maxima detection should not depend on the filter width itself, and the correlation between the detection rates should be close to unity. When the variance of the filter is varied in discrete steps, the error of the filter with variance i can be estimated by

$$e_{\sigma^2=i}^2 = 1 - \frac{\text{corr}(d_{i-1}, d_i) + \text{corr}(d_i, d_{i+1})}{2}. \quad (5.25)$$

When all errors are assumed to be statistically independent, the error norm

$$e_{tot,i} = \sqrt{e_{M(i)}^2 + e_{\Delta M(i)}^2 + e_{\sigma^2=i}^2} \quad (5.26)$$

can be minimised to obtain an optimal choice for the variance $\sigma^2 = i$.

Fig. 5.6 shows that for a sufficiently large blur size, the error is dominated by $e_{\Delta M(i)}$ only and reaches a plateau of nearly constant total error. Based on that, a blur filter with a standard deviation of 4 pixels ($\sigma^2 = 16$) was chosen for all data sets. This results in a total relative uncertainty of about 10% for a single concentration measurement.

Fig. 5.7 shows a result of the maxima counting, plotted is the number of detected maxima per square millimetre of the projected area over time. The approximate 4% drop in concentration for short times corresponds to the amount of particles collected by the bubble. The further slow decrease in concentration is approximately the rate of particle settling in the whole facility⁷. If the concentration values obtained from Fig. 5.7 are used to calculate the total amount of particles in the facility, the obtained value is only about one quarter to one third of the amount of particles that were added to the setup beforehand. This shows that particles quickly settle and attach to surfaces of the setup, a process that cannot be avoided as evidenced by the negative slope of the particle concentration for larger times. The typical volume load

⁷Ideally, this should have been confirmed by a separate measurement of the decay of particle concentration only (without a bubble); however, in the first place, the colour images were taken for documentation purposes only, and it was found later that they contain more valuable information compared to the images taken with the high-speed camera and a light sheet

5 Surface Attachment

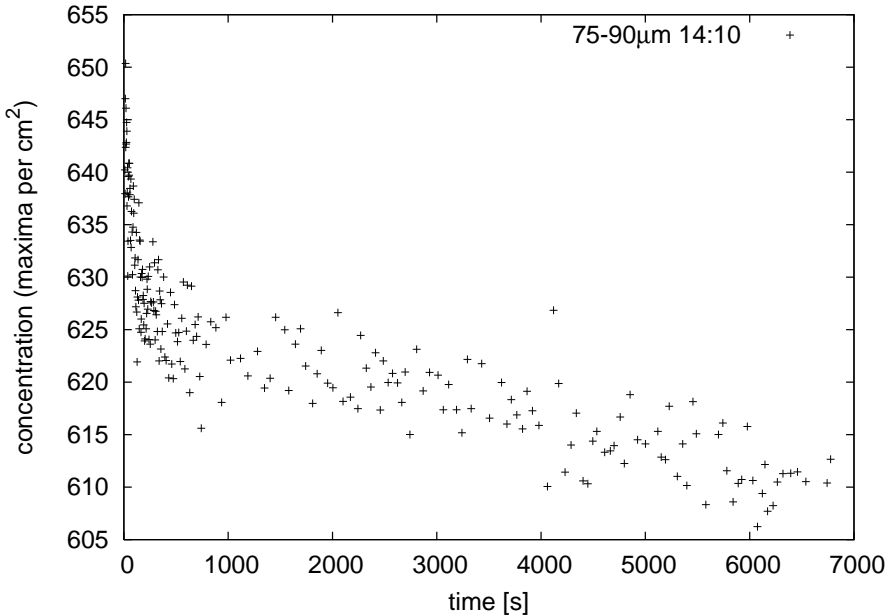


Figure 5.7: Time-development of the particle concentration (counted maxima) in the flow (75...90 μm particles). Note the sharp decrease at the beginning of the experiment (high attachment rate due to the presence of a yet uncovered bubble), compared to the slow decrease when the bubble's surface is covered (particle settling in the facility)

for all performed experiments was in the order of 10^{-4} (1...5cm³ of particles over a total fluid volume of about 20 litres).

5.2.4 Qualitative results

The following part gives a brief descriptions of the bubbles used for measurements in the DABuT facility. The discussed regimes for the bubble shape are not sharp, and transitions of one type to another typically occur when the surface tension changes due to a mono layer of attached particles (see Sec. 5.2.5), due to a change in boundary-condition at the bubble surface with an increasing number of attached particles, and when the volume is reduced over time due to dissolving

air. The bubble shapes described in the following have been found in many experiments already, see e.g. Clift *et al.* (2005) for a summary.

Semi-spherical bubbles

The bubbles of this type are an intermediate regime between the wobbling-ellipsoidal/wobbling spherical-cap bubbles and the large Taylor bubbles typically found in slug flows. They have a volume of about 5 cm^3 , and contrary to wobbling-ellipsoidal bubbles the wall effects have a noticeable influence on the shape. The shape of a freely rising bubble with a similar volume in water would have the shape of a spherical cap. The semi-spherical bubbles inherit from them the stable flow pattern around the bubble and the rather sharp (small radius of curvature) rim at the point of flow separation. The presence of the pipe walls results in a semi-spherical shape as a significant portion of the pipe's cross-sectional area is occupied by the bubble ($>50\%$ blockage). The shape of this type of bubbles is rather stable due to the stable flow pattern around it, and is only disturbed by surface modes that get damped and finally vanish as soon as a sufficient number of particles become attached to the bubble surface. In the latter case the shape also changes slightly; the rim becomes less sharp and the point of flow separation moves a bit upstream. Bubbles with a somewhat smaller volume can also change their shape towards a wobbling ellipsoidal bubble by the attachment of particles and by a volume loss due to air dissolving into the water. A detachment of smaller bubbles from the rim as occurs for larger Taylor bubbles was not observed.

Wobbling-ellipsoidal bubbles

These air bubbles have a volume of about $1\text{-}2 \text{ cm}^3$, and their shape is typically not stable. This regime includes also wobbling spherical-cap bubbles ($\approx 2 \text{ cm}^3$), as these typically turn into a wobbling ellipsoidal bubble when a sufficient large number of particles stick to the surface. In general, the effects of the pipe wall are still weaker than the surface forces, and although the wobbling spherical caps show first signs of a rim, the surface is generally smooth. The flow around these bubbles is on the border between a largely stable (wobbling spherical cap) and unstable (wobbling ellipsoidal) flow pattern. The presence of the pipe

5 Surface Attachment

walls is likely the cause for the stabilisation. A good discussion of the path instability of ellipsoidal bubbles can be found in Magnaudet & Eames (2000).

Small ellipsoidal and spherical bubbles

The shape of the bubbles in this regime is fully determined by surface forces, with the deviation from the spherical shape due to gravitational effects and no observed wobbling. These bubbles are either (i) created by detachment from a sharp rim at the point of flow separation or (ii) by single bubbles that detach individually from the injection capillary and that do not coalesce on their path towards the test section. Bubbles with a diameter of about 1 mm and less are of the first kind, because the detachment from the injection capillary provides a lower limit for the bubble size. When multiple bubbles of this type are injected, they typically coalesce within a few seconds and create a larger bubble of the wobbling ellipsoidal type. With the presence of small polyethylene particles (with a diameter of 27-45 μm) in the flow, the rapid attachment of these particles prevents coalescence and measurements can be done on small groups of these bubbles. The wake behind these bubbles is already turbulent such that these bubbles oscillate, and in general they follow chaotic paths. Smaller, spherical bubbles almost never leave the boundary layer near the pipe walls; the situation changes a bit with larger bubble sizes and in the presence of other bubbles.

Taylor bubbles

If one injects bubbles with a volume significantly larger than that of a semi-spherical bubble, the semi-spherical front of the bubble will not change, and the increase in volume results in an extension of the bubble size downstream (Delfos, 1996). Although the extension is almost cylinder-like, the distance of the surface to the pipe wall is gradually decreasing. The somewhat unstable bottom of the Taylor-bubble is separated from the side walls by a sharp rim. The Taylor bubble loses volume over time by the separation of small ($<1\text{mm}$) bubbles from this rim, which are typically found in the wake of the Taylor bubble.

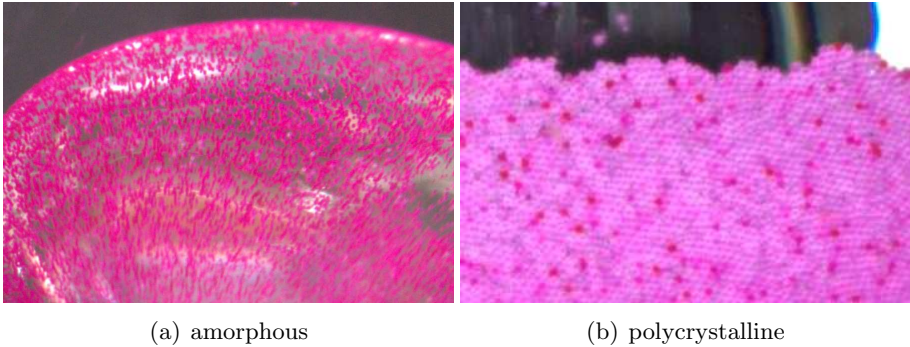


Figure 5.8: Observed monolayers on bubble surfaces

5.2.5 Observations

Monolayers of Particles

The recorded images with a sufficient number of attached particles show that the particles form a mono layer, with an increasingly dense packing that locally approaches a two-dimensional dense packing for bubbles with a fully covered bottom (see Fig. 5.8). The only exception are clusters of smaller particles that are present in the flow (the turbulence in the setup is not strong enough to break up these clusters) and which also attach as clusters. This mono layer has the effect that it changes the boundary condition on the bubble surface from free-slip to no-slip. There is also an effect on the effective surface tension of the particle-filled interface: Contrary to the reduction of surface tension by surfactants (Probstein, 2003), a layer of attached particles increases the stiffness and thereby the surface tension.

The two types of monolayers shown in Fig. 5.8 are to some degree related to the flow around the bubble: high tangential velocities cause stronger shear forces, causing particles to create a more dense packing with short-range order (“polycrystalline”) at the rear side of the bubble. If these shear forces are lower (lower rise velocity of the bubble), then particles tend to cover the surface with a higher inter-particle distance with no apparent order (“amorphous”). Local repulsive forces between the particles inhibit the formation of a more dense packing.

According to Landau & Lifshitz (1987), an adsorbed film can change

5 Surface Attachment

surface tension because it provides an additional resistance to the increase or decrease of local surface area. This is the case if the (effective) viscosity of the film is large compared to that of the two fluids (here: air and water). The boundary condition to fulfil at the interface is⁸:

$$\left[p_1 - p_2 - \sigma \left(\frac{1}{R_1} + \frac{1}{R_2} \right) \right] n_i = (\sigma_{ik}^{(1)} - \sigma_{ik}^{(2)}) n_k + \frac{\partial \sigma}{\partial c_A} \frac{\partial c_A}{\partial x_i} \quad (5.27)$$

The left side is equivalent to the Young-Laplace formula, and the first term on the right takes into account the strain rate tensor

$$\sigma_{ik} = -p\delta_{ik} + \mu \left(\frac{\partial u_i}{\partial x_k} + \frac{\partial u_k}{\partial x_i} \right) \quad (5.28)$$

of a moving interface as a result of viscous friction in both media. The second term to the right is the gradient of the (spatially varying) surface tension, with the surface tension $\sigma(c_A)$ being a function of the surface concentration c_A . Additionally, the continuity equation for the film

$$\frac{\partial c_A}{\partial t} + \text{div}(c_A \mathbf{v}) = 0 \quad (5.29)$$

has to be fulfilled in case the film is compressible (the area of small surface elements can change). The latter is to some degree the case, as the film can be tangentially stretched (increasing the inter-particle distance at constant thickness would not invalidate the layer model for small expansions); however, compression is effectively not possible beyond the point when neighbouring particles are in direct contact.

Landau & Lifshitz (1987) also derive a damping factor for capillary waves at a surface that is covered with an adsorbed incompressible film. Neglecting gravity, they obtain

$$\gamma = \frac{k^{7/4} \mu^{1/2} \sigma^{1/4}}{2\sqrt{2} \rho^{3/4}} \quad (5.30)$$

with the wave number k , the dynamic viscosity μ and fluid density ρ , a value which differs from the pure interface by the factor

$$\frac{\gamma_{\text{Film}}}{\gamma} = \frac{1}{4\sqrt{2}} \left(\frac{\sigma \rho}{k \mu^2} \right)^{1/4} = \frac{1}{4} \left(\frac{\text{Re}_\lambda^2}{8\pi \text{We}_\lambda} \right)^{1/4}. \quad (5.31)$$

⁸This model is solely based on macroscopic reasoning (finitely small film thickness); effects like the locally increased curvature are not considered and unlikely to contribute significantly, as the contact angle for PE particles with water and air is close to 90°C

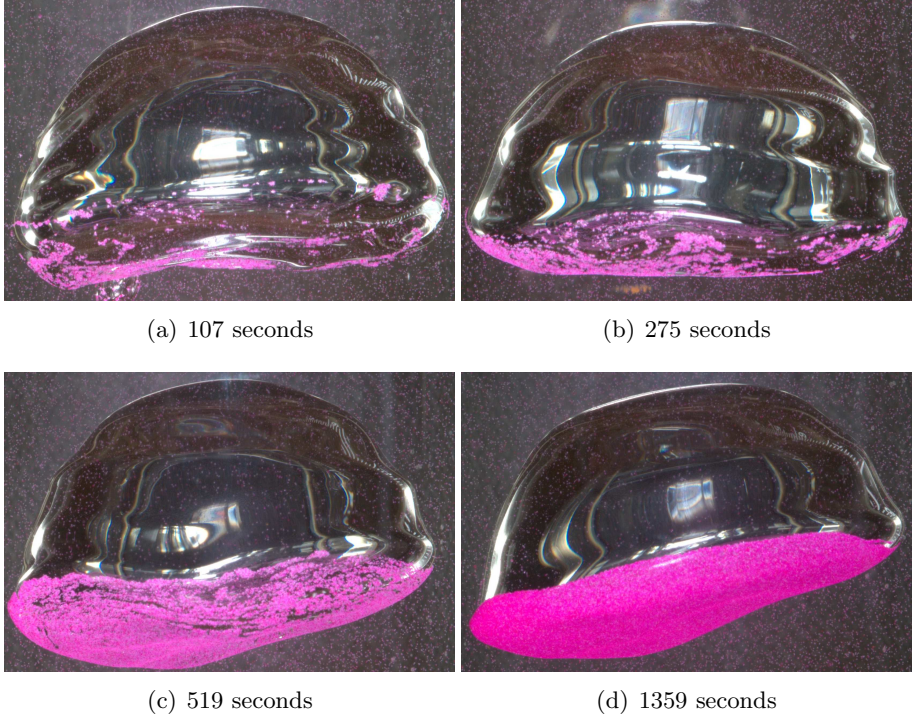


Figure 5.9: Selected records of a time series with a semi-spherical bubble, 4g PE particles of diameter $53\text{-}63\mu\text{m}$

The Weber number $We_\lambda = \rho v^2 \lambda / \sigma$ and the Reynolds number $Re_\lambda = \rho v \lambda / \mu$ are here defined with the wavelength λ of the capillary wave as the characteristic length scale (not to be confused with the turbulent Reynolds number that is defined over the Taylor microscale). For typical k , this factor is large relative to 1, therefore the adsorbed film model explains the strong damping of surface waves that is observed in the presence of a mono layer of particles.

Semi-Spherical Bubbles

Semi-spherical bubbles show a rather unusual build-up of particle concentration. From the start of the experiment on, surface concentration builds up very quickly ($\mathcal{O}(10\text{s}) \dots \mathcal{O}(100\text{s})$) on the rear (wake side) of the bubble. As soon as the rear side is covered such that the bubble is filled

5 Surface Attachment

beyond the rim at the stagnation point, the concentration increases only very slowly in the order of several hours ($\mathcal{O}(10^4\text{s})$). This period is characterised by a completely covered rear side that only breaks up occasionally to leave thin gaps of free air-water interface that closes quickly. At the time scale of $\mathcal{O}(10^4\text{s})$ the volume of the bubble also changes due to air dissolving into the water; therefore it cannot be excluded that the increase in the percentage of covered bubble surface is caused by a volume loss with an approximately constant total number of attached particles. Noticeable is also the dense packing of particles in the covered area, even a quasi-2-dimensional short-range order similar to that in a polycrystalline solid can be observed.

Wobbling-Ellipsoidal Bubbles

The build-up of the surface particle concentration is more slowly in the case of a wobbling ellipsoidal bubble. The time needed to cover more than half of the bubble's surface is $\mathcal{O}(10^3\text{s})$, the attachment rates decrease gradually. Over the same time scale, a volume loss due to dissolving air can be noticed, which only stops when the bubble is completely covered with particles. However, the bubble is never as densely covered as in case of the semi-spherical bubbles, in analogy to a solid state crystal the covering layer could be described as amorphous.

Small Ellipsoidal and Spherical Bubbles

The particle attachment to small ellipsoidal and spherical bubbles is comparable to that of wobbling-ellipsoidal bubbles, with gradually decreasing attachment rates over a time of several minutes, up to a point where no increase is observable any more. On the same time scale a loss of volume due to dissolving air is visible. The surface is never fully covered with particles, as coverage remains loose with greater clear openings. It should be noted that these observations are only based on a single time series of records taken from an injected group of bubbles.

Taylor Bubbles

The concentration increase at the back side of Taylor bubbles is, similar to the semi-spherical bubbles, of order $\mathcal{O}(10^2\text{s})$. They also show a similar slowdown in the attachment rate when the rear side is fully covered.

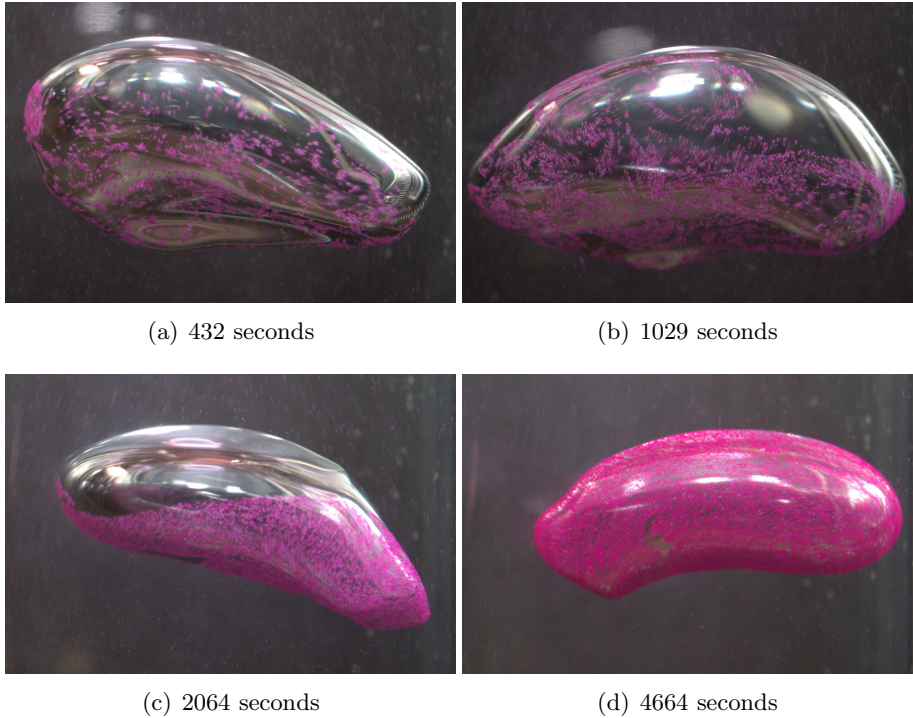


Figure 5.10: Selected records of a time series with a wobbling-ellipsoidal bubble, 2g PE particles of diameter $53\text{-}63\mu\text{m}$

After that moment, the covered area grows slowly ($\mathcal{O}(10^4\text{s})$) beyond the rim and creeps upwards against the flow direction. Estimates of time scales are difficult here, since the bubble constantly loses small air bubbles that are (partially) covered by particles, and which create small clusters of millimetre-sized bubbles and particles (see Fig. 5.12). The covered part of the bubble is densely packed with particles.

Attachment Time-Scales for Semi-Spherical Bubbles

Fig. 5.14 was obtained by plotting the computed values for the coverage of the bubble over time. The covered area is increasing steeply in the beginning, reaches a local maximum for intermediate times and then approaches then a constant value. The data shows a lot of scatter, larger than the estimated uncertainty in the particle counting. The

5 Surface Attachment

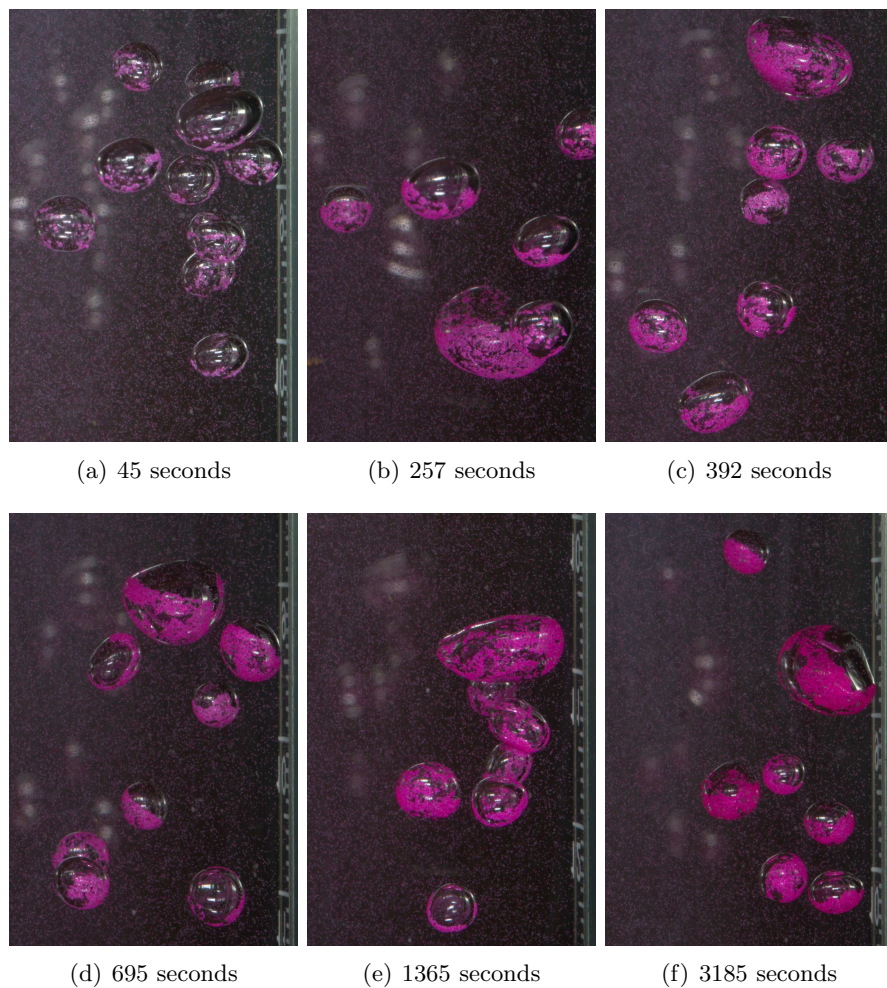


Figure 5.11: Selected records of a time series with a group of small bubbles, 8g PE particles of diameter $53\text{-}63\mu\text{m}$

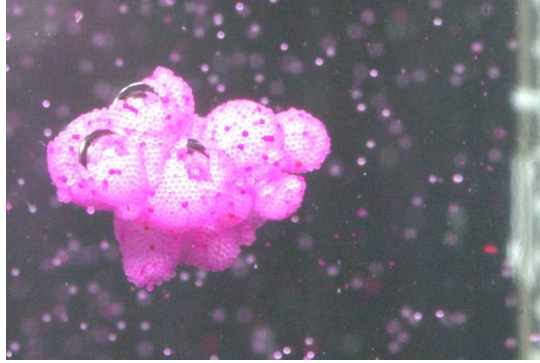


Figure 5.12: Clusters of millimetre-sized bubbles and particles (106-125 μm) in the wake of a Taylor bubble

latter is a direct consequence of the wobbling of the bubble; when the bottom side of the bubble is visible in the field-of-view, higher values are recorded than when the bubble is observed from the side only. The observed local maximum in Fig. 5.18 (top) is likewise a result of the wobbling, which is caused by a bias in the data analysis: the algorithm is too simple to distinguish between particles that are observed directly and those that are seen through the bubble itself (see Fig. 5.15). In both cases, part of the image is positively detected as “pink” and is therefore counted as covered area. If the bubble is wobbling strongly due to the absence of a damping particle layer (compare Sec. 5.2.5), observing bubbles tilted towards and away from the observer is more common and leads to the computation of higher values of coverage. It should be noted that this is a fundamental bias of all projective measurements of the surface coverage using one camera only. The bias can be minimised by observing the bubble from the bottom position, which is however experimentally difficult to realise, or by fully reconstructing the 3D bubble surface using multiple cameras. It can be seen in Fig. 5.18 that the bias is small compared to the uncertainties induced by the wobbling of the bubble in general, and therefore no need was seen to further improve the data analysis here.

The time scales of the flotation can be obtained from Fig. 5.14 by fitting the model Eq. (5.19) from Sec. 5.1.4. T_{att} can be interpreted as the time scale to reach $1 - 1/e$ of the maximum coverage. It will be

5 Surface Attachment

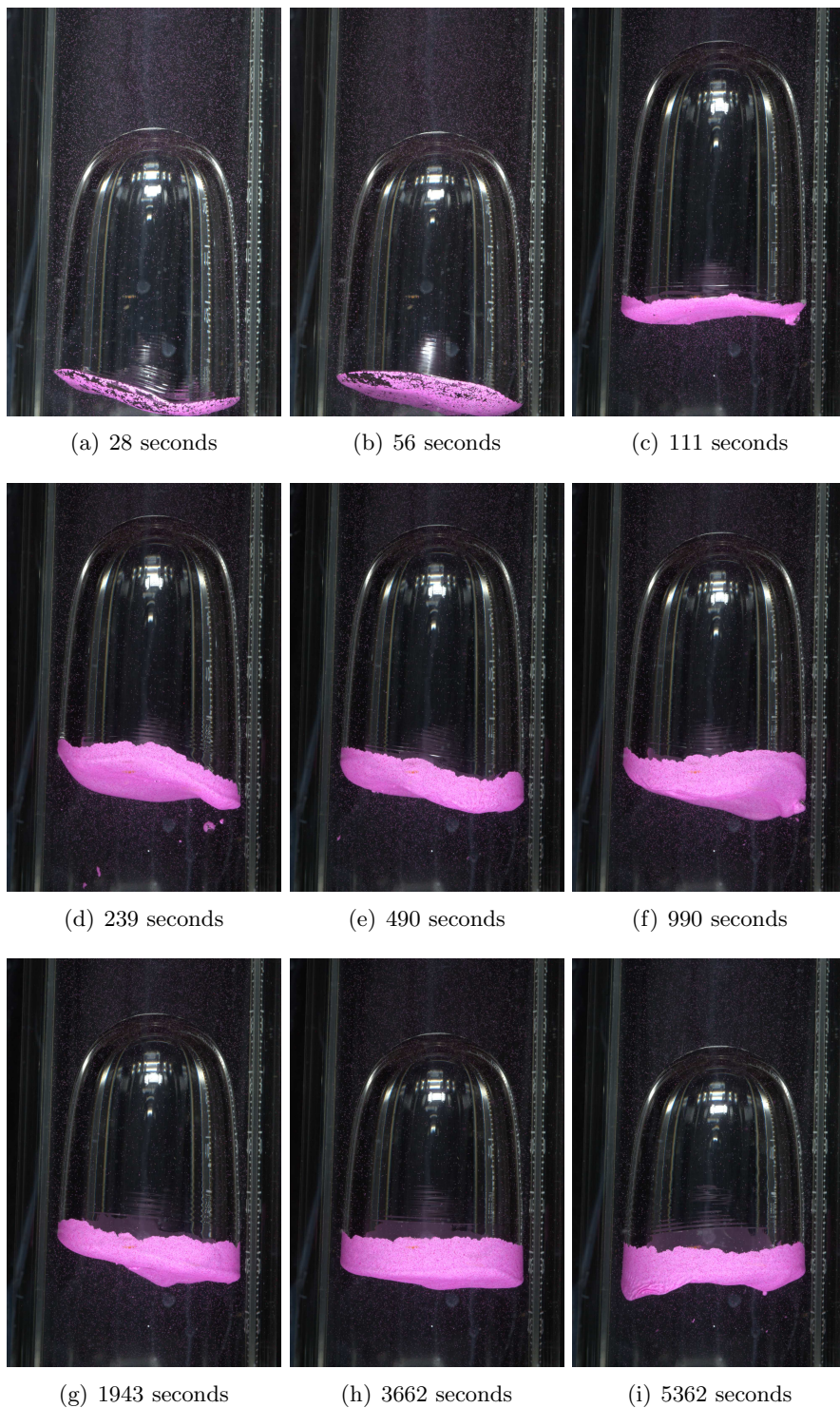


Figure 5.13: Selected records of a time series with a Taylor bubble, 6g PE particles of diameter $75\text{-}90\mu\text{m}$

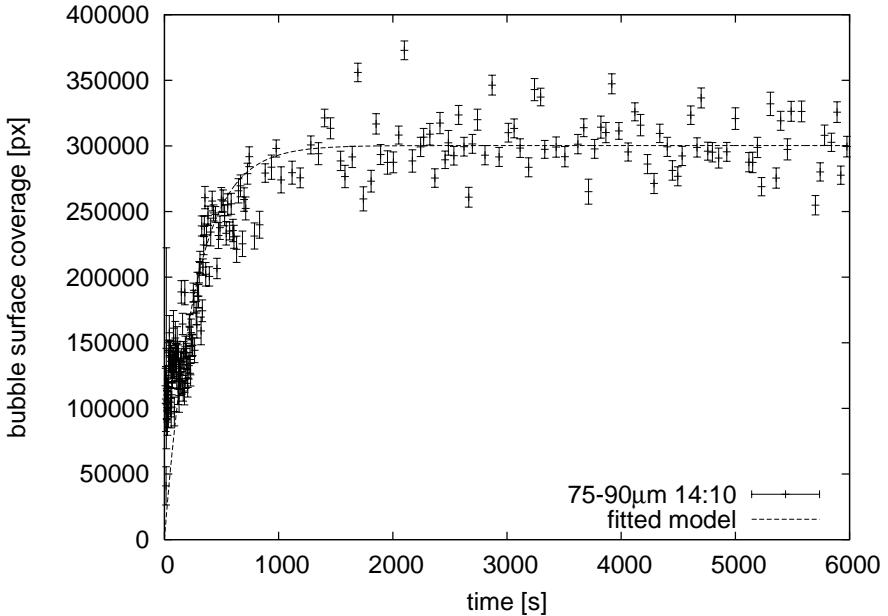


Figure 5.14: Time-development of the bubble surface area covered by particles; note the strong variations due to the wobbling of the bubble at the beginning of the experiment, directly after injection

called the *attachment time scale* in the following. For $t \rightarrow \infty$, the model Eq. (5.19) converges against a covered area A_0 , the *final coverage*. Values of both parameters are given in Tab. 5.3 for all experiments done with semi-spherical bubbles. It should be noted that the values for the final coverage A_0 are difficult to relate to the percentage of covered surface area, as the exact shape of the bubble is unknown (the semi-sphere is an approximation) and the perspective of the camera introduces a bias in the data analysis described in Sec. 5.2.3. The exact value is furthermore not of interest compared to the attachment time scale T_{att} ⁹, which is inversely proportional to the sweeping efficiency (the combined

⁹The total time a bubble needs to rise from the injection to the surface of a flotation cell is $\mathcal{O}(1) \dots \mathcal{O}(10)$ seconds for typical industrial applications; therefore, even a spherical-cap bubble with a high sweeping rate will not reach a full coverage of its rear side



Figure 5.15: Bias in the particle counting leading to the observed maximum in Fig. 5.14: Together with the pink particles detected at the bottom of the bubble, also the inner side of the bottom can be observed by refraction

flotation efficiency $P_{\text{float}} = P_{\text{enc}}P_{\text{att}}(1 - P_{\text{det}})$ with detachments excluded ($P_{\text{det}} = 0$) of the particular bubble.

The time-development of the covered surface area for different experiments is presented in Fig. 5.16. The data shows a strong scatter in particular the data recorded with the small particle sizes (Fig. 5.16 top). These were the early measurements for which also fewer records were taken than during the later experiments. Nevertheless, within a single data set, there is a reasonable agreement of the data with the predictions of the attachment model, i.e. a fast increase in the covered area followed by a decrease in the attachment rate until a somewhat stationary level is reached.

For the measurements with larger particles presented in Fig. 5.17, more records were taken and they also show a better match between

5.2 Measurements of Particle Attachment Rates

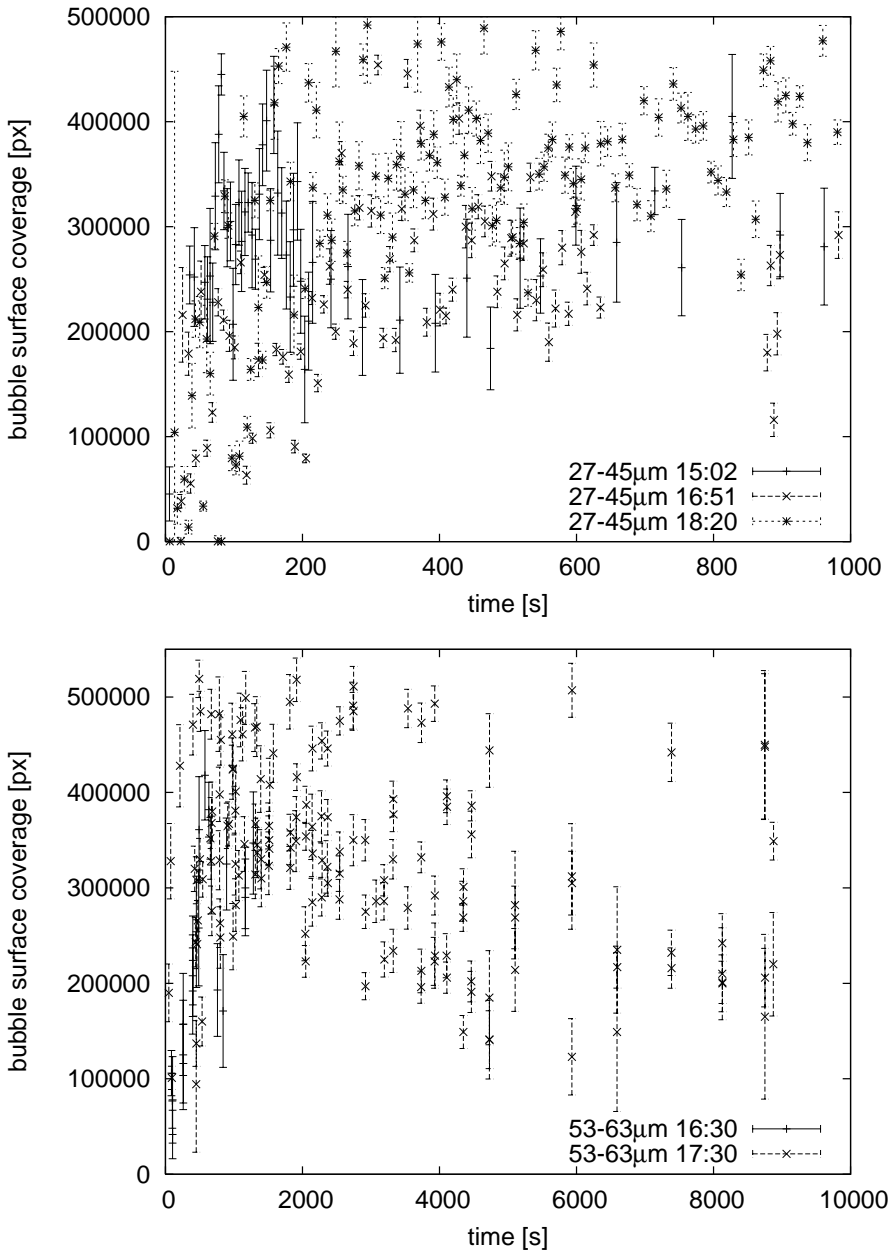


Figure 5.16: Projected covered surface area over time, 27-45 μm particles (top) and 53-63 μm particles (bottom), semi-spherical bubbles

5 Surface Attachment

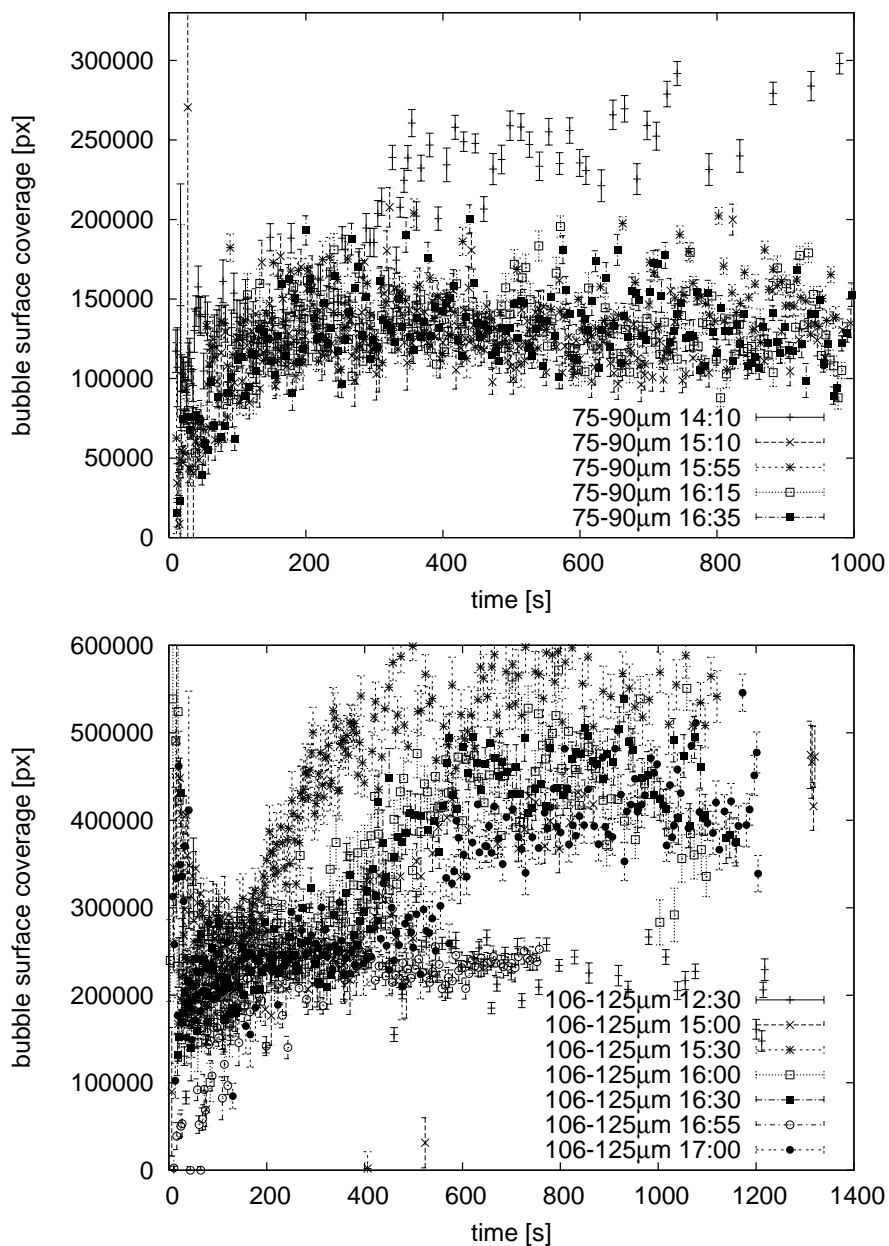


Figure 5.17: Projected covered surface area over time, 75-90 μm particles (top) and 106-125 μm particles (bottom), semi-spherical bubbles

different data sets. Qualitatively, the predicted behaviour of the attachment model can be verified again. However, more than half of the data sets show a second steep increase after some time when the stationary state has been reached according to the model. This behaviour coincides with the creeping of the monolayer over the rim of the semi-spherical bubble; see Tab. 5.3 for a more detailed analysis of this effect. Qualitatively, these measurements can only be explained by the model until the second sharp increase. Fitting the model to the data sets with the two-step behaviour naturally results in much larger attachment time scales than for the data sets that match the model's prediction. This can be seen in listing of all measured time scales in Tab. 5.3.

If all data sets are separated in two groups (the ones following the predictions of the model, and the ones showing a two-step behaviour), then Fig. 5.18 is obtained. In both cases, the time axis was furthermore normalised by the measured particle concentration (a concentration of approximately 750 detected maxima per cm^2 was normalised with a factor of one (this is approximately equivalent to a volume load of 10^{-4} for $100\mu\text{m}$ particles), as this was near the median concentration of all data sets), and the covered surface area by the final coverage area obtained from the fit. In the case of the measurements with a single-step behaviour, this normalisation leads to a good overlap of the graphs of the different measurements. This strongly supports the idea that there is no measurable effect of the particle size on the attachment rates in the performed experiments. In the case of the data sets showing the mentioned two-step behaviour, a higher number of outliers can be noticed shortly after injection, an effect that is related to the bias in the data analysis for strongly wobbling bubbles. The graphs from different measurements again match very well (within the scatter of the data) for times smaller than 200 seconds and larger than 600 seconds. In between, the second rapid increase in coverage occurs at different times for different experiments, such that the scatter there is significantly larger.

A comparison to an experiment with a wobbling-ellipsoidal bubble reveals that the time scales for the attachment rate are significantly larger in this case, see Fig. 5.19. This graph shows again the coverage, normalised with the final coverage obtained from the fit, over the time with the correction applied for the difference in the absolute particle concentration. The data shows much more scatter than in the cases of the semi-spherical bubbles, a result of the highly unsteady motion

5 Surface Attachment

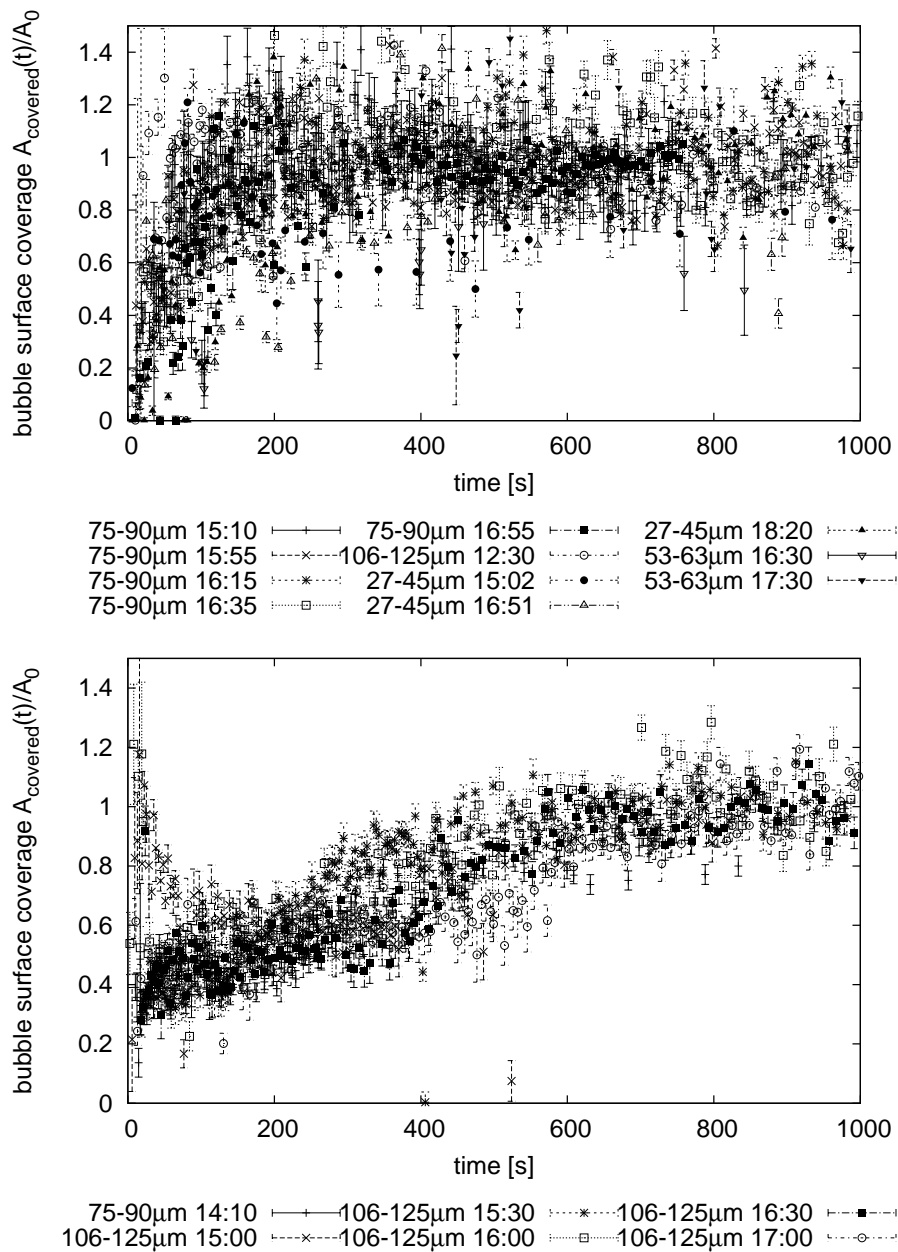


Figure 5.18: Covered surface area over time for semi-spherical bubbles showing an exponential increase according to the model (top) and with a two-step behaviour (bottom)

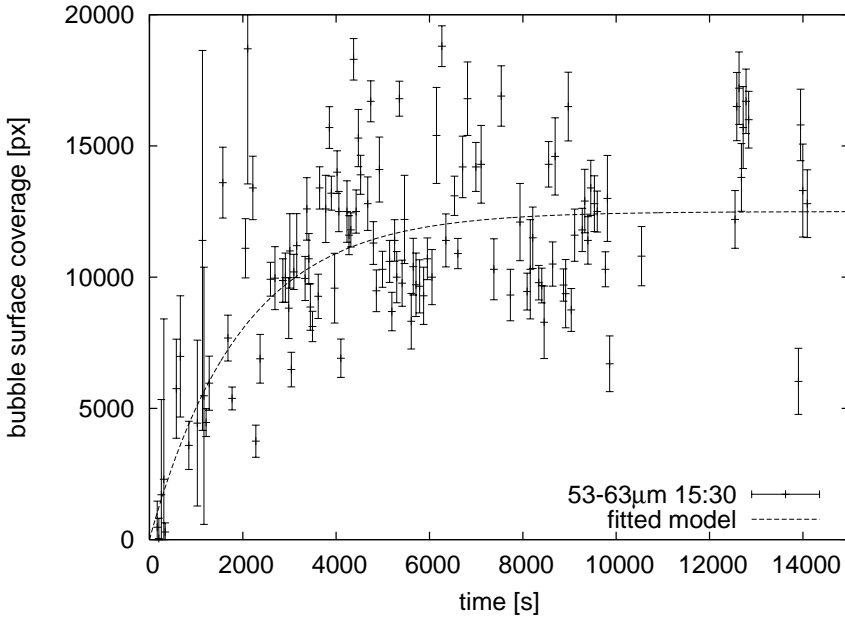


Figure 5.19: Covered surface area over time for a wobbling-ellipsoidal bubble; note the difference in time range

and chaotic oscillations of the bubble. This is also reflected in the much higher measurement uncertainties obtained from the data analysis method. Nevertheless, the data seems to agree with the model to a certain degree (the χ^2 of the fit is 10.1 in this case, which is comparable to the values obtained for the semi-spherical bubbles, see Tab. 5.3). The attachment time scale, however, is approximately 2000 seconds, a value that is one order of magnitude larger than the time scales of the bubbles with the two-step behaviour, and about a factor of 40 larger than the bubbles with only one step. The semi-spherical bubbles have a wake with complex vortex shedding and no stable vortex ring/recirculation zone at the rear side where a zone of highly turbulent flow is permanently in direct proximity to a part of the bubble surface. If the turbulence is assumed to have no influence on the attachment of particles, either by increasing the encounter rate or by quickening the rupture of the thin liquid film, it is difficult to argue that these bubbles show such a different result when bubble rise velocity (and thus flow rate) as well

5 Surface Attachment

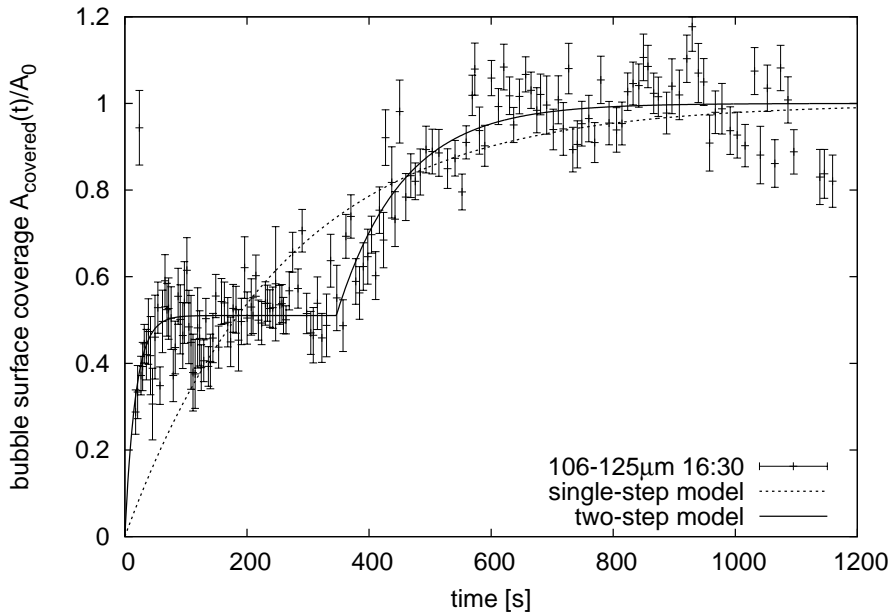


Figure 5.20: Observed two-step behaviour: the measured surface concentration of particles increases rather quickly and saturates, and a second exponential increase occurs after an initial delay; compare the images in Fig. 5.21

as the particle properties (size and material, the differences in absolute concentration is corrected by the normalisation of the time axis) are similar.

Tab. 5.3 lists the attachment time scales from the single-step fit for all experiments done with semi-spherical bubbles. The separation into the two groups is also obvious here, the short attachment time scales around 50 seconds correspond to the “fast” sweeping bubbles that agree with the model, and the ones with a larger time scales correspond to the measurements showing the two-step behaviour.

Two-Step Attachment

The two-step behaviour is illustrated in Fig. 5.20, showing the measured concentration increase. A series of images recorded during the same

5.2 Measurements of Particle Attachment Rates

Table 5.3: Attachment time scales T_{att} obtained from fitting Eq. (5.19) for all measured semi-spherical bubbles

particle size	attachment time scale T_{att} [s]	final coverage A_0 [px]	rms of residuals (reduced χ^2)
75-90 μm	211 \pm 8	3.00e5 \pm 2.7e3	3.69
	53 \pm 5	1.28e5 \pm 1.5e3	1.95
	55 \pm 6	1.43e5 \pm 2.0e3	3.49
	48 \pm 5	1.32e5 \pm 1.7e3	2.81
	54 \pm 4	1.32e5 \pm 1.7e3	2.79
	126 \pm 26	2.40e5 \pm 1.3e4	7.7
106-125 μm	36 \pm 5	2.55e5 \pm 4.5e3	5.8
	41 \pm 6	4.18e5 \pm 1.0e4	5.59
	203 \pm 12	5.60e5 \pm 1.1e4	2.73
	204 \pm 18	4.45e5 \pm 1.1e4	3.03
	277 \pm 20	4.7e5 \pm 1.2e4	2.50
	294 \pm 25	4.21e5 \pm 1.1e4	3.0
27-45 μm	39 \pm 22	3.68e5 \pm 2.9e4	5.82
	184 \pm 35	2.85e5 \pm 2.3e4	6.94
	206 \pm 20	3.66e5 \pm 8.8e3	6.35
53-63 μm	352 \pm 102	3.45e5 \pm 4.1e4	1.52
	172 \pm 73	3.81e5 \pm 1.2e4	6.37
Comparison: wobbling ellipsoidal bubble			
53-63 μm	1943 \pm 289	1.25e4 \pm 4.8e2	3.18

5 Surface Attachment

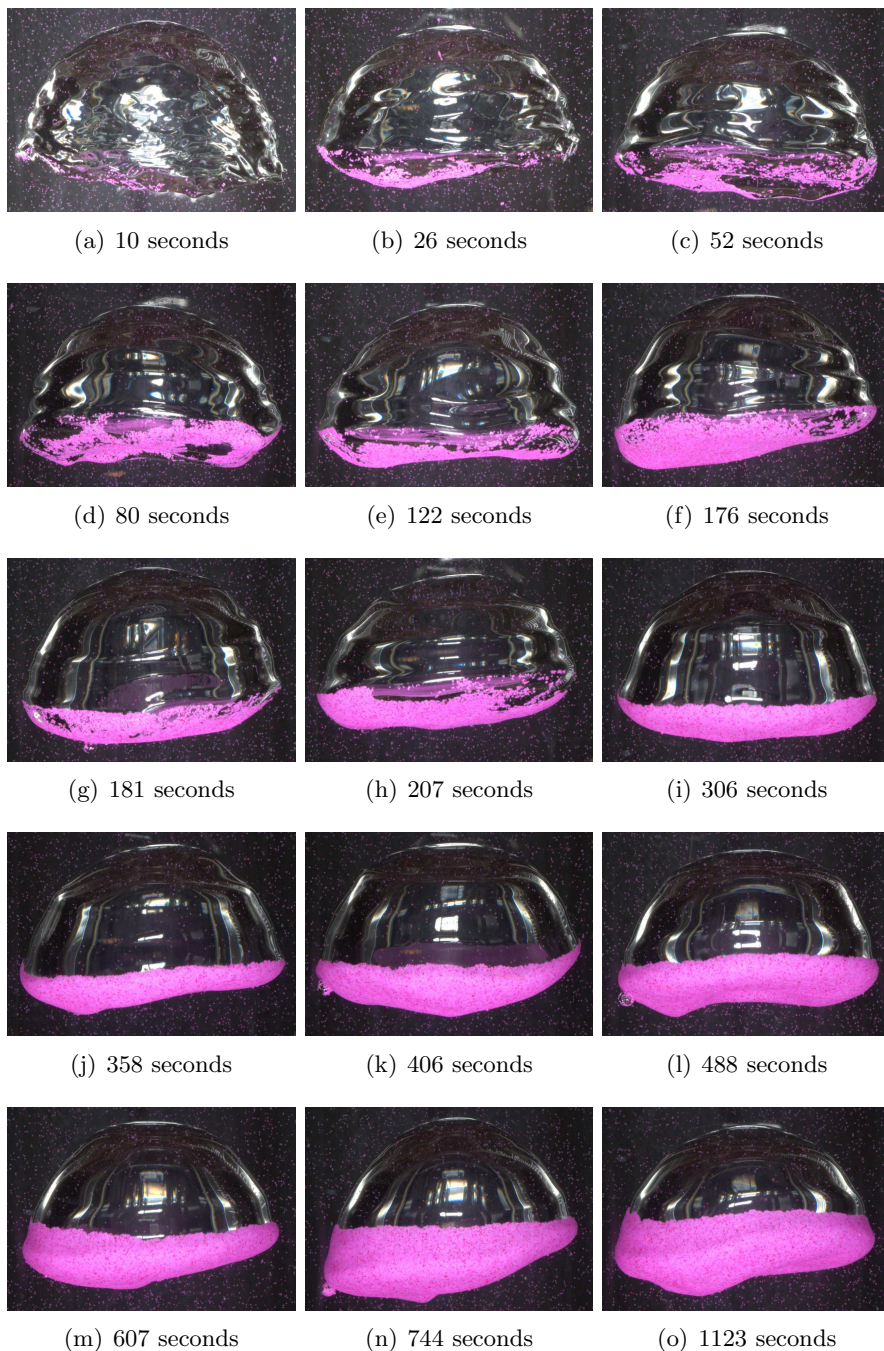


Figure 5.21: Time-series with a double-step behaviour (PE 106–125 μm particles): the second step at around $t_0 = 346 \pm 10\text{s}$ coincides with the point at which the monolayer creeps over the rim of the spherical cap, compare Fig. 5.20

measurement is presented in Fig. 5.21. Qualitatively, the occurrence of the second step coincides with the moment at which the monolayer starts creeping over the rim of the semi-spherical bubble, see in particular the images at times between 300 and 400 seconds in Fig. 5.21.

A fit for two exponential steps can be obtained from the function

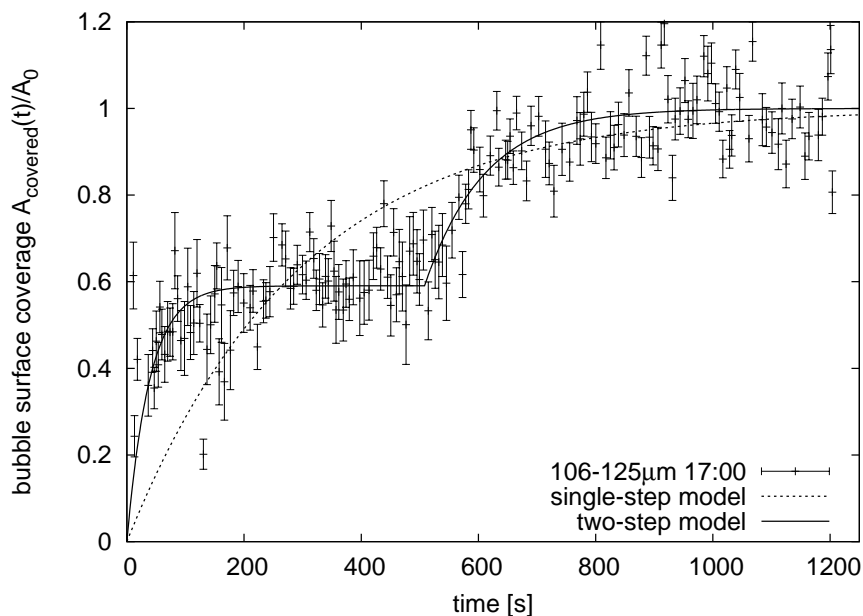
$$A_{\text{covered}}(t) = \begin{cases} A_1 \left(1 - \exp\left(-\frac{t}{T_{\text{att},1}}\right) \right), & \text{if } t \leq t_0 \\ A_1 \left(1 - \exp\left(-\frac{t}{T_{\text{att},1}}\right) \right) + A_2 \left(1 - \exp\left(-\frac{t-t_0}{T_{\text{att},2}}\right) \right), & \text{if } t > t_0 \end{cases} \quad (5.32)$$

with five unknown parameters and $A_0 = A_1 + A_2$. Fig. 5.20 shows an example of such a fit. It can be seen that this model provides a much better fit to this particular data set (variance of the residuals $\chi^2 = 2.1$, $\chi^2 = 6.3$ for the single-step model). The time scales obtained are $T_{\text{att},1} = 17\text{s} \pm 3\text{s}$, $T_{\text{att},2} = 108\text{s} \pm 17\text{s}$ with a delay time $t_0 = 346\text{s} \pm 10\text{s}$, compared to $277\text{s} \pm 20\text{s}$ for the single-step model. The initial time scale $T_{\text{att},1}$ is nevertheless biased towards smaller values because of the strong wobbling, see Sec. 5.2.2 for a description.

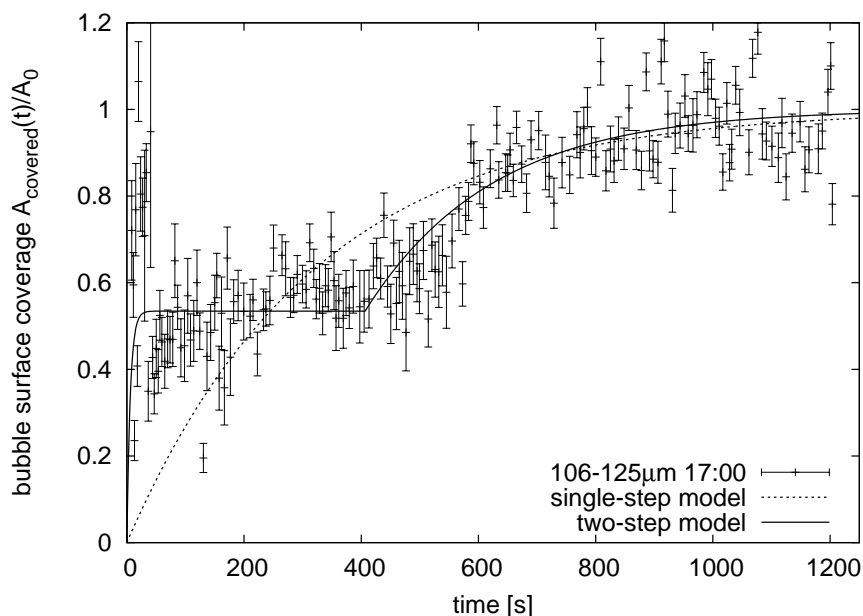
This bias is illustrated by the fit shown in Fig. 5.22. For the single-step model, the number of outliers due to wobbling is always small compared to the number of samples in the whole data set, and both fits give almost the same results within the margin of error ($296 \pm 12\text{s}$ versus $320 \pm 15\text{s}$), although the regression with outliers removed gives naturally the better fit ($\chi^2 = 6.35$ versus $\chi^2 = 8.97$). In the two-step model on the contrary, the initial time scale $T_{\text{att},1}$ changes from $39 \pm 6\text{s}$ (a value that agrees well with the earlier results from the “fast” sweeping bubbles) to $5.9 \pm 2.7\text{s}$ (a value almost one order of magnitude smaller than the earlier results) despite an only marginal decrease in the quality of the fit ($\chi^2 = 3.9$ instead of $\chi^2 = 3.3$). The time scale $T_{\text{att},2}$ is not influenced by the outliers (they only exist directly after injection of the bubble), but affected by the choice of the initial value of the delay time t_0 . The parameter correlation for both fits is -0.75 (outliers excluded) and -0.67 (outliers included), which confirms the strong (anti-)correlation between the two parameters. It must be concluded that the two-step model with five free parameters is already too complex¹⁰ for the regression of the measured data, and its results

¹⁰John von Neumann: “With four parameters I can fit an elephant, and with five I can make him wiggle his trunk.”

5 Surface Attachment



(a) Fit with outliers removed, and a large start value for t_0



(b) Fit including the outliers, and a small start value for t_0

Figure 5.22: Problems of the two-step model: two fits of the same data set showing very different results depending on the initial value of the delay time and the presence of outliers due to strong wobbling, see also the text

Table 5.4: Time scales obtained from the two-step model

particle size	$T_{\text{att},1}$ [s]	$T_{\text{att},2}$ [s]	t_0 [s]	χ^2
75-905 μm	16.1 ± 3.1	297 ± 26	187 ± 15	6.8
	17.4 ± 22.6	692 ± 106	303 ± 43	5.3
	8.5 ± 12	196 ± 26	122 ± 13	6.0
106-125 μm	32.9 ± 6.0	111 ± 26	312 ± 16	4.1
	17.5 ± 3.1	108 ± 17.6	346 ± 10	2.2
	38.9 ± 5.8	103 ± 24	508 ± 17	3.3

should be used and interpreted with care.

Tab. 5.4 summarises the resulting parameters of the two-step model. As discussed, the time scales of the initial step can be very small and uncertainties large, a result of the bias in the surface concentration measurement. It can still be concluded that these time scales are comparable to the short time scales found in Tab. 5.3. The time scales for the second step are larger, and there is a reasonable correspondence to the longer time scales found in Tab. 5.3.

5.2.6 Discussion of the Attachment Measurements

The experiments with the semi-spherical bubbles allow to obtain some insight about the mechanisms that improve the particle attachment rates in flotation, although drawing a final conclusion is not yet possible. If one hypothesises that particles attach to the front side of the bubble, one would expect that the attachment rate is constant over time, as the conditions (a clean surface) do not change over time (for semi-spherical bubbles). Nevertheless, it was observed that there is a noticeable decrease in attachment rates when the rear (wake) side of the bubble is filled with particles, which violates the assumption.

The observed two-step behaviour is more difficult to explain, and it was not expected from the simple attachment model. It is unlikely that it is caused by a sudden attachment rate at the front of the bubble. The duration of the change from the first plateau to the second one is in the order of 200 to 400 seconds, which excludes a sudden burst

5 Surface Attachment

of turbulence created upstream of the bubble in the settling chamber. In the latter case, several shorter increases would be much more likely, although they might not be visible due to the strong scattering of the data. It is more likely that small gaps open in the monolayer at random (e.g. near stagnation points), allowing new particles to attach. This is more and more prevented as the monolayer becomes densely packed. There is apparently some hysteresis when the rear side of the bubble is fully covered, as the shear stress prevents the attached particles moving over the rim. Once the boundary of the monolayer creeps over the rim, the stresses become lower again such that — at a lower rate — particles can attach again due to a higher probability for random small gaps. The whole attachment process finally stops if stresses are high enough that the monolayer is compressed to a dense packing again, preventing the creation of openings due to turbulence at the rear side.

Besides these conclusions that can be drawn from the qualitative behaviour alone, speculating over the exact cause of the particle attachment is difficult as the experimental results do not shed any light on this issue. The achievable resolution is limited to approximately $45\mu\text{m}$ due to the magnification and the diffraction-limited imaging. Resolving the thin liquid film is therefore not possible by the imaging system alone, ignoring all other practical problems that such an attempt would give. The analysis is therefore limited to “bulk” properties like the covered surface area, and there is no access to the microscopic processes involved in the particle attachment in this type of experiment. Having studied the wakes of a spherical cap (see Ch. 4), however, suggests that the expected turbulent particle flux (compare Eq. (5.6)) to the bubble surface is larger by one order of magnitude in the bubble wake compared to the low-turbulence flow approaching the bubble’s front. This one order of magnitude difference can also be found in the time scales of the coverage measurements; it can therefore be attributed to the turbulent particle encounter only. Nonetheless, it does not exclude other contributing effects of turbulence on the attachment itself, in particular the idea of Reeks *et al.* (1988) described in Sec. 5.1.3 for the particle detachment from a surface is intriguing: the thin liquid film separating particle and bubble is a dynamic system itself with eigenmodes in form of capillary waves. The amplification of these eigenmodes (and/or the weakened attenuation for smaller film thicknesses) is essential for the formation of a dimple that finally leads to the rupture of the film. A

5.2 Measurements of Particle Attachment Rates

turbulent flow would provide a spectral energy range that, if there is an overlap with the eigenspectrum of the thin liquid film, can in principle greatly reduce the time needed to cause these instabilities.

6 Applicability and Conclusion

6.1 The Wake Experiments and the Wake Model

To measure a contribution to the particle transport by the wakes of rising bubbles, PIV measurements were done on the wake of a solid spherical-cap model with the geometry of a typical spherical-cap bubble. Analysing the particle flux (excluding density effects) over the wake boundary did not give results of sufficient accuracy to support the existence of this effect. The particle concentration measurement on the contrary — despite still rather high measurement uncertainties — provide more evidence and show a clear trend that matches with the predictions of the derived model, although the scaling factor is not exactly unity.

The models — in particular the equations for the diffusive flux (Eq. (2.49)) — were derived with the intention to have simple scalar parameters that can easily be obtained from experiments. Consequently, the whole effect of turbulence was reduced to the rms of the velocity multiplied with an a-priori unknown scaling constant. Using the more general expression for the diffusive flux gives

$$\Phi_d = \int D_P|_{r=R_{\text{wake}}} \nabla \langle n_P \rangle_t \cdot d\mathbf{A}|_{r=R_{\text{wake}}} . \quad (6.1)$$

Better approximations for the local particle diffusion tensor D_P can be obtained from correlations of the particle phase velocity (Reeks, 1992).

Similarly to the diffusive flux, more general expressions for the inertial and the gravitational components can be obtained by integrating the particle slip velocity in normal direction over the wake boundary. This would automatically include turbophoresis in the mean transport term. A more general treatment therefore requires more detailed knowledge about the statistics of the flow, which is available from the PIV images for the performed experiments, but less so for most industrial applications. The simple model provides correct scaling relations also for these cases, but will require correction factors that are dependent on the conditions of the application (turbulence level in the outer flow, mean wake size, and mean rise velocity of the bubble).

For discriminating between the spherical and the elliptical wake models and/or other potentially influencing parameters, more accurate measurements are needed. Due to the different geometry, the elliptical-wake model showed a marginally better correlation with the experimental

data than the spherical-wake model, though the difference is statistically not significant. With the difference in the scaling constants obtained from the fit, the spherical wake model overpredicts the concentration increase by a factor of about 2 relative to the elliptical wake model, whose fitted slope is closer to unity. The models are assumed to describe the concentration increase in the wake of a spherical-cap gas bubbles as well, although with a potentially different scaling constant due to the free-slip boundary condition at the surface of the bubble.

A still open problem is the inclusion of the turbophoresis term into the model. The short analysis in Sec. 2.3.5 shows that the order of magnitude of the turbophoresis is seemingly small compared to the contribution of the time-averaged flow, but can be of the same order of magnitude in high-entropy regions as the free shear layers. The total contribution of turbophoresis is therefore difficult to estimate from the scaling arguments only. Nevertheless, its contribution is likely weaker in case of real gas bubbles with a free-slip boundary condition due to the weaker shear layers.

6.2 The Bubble Experiments

The experiments with the semi-spherical air bubbles can be summarised as following: After a very fast start, the particle attachment rates decrease as the rear side (wake side) of the bubble becomes covered with a mono layer of particles. After the coverage is completed, the remaining attachment rates are so low that no further growth of the covered area can be observed. In fact, the loss of bubble volume due to air dissolving in the water causes a reduction in surface area that leads to a slowly increasing coverage which is, in the performed experiments, indistinguishable from an increase in coverage due to attachment. What can be concluded is that the initial attachment rate can be solely related to the remaining free surface area at the rear of the bubble, and any other attachment rate is at least two orders of magnitude lower than the initial one and effectively not measurable in the performed experiments.

This leads to the conclusion that attachment at the bubble's front is insignificant compared to attachment at the rear. This is a consequence of the fact that the front side stays clean for the whole duration of the experiment, and only the rear side is covered. As soon as the rear side

6 Applicability and Conclusion

is covered with a mono layer of particles, then any further increase in coverage happens very slowly. This also coincides with the observations made for the wobbling-ellipsoidal bubbles: their wake is no stable toroidal vortex ring with strong turbulence in direct proximity to the bubble, the vortex shedding happens locally and in a chaotic manner. Consequently, only a slow increase in the particle attachment was observed. Another argument is the good agreement of the model derived in Sec. 5.1.4 with the experimental data in Sections 5.2.4 and 5.2.5. The only assumption needed for this model is an attachment rate proportional to the product constant attachment flux and the free, uncovered surface area in proximity to a turbulent wake.

As there is no reason why the rear side of the bubble is preferred for an attachment (gravity can be excluded because of the use of almost neutrally buoyant particles). The reasons for the observed differences should lie in the type of flow: laminar flow around the front part of the bubble versus a turbulent flow in its wake. The contribution of turbulence to the attachment rates can again be twofold:

1. turbulence increases the encounter rate, and
2. it can possibly reduce the film drainage time and thereby increase the attachment probability.

The increase in encounter rate is supported by the models described in Eq. (5.6); they suggest a linear scaling with the rms of the turbulent velocity fluctuations. The second argument is more subtle, and it needs the “Rock’n’Roll” idea of Reeks *et al.* (1988) described in Sec. 5.1.3: for the detachment process, the spectrum of turbulent kinetic energy attenuates oscillations of attached particles in the near-wall potential if there is resonance (overlap with the spectrum of the particle oscillations). Similarly, if there is resonance between the spectrum of the capillary waves of the thin liquid film separating particle and interface, then turbulence can also enhance the attachment rates by a stronger amplification of the instabilities of the thin film. For the moment, there is no possibility to draw a conclusion about this enhancement from the performed experiment, and the presented reasoning certainly remains speculative. But as an afterthought it points into a direction that is very interesting for a future study, experimental and theoretical.

6.3 Applicability of the Results

The intention of the project that led to this work was to obtain more insight into the mechanisms that contribute to the particle transport in flotation. This section provides some examples how the obtained results can be used to approach problems in the optimisation of the flotation efficiency in industrial applications.

6.3.1 Make it Turbulent!

The experiments show that turbulence can have a positive and sometimes operative effect on the obtained flotation rates if certain conditions are met. Most obvious is the $\propto u_{\text{rms}}$ scaling of the particle encounter rate in a turbulent flow, see Eq. (5.6). A high turbulence level in the whole domain would therefore also enhance the attachment rates for smaller, spherical and in particular wobbling-ellipsoidal bubbles. For larger, more quiescent facilities, it would be beneficial to inject bubbles of the size of a spherical cap, as this type of bubbles provides clearly higher attachment rates than wobbling-ellipsoidal bubbles, with the additional benefit of the most effective particle transport in the wake due to a large wake volume and a stable vortex ring.

6.3.2 Scaling of Wake Entrainment with Bubble Volume

Davies & Taylor (1950) derived the simple relation (as shown by Joseph (2003), it holds for perfect spherical caps with vanishing viscosity and surface tension)

$$\frac{U_{\infty}^2}{gR_{\text{curv}}} = \text{Fr}^2 = \frac{4}{9} \quad (6.2)$$

for the bubble rise velocity of a spherical-cap bubble as a function of the radius of curvature R_{curv} of the bubble's front. Eq. (6.2) together with Eq. (2.59) gives the scaling of the concentration increase with bubble size

$$\frac{n_{P,\text{wake}}}{n_{P,\text{exterior}}} - 1 \propto \frac{U_{\infty}}{u_{\text{rms}}} \frac{U_{\infty}}{R_{\text{curv}}} \propto \frac{1}{\sqrt{R_{\text{curv}}} f(\text{Re})}. \quad (6.3)$$

In other word, smaller bubbles tend to have higher concentration differences due to the smaller radius of curvature. The scaling of the total

6 Applicability and Conclusion

amount of inclusions removed over the injected amount of gas therefore becomes

$$\frac{\text{concentration} \cdot \text{wake volume}}{\text{injected volume}} \propto \frac{V^{-1/6}}{f(Re)}, \quad (6.4)$$

if a constant wake-to-bubble volume ratio is assumed. Excluding the Re-dependent changes in average turbulence intensity in and size of the wake, there is a weak negative scaling $\propto V_{\text{bubble}}^{1/6}$ in transport efficiency with increasing bubble volume.

6.3.3 Estimates of Removal Rates

A comparison of the efficiency of the wake-induced transport and the transport due to particle attachment can be made exemplary for spherical-cap bubbles, if it is assumed that the results for the attachment rates of the semi-spherical bubbles are representative also in the case of a freely rising bubble.

A spherical-cap air bubble with a volume of 2cm^3 in water would have a rise velocity of $U_\infty = 18.5\text{cm/s}$, an Eötvös number of $Eu = 33$, a Froude number of $Fr = 4/9$ and a Reynolds number of about $Re = 2900$. Assuming a typical rim angle of $\theta_0 = 50^\circ$ results in a shape factor for the spherical wake model (compare Eq. (2.60)) of 1.27. For the $\rho_P = 0.98\text{g/cm}^3$ PE particles with a diameter of $50\mu\text{m}$, the modified particle response time (see Eq. (2.54)) is $\tau_{P*} = 1.1 \cdot 10^{-5}\text{s}$. With an assumed turbulence level of $u_{\text{rms}}/U_\infty = 0.2$, the relative increase in particle concentration according to the spherical wake model Eq. (2.59) is only $1.7 \cdot 10^{-3}$, therefore the wake only contributes insignificantly to the overall transport in this case. The situation is different in the case of an Argon bubble of the same volume rising in liquid steel ($\rho_F = 6.9 \cdot 10^3\text{kg/m}^3$, $\sigma = 1800\text{g/s}^2$ at 1823K , compare Li *et al.* (2005)) results approximately in a 3.5% increase in particle concentration inside the wake for a $50\mu\text{m}$ Al_2O_3 particle ($\rho_{\text{Al}_2\text{O}_3} = 4\text{g/cm}^3$).

In the attachment model Eq. (5.19), the attachment time scale $T_{\text{att}} = 1/j_{\text{att}}A_P$ is approximately 50s for the performed experiments. The attachment flux density for the experiments can therefore be estimated as $j_{\text{att}} = 101/\text{s mm}^2$. This value was obtained for the semi-spherical bubbles with $A_0 \approx 10\text{cm}^2$ and a volume load of approximately $\Phi = 10^{-4}$, the value of the rear area of a 2cm^3 spherical-cap bubble is $A_0 = 4.1\text{cm}^2$. With a total process time of 10 seconds, such a spherical bubble can

sweep approximately 4000 particles at a volume load of 10^{-4} , these values are independent of particle size and density. The wake of the 2cm^2 bubble has a volume of approximately 20cm^3 (for a spherical wake, more if an ellipsoidal wake is assumed), and with a concentration of 1500 particles per cm^3 (equivalent to a volume load of 10^{-4} $50\mu\text{m}$ particles) gives approximately 30000 particles per wake. A 3.5% increase in particle concentration would therefore result in an effective transport of ca. 1000 particles per wake, or about one quarter of the particles removed by direct attachment. It can therefore be concluded that for long rising time the transport rate due to particle attachment is more effective than the increase in wake concentration, although the latter can have a comparable magnitude if the rising times of bubbles are short. As both the attachment flux j_{att} and the wake concentration n_{wake} are linear in the total particle concentration, their ratio does not change with absolute particle concentration in the flow.

This short calculation shows that both contributions can have an impact on the optimisation of flotation processes and should be considered.

Bibliography

- ADRIAN, RONALD J. & WESTERWEEL, JERRY 2010 *Particle Image Velocimetry*. Cambridge University Press.
- AHMADI, G. & GOLDSCHMIDT, V. W. 1971 Motion of particles in a turbulent fluid—the basset history term. *Journal of Applied Mechanics* **38** (2), 561–563.
- AUTON, T. R. 1987 The lift force on a spherical body in a rotational flow. *J. Fluid. Mech.* **183**, 199–218.
- AUTON, T. R., HUNT, J. C. R. & PRUD'HOMME, M. 1988 The force exerted on a body in inviscid unsteady non-uniform rotational flow. *J. Fluid. Mech.* **197**, 241–257.
- BAGCHI, PROSENJIT & BALACHANDAR, S. 2004 Response of the wake of an isolated particle to an isotropic turbulent flow. *Journal of Fluid Mechanics* **518**, 95–123.
- BASSET, A. B. 1888 On the motion of a sphere in a viscous liquid. *Philosophical Transactions of the Royal Society of London. A* **179**, pp. 43–63.
- BATCHELOR, G. K. 1967 *An Introduction to Fluid Dynamics*. Cambridge University Press.
- BEARD, KENNETH V. & CHUANG, CATHERINE 1987 A new model for the equilibrium shape of raindrops. *J. Atmos. Sci.* **44** (11), 1509–1524.
- BHAGA, D. & WEBER, M. E. 1981 Bubbles in viscous liquids: shapes, wakes and velocities. *J. Fluid. Mech.* **105** (-1), 61–85.
- BOUSSINESQ, JOSEPH 1885a *Application des potentiels à l'étude de l'équilibre et du mouvement des solides élastiques: principalement*

Bibliography

au calcul des déformations et des pressions que produisent, dans ces solides, des efforts quelconques exercés sur une petite partie de leur surface ou de leur intérieur: mémoire suivi de notes étendues sur divers points de physique, mathématique et d'analyse. Gauthier-Villars.

BOUSSINESQ, JOSEPH 1885*b* Sur la résistance qu'oppose un liquide indéfini en repos. *CR Acad. Sci. Paris* **100**, 935–937.

BOUSSINESQ, JOSEPH 1903 *Théorie analytique de la chaleur*. Gauthier-Villars.

BRÜCKER, CH. 1996 3-d scanning-particle-image-velocimetry: Technique and application to a spherical cap wake flow. *Appl. Sci. Res.* **56**, 157–179, 10.1007/BF02249379.

CALZAVARINI, E., VOLK, R., BOURGOIN, M., LÉVÊQUE, E., PINTON, J.-F. & TOSCHI, F. 2009 Acceleration statistics of finite-sized particles in turbulent flow: the role of Faxén forces. *J. Fluid. Mech.* **630**, 179–189.

CAPLAN, NICHOLAS & GARDNER, TREVOR N. 2007 A fluid dynamic investigation of the big blade and macon oar blade designs in rowing propulsion. *Journal of Sports Sciences* **25** (6), 643–650, PMID: 17454531.

CHESTER, W., BREACH, D. R. & PROUDMAN, IAN 1969 On the flow past a sphere at low reynolds number. *Journal of Fluid Mechanics* **37**, 751–760.

CLIFT, R., GRACE, J.R. & WEBER, M.E. 2005 *Bubbles, Drops, and Particles*. Dover Publications, Inc.

COPPUS, JHC, RIETEMA, K & OTTENGRAF, SPP 1977 Wake phenomena behind spherical-cap bubbles and solid spherical-cap bodies. *T. I. Chem. Eng.-Lond.* **55** (2), 122–129.

CORRSIN, S. & LUMLEY, J. 1956 On the equation of motion for a particle in turbulent fluid. *Applied Scientific Research, Section A* **6** (2-3), 114–116.

- DAUDA, MICHAEL 2011 Gas hold-up dependency on polymer concentration in water. Master's thesis, Delft University of Technology.
- DAVIES, R. M. & TAYLOR, GEOFFREY 1950 The mechanics of large bubbles rising through extended liquids and through liquids in tubes. *Proceedings of the Royal Society of London. Series A. Mathematical and Physical Sciences* **200** (1062), 375–390.
- DAYAN, ABRAHAM & ZALMANOVICH, SILVIA 1982 Axial dispersion and entrainment of particles in wakes of bubbles. *Chem. Eng. Sci.* **37** (8), 1253 – 1257.
- DELFO, RENÉ 1996 Experiments on air entrainment from a stationary slug bubble in a vertical tube. PhD thesis, Technische Universiteit Delft.
- DOBBY, G.S. & FINCH, J.A. 1987 Particle size dependence in flotation derived from a fundamental model of the capture process. *International Journal of Mineral Processing* **21** (3-4), 241 – 260.
- EINSTEIN, ALBERT 1905 On the movement of small particles suspended in stationary liquids required by the molecular-kinetic theory of heat. *Ann. d. Phys.* **17**, 549–560.
- ELGHOBASHI, S. 1994 On predicting particle-laden turbulent flows. *Applied Scientific Research* **52** (4), 309–329.
- EVANS, HUMBERTO BOCANEGRA 2013 Glowing droplets : a diagnostic for particle-laden flows. PhD thesis, Eindhoven University of Technology.
- FAN, LIANG-SHIN & TSUCHIYA, KATSUMI 1990 *Bubble wake dynamics in liquids and liquid-solid suspensions*. Butterworth-Heinemann Series in Chemical Engineering.
- FAXÉN, HILDING 1922 Der Widerstand gegen die Bewegung einer starren Kugel in einer zähen Flüssigkeit, die zwischen zwei parallelen ebenen Wänden eingeschlossen ist. *Annalen der Physik* **373** (10), 89–119.

Bibliography

- FLEMING, PHILIP J. & WALLACE, JOHN J. 1986 How not to lie with statistics: the correct way to summarize benchmark results. *Commun. ACM* **29**, 218–221.
- FRIEDLANDER, SHELDON K. 2000 *Smoke, dust, and haze: Fundamentals of Aerosol Dynamics*. Oxford University Press, New York.
- GATIGNOL, R. 1983 The Faxén formulae for a rigid particle in an unsteady non-uniform stokes flow. *J. Mec. Theor. Appl* **2** (2), 143–160.
- GAUDIN, A.M. 1957 *Flotation*, 2nd edn. McGraw-Hill Book Company, Inc.
- GIFFARD, AUDREY 2011 Optical determination of flotation efficiency in a water tank.
- GOLDSTEIN, SYDNEY 1929 The steady flow of viscous fluid past a fixed spherical obstacle at small reynolds numbers. *Proceedings of the Royal Society of London. Series A, Containing Papers of a Mathematical and Physical Character* **123** (791), pp. 225–235.
- GUO, JUNKE 2011 Motion of spheres falling through fluids. *Journal of Hydraulic Research* **49** (1), 32–41.
- VAN HAARLEM, BAS ADRIAAN 2000 The dynamics of particles and droplets in atmospheric turbulence - a numerical study. PhD thesis, Delft University of Technology.
- HADDAD, R.A. & AKANSU, A.N. 1991 A class of fast gaussian binomial filters for speech and image processing. *Signal Processing, IEEE Transactions on* **39** (3), 723–727.
- HALIR, RADIM & FLUSSER, JAN 1998 Numerically stable direct least squares fitting of ellipses.
- HARDALUPAS, Y., TAYLOR, A. M. K. P. & WHITELAW, J. H. 1992 Particle dispersion in a vertical round sudden-expansion flow. *Phil. Trans. R. Soc. Lond. A* **341** (1662), 411–442.
- HILL, M. J. M. 1894 On a spherical vortex. *Philosophical Transactions of the Royal Society of London. (A.)* **185**, 213–245.

- VAN HINSBERG, M.A.T., TEN THIJE BOONKAMP, J.H.M. & CLERCX, H.J.H. 2011 An efficient, second order method for the approximation of the basset history force. *Journal of Computational Physics* **230** (4), 1465 – 1478.
- HINZE, J.O. 1975 *Turbulence*. McGraw-Hill Book Company.
- HJELMFELT, A. & MOCKROS, L. 1966 Motion of discrete particles in a turbulent fluid. *Applied Scientific Research* **16**, 149–161, 10.1007/BF00384062.
- JOSEPH, DANIEL D. 2003 Rise velocity of a spherical cap bubble. *Journal of Fluid Mechanics* **488**, 213–223.
- KAMBE, TSUTOMU 2003 Gauge principle for flows of an ideal fluid. *Fluid Dynamics Research* **32** (5), 193 – 199.
- KLESHNEV, VALERY 1999 Propulsive efficiency of rowing. In *Proceedings of the XVII International Symposium on Biomechanics in Sports*, pp. 224–228.
- LANDAU, L.D. & LIFSHITZ, E.M. 1987 *Fluid Mechanics*, 2nd edn., *Course of Theoretical Physics*, vol. 6. Butterworth–Heinemann.
- LEIGHTON, DAVID & ACRIVOS, ANDREAS 1985 The lift on a small sphere touching a plane in the presence of a simple shear flow. *Z. Angew. Math. Phys.* **36**, 174–178, 10.1007/BF00949042.
- LI, Z., MUKAI, K., ZEZE, M. & MILLS, K.C. 2005 Determination of the surface tension of liquid stainless steel. *Journal of Materials Science* **40** (9-10), 2191–2195.
- LIAO, SHI-JUN 2002 An analytic approximation of the drag coefficient for the viscous flow past a sphere. *International Journal of Non-Linear Mechanics* **37** (1), 1 – 18.
- LIGHTHILL, M. J. 1956a Drift. *Journal of Fluid Mechanics* **1**, 31–53.
- LIGHTHILL, M. J. 1956b The image system of a vortex element in a rigid sphere. *Mathematical Proceedings of the Cambridge Philosophical Society* **null**, 317–321.

Bibliography

- LIGHTHILL, M. J. 1957 Contributions to the theory of the pitot-tube displacement effect. *Journal of Fluid Mechanics* **2**, 493–512.
- LINDBERG, TONY 1993 Detecting salient blob-like image structures and their scales with a scale-space primal sketch: A method for focus-of-attention. *International Journal of Computer Vision* **11** (3), 283–318.
- MACKENZIE, BRIAN R. & KIORBOE, THOMAS 2000 Larval fish feeding and turbulence: A case for the downside. *Limnology and Oceanography* **45** (1), 1–10.
- MACKENZIE, BRIAN R., MILLER, THOMAS J., CYR, STEPHANE & LEGGETT, WILLIAM C. 1994 Evidence for a dome-shaped relationship between turbulence and larval fish ingestion rates. *Limnology and Oceanography* **39** (8), 1790–1799.
- MAGNAUDET, JACQUES 2003 Small inertial effects on a spherical bubble, drop or particle moving near a wall in a time-dependent linear flow. *J. Fluid Mech.* **485**, 115–142.
- MAGNAUDET, J. & EAMES, I. 2000 The motion of high-reynolds-number bubbles in inhomogeneous flows. *Annual Review of Fluid Mechanics* **32** (1), 659–708.
- MANN, J., OTT, S., PÉCSELI, H. L. & TRULSEN, J. 2005 Turbulent particle flux to a perfectly absorbing surface. *Journal of Fluid Mechanics* **534**, 1–21.
- MARCHIOLI, CRISTIAN, FANTONI, MARCO & SOLDATI, ALFREDO 2007 Influence of added mass on anomalous high rise velocity of light particles in cellular flow field: A note on the paper by maxey (1987). *Physics of Fluids* **19** (9), 098101.
- MAXEY, M. R. 1987 The motion of small spherical particles in a cellular flow field. *Physics of Fluids* **30** (7), 1915–1928.
- MAXEY, MARTIN R. & RILEY, JAMES J. 1983 Equation of motion for a small rigid sphere in a nonuniform flow. *Phys. Fluids* **26** (4), 883–889.

- MAXWORTHY, T. 1967 A note on the existence of wakes behind large, rising bubbles. *Journal of Fluid Mechanics* **27** (02), 367–368.
- MAZUR, P. & BEDEAUX, D. 1974 A generalization of Faxén’s theorem to nonsteady motion of a sphere through an incompressible fluid in arbitrary flow. *Physica* **76** (2), 235 – 246.
- MAZZITELLI, IRENE M. 2003 Turbulent bubbly flow. PhD thesis, University of Twente, Enschede.
- MEI, R. 1996 Velocity fidelity of flow tracer particles. *Exp. Fluids* **22** (1), 1–13.
- MICHAELIDES, E.E. 1992 A novel way of computing the basset term in unsteady multiphase flow computations. *Physics of Fluids A* **4** (7), 1579–1582, cited By (since 1996)24.
- MONCHAUX, R., BOURGOIN, M. & CARTELLIER, A. 2010 Preferential concentration of heavy particles: A voronoï analysis. *Physics of Fluids* **22** (10), 103304.
- NGUYEN, A.V., SCHULZE, H.J. & RALSTON, J. 1997 Elementary steps in particle–bubble attachment. *International Journal of Mineral Processing* **51** (1-4), 183 – 195, *Application of Surface Science to Advancing Flotation Technology*.
- NGUYEN, A. V. 1994 The collision between fine particles and single air bubbles in flotation. *Journal of Colloid and Interface Science* **162** (1), 123 – 128.
- NGUYEN, ANH V, RALSTON, JOHN & SCHULZE, HANS J 1998 On modelling of bubble–particle attachment probability in flotation. *International Journal of Mineral Processing* **53** (4), 225 – 249.
- NGUYEN, ANH V. & SCHULZE, HANS JOACHIM 2004 *Colloidal Science of Flotation*. Marcel Dekker Inc.
- OSEEN, CARL WILHELM 1927 *Neuere Methoden und Ergebnisse in der Hydrodynamik*. Akad. Verl.-Ges.
- PARLANGE, JEAN-YVES 1969 Spherical cap bubbles with laminar wakes. *Journal of Fluid Mechanics* **37** (02), 257–263.

Bibliography

- PÉCSELI, H.L., TRULSEN, J. & FIKSEN, Ø. 2012 Predator–prey encounter and capture rates for plankton in turbulent environments. *Progress in Oceanography* **101** (1), 14 – 32.
- PÉCSELI, H. L. & TRULSEN, J. 2007 Turbulent particle fluxes to perfectly absorbing surfaces: a numerical study. *Journal of Turbulence* p. N42.
- PÉCSELI, H. L. & TRULSEN, J. 2010 Transit times in turbulent flows. *Phys. Rev. E* **81**, 046310.
- PLOUG, HELLE 2008 Cyanobacterial surface blooms formed by aphanizomenon sp. and nodularia spumigena in the baltic sea: Small-scale fluxes, ph, and oxygen microenvironments. *Limnol. Oceanogr.* **53** (3), 914–921.
- POELMA, CHRISTIAN 2004 Experiments in particle-laden turbulence. PhD thesis, Technische Universiteit Delft.
- POPE, ROBIN M. & FRY, EDWARD S. 1997 Absorption spectrum (380–700 nm) of pure water. ii. integrating cavity measurements. *Appl. Opt.* **36** (33), 8710–8723.
- PRANDTL, L 1904 Über flüssigkeitsbewegung bei sehr kleiner reibung. *Collected papers* **2**, 575–584.
- PROBSTEIN, RONALD F. 2003 *Physiochemical Hydrodynamics*, second edition edn. John Wiley & Sons, Inc.
- PROUDMAN, IAN & PEARSON, J. R. A. 1957 Expansions at small reynolds numbers for the flow past a sphere and a circular cylinder. *Journal of Fluid Mechanics* **2**, 237–262.
- RALSTON, J., DUKHIN, S.S. & MISHCHUK, N.A. 2002 Wetting film stability and flotation kinetics. *Advances in Colloid and Interface Science* **95** (2-3), 145 – 236.
- REEKS, M.W. & HALL, D. 2001 Kinetic models for particle resuspension in turbulent flows: theory and measurement. *Journal of Aerosol Science* **32** (1), 1 – 31.

- REEKS, M. W. 1992 On the continuum equations for dispersed particles in nonuniform flows. *Phys. Fluids A-Fluid* **4** (6), 1290–1303.
- REEKS, M. W. & MCKEE, S. 1984 The dispersive effects of basset history forces on particle motion in a turbulent flow. *Physics of Fluids* **27** (7), 1573–1582.
- REEKS, M W, REED, J & HALL, D 1988 On the resuspension of small particles by a turbulent flow. *Journal of Physics D: Applied Physics* **21** (4), 574.
- RICHARDSON, LEWIS F. 1926 Atmospheric diffusion shown on a distance-neighbour graph. *Proceedings of the Royal Society of London. Series A, Containing Papers of a Mathematical and Physical Character* **110** (756), pp. 709–737.
- ROTHENBERG, THOMAS J., FISHER, FRANKLIN M. & TILANUS, C. B. 1964 A note on estimation from a cauchy sample. *Journal of the American Statistical Association* **59** (306), pp. 460–463.
- RUBEY, WILLIAM W. 1933 Settling velocity of gravel, sand, and silt particles. *Am. J. Sci.* **25**, 325–338.
- SAFFMAN, P. G. 1956 On the motion of small spheroidal particles in a viscous liquid. *Journal of Fluid Mechanics* **1**, 540–553.
- SAFFMAN, P. G. 1965 The lift on a small sphere in a slow shear flow. *J. Fluid. Mech.* **22** (02), 385–400.
- SAFFMAN, PHILIP G 1992 *Vortex dynamics*. Cambridge University Press.
- SCHULZE, H.J. 1992 Probability of particle attachment on gas bubbles by sliding. *Advances in Colloid and Interface Science* **40** (0), 283 – 305.
- SEITER, C. & ALDER, B.J. 1978 The chemical potential for dilute hard-sphere mixtures. *Journal of Solution Chemistry* **7** (2), 73–79.
- SEZGIN, MEHMET & SANKUR, BÜLENT 2004 Survey over image thresholding techniques and quantitative performance evaluation. *Journal of Electronic Imaging* **13** (1), 146 – 165.

Bibliography

- STOKES, G. G. 1851 On the Effect of the Internal Friction of Fluids on the Motion of Pendulums. *Transactions of the Cambridge Philosophical Society* **9**, 8.
- SUTHERLAND, K. L. 1948 Physical chemistry of flotation. xi. kinetics of the flotation process. *The Journal of Physical and Colloid Chemistry* **52** (2), 394–425.
- TENNEKES, H. & LUMLEY, JOHN L. 1972 *A first course in turbulence*. MIT Press.
- THEN, CHAN-MOU 1947 Mean value and correlation problems connected with the motion of small particles suspended in a turbulent fluid. PhD thesis, Technische Hogeschool te Delft.
- THOMAS, P. J. 1992 On the influence of the basset history force on the motion of a particle through a fluid. *Phys. Fluids A-Fluid* **4** (9), 2090–2093.
- VEYSEY, II, J. & GOLDENFELD, N. 2007 Simple viscous flows: From boundary layers to the renormalization group. *Rev. Mod. Phys.* **79**, 883–927.
- VOJIR, D.J. & MICHAELIDES, E.E. 1994 Effect of the history term on the motion of rigid spheres in a viscous fluid. *International Journal of Multiphase Flow* **20** (3), 547 – 556.
- WARNCKE, N. G. W., DELFOS, R. & WESTERWEEL, J. 2009 Particle transport in turbulent wakes behind spherical caps. In *Advances in Turbulence XII* (ed. Bruno Eckhardt), *Springer Proceedings in Physics*, vol. 132, pp. 513–516. Springer Berlin Heidelberg, 10.1007/978-3-642-03085-7_123.
- WEGENER, P P & PARLANGE, J Y 1973 Spherical-cap bubbles. *Annu. Rev. Fluid. Mech.* **5** (1), 79–100.
- WU, J.-S. & FAETH, G. M. 1994 Sphere wakes at moderate Reynolds numbers in a turbulent environment. *AIAA Journal* **32**, 535–541.
- WU, J S & FAETH, G M 1995 Effect of ambient turbulence intensity on sphere wakes at intermediate reynolds number. *AIAA Journal* **33** (1), 171–173.

- YOON, R.-H. 2000 The role of hydrodynamic and surface forces in bubble–particle interaction. *International Journal of Mineral Processing* **58** (1-4), 129 – 143.
- YOON, R. H. & LUTTRELL, G. H. 1989 The effect of bubble size on fine particle flotation. *Mineral Processing and Extractive Metallurgy Review* **5** (1-4), 101–122.
- ZAHNOW, JENS C. 2010 Aggregation and fragmentation dynamics of inertial particles in fluid flows. PhD thesis, University of Oldenburg.
- ZAHNOW, JENS C., MAERZ, JOERAN & FEUDEL, ULRIKE 2011 Particle-based modeling of aggregation and fragmentation processes: Fractal-like aggregates. *Physica D: Nonlinear Phenomena* **240** (9–10), 882 – 893.
- ZEYTOUNIAN, RADYADOUR KH. 2003 Joseph Boussinesq and his approximation: a contemporary view. *Comptes Rendus Mécanique* **331** (8), 575 – 586.
- ZHANG, LIFENG & THOMAS, BRIAN G 2003 Inclusions in continuous casting of steel. In *Proceeding of XXIV Steelmaking National Symposium*, pp. 138–183.
- ZISKIND, G., FICHMAN, M. & GUTFINGER, C. 1995 Resuspension of particulates from surfaces to turbulent flows—review and analysis. *Journal of Aerosol Science* **26** (4), 613 – 644.
- ZOHARY, TAMAR & ROBARTS, RICHARD D. 1990 Hyperscums and the population dynamics of microcystis aeruginosa. *Journal of Plankton Research* **12** (2), 423–432.
- ZWAAN, FOKKE 2010 Optical determination of particle concentrations in a water model. *Tech. Rep.* 150073. Tata Steel, Tata Steel Research, Development & Technology Ijmuiden Technology Centre SCC PRD Adress code 4H.16 PO Box 10000 1970 CA Ijmuiden, NL.

Acknowledgements

First and foremost, I want to thank my my supervisor René Delfos for all his support over the years of this project. With him I had the most vivid discussions about fluid dynamics, mathematics and philosophy in general while scribbling with chalk on his ancient blackboard. I particularly appreciate his “open door” attitude, the possibility to just bump into his office and quickly discuss some problems with data analysis or the experimental facility.

The latter is equally true for my promoter Jerry Westerweel. The discussions with him gave me a much better insight into the internals of PIV and helped a lot in getting the most out of my recorded camera images. He also provided some igniting sparks in the simplification of the equation of motion of a particle at moments when I was stuck, ideas that later lead to the derivation of the model for the wake entrainment.

I also want to thank Gijsbert Ooms for the time he spent with me on the theoretical parts of this work. He gave me a lot of input in form of old papers that turned out to be relevant to my problem, in particular Dayan & Zalmanovich (1982) was another spark that finally made the path towards the wake entrainment model clear. What I often found remarkable was that he did not only give advice during the regular meetings, but that he gave hints and ideas after having thought about them for a while. I think that this is an altitude towards science that is not often found in modern academia, unfortunately.

I want to express my special thanks for the support I got from the technicians of our lab. Joop created many mounts and adapters from quick’n’dirty drawings, and he was the first person to help with searching pieces of material that later became integral mechanical parts of the facilities. He was also the first to only talk to me in Dutch, after his “Where are you from?”, my reply “From Germany.” and the following “German? Dan kan ik ook Nederlands praten...” on my very first day in the lab. Cor helped in many ways for getting to run pump controllers solving all the little electronic problems that occur so frequently. A

6 Acknowledgements

good colleague and a person with truly golden hands was Simon, who contributed a major part to the build-up of the bubble trap facility. In particular the ingeniously simple but perfectly working bubble injector spoon was his design. I also enjoyed a lot the work with Edwin on the peak locking, and I appreciate his help with cameras and light sheet optics as much as his effort in holding back Gosse's passion for collecting in and piling up all potentially useful equipment at his setup. Likewise, my special thanks also to our two secretaries Ria and Caroline. Appreciating their work is often too easy to overlook, but they were always available for help, no matter whether it was fighting with bureaucracy or gently pushing supervisors to reading drafts. I enjoyed the collaboration with Fokke Zwaan on the work with the Corus (now Tata Steel) flotation facility, and in particular also with "my" Master students Michael Dauda and Audrey Giffard.

One thing that I will remember is the good atmosphere in this lab in general. There was a lot of support between the PhD students, from joint illegal milling sessions after seven o'clock over discussing photography equipment during lunch time to learning Dutch in front of the coffee machine or trying to revive my Russian. I certainly will not forget all our activities, whether it was the introduction to Belgian "Hopfenkaltshalen" during my first months in Delft, doing sports during zwemloops, nieuwjaarsduiks, surfing and go-carting, or biking tours with pancake dinners. Thank you all for a very enjoyable time here in this group: Uli, Jurriaan, Marc, Mark, Valentina, Jeanette, Carole, Sedat, Manu, Mathieu, Dirk-Jan, Vincent, Christian, Wim-Paul, Gerrit, Hyoungsoo, Nadine, Massimiliano, Marcel, Astrid, Sascha, Nikolay, Arnoud, Daniele, and Gosse. Last but not least, my thanks also to all the people at the RID and at WE.

The same thanks of mine for all the good years go to my compañeros Daniele, Artur, Isabel and Richard, and the people from the rowing club DDS, team "Angels", the EMRC, the MatCie and all the crazy marathoners.

I want to conclude this work with a last thought: I am convinced that every new-born human being is somewhat similar to a blank CD. Although there might be some differences in capacity for each of these CDs, what really matters is what has been written on over time, written on or maybe even burnt in by the environment a person grew up in. As a high capacity disk with a good sampling rate does not make bad music

any better, I am certain that the difference between tracks of dissonant sounds and those that make one enjoy a symphony largely depends on the environment a person lived in. In that sense I would like to name a few people that, even though they did not contribute to this work directly, had a positive influence on me, gave me an new perspective on things, were a source of motivation, or gave me a little push in the right direction at the right time. These people are: Ingrid Hahn, Heinz Krahn, Manfred Held, Klaus de Groot, and Reinhard Werner. Including my parents, Renate and Gustav Warncke, and my grand parents whom I could meet personally, Erna and Werner Grohmann, I want to thank them for having brought me to the point where I am now. I have learnt a lot from all of you.

Norbert Warncke
Delft, April 2014

About the Author

Norbert Warncke was born on 5 September 1979 in Wurzen, Germany. He grew up in Nerchau, and finished his secondary education at the “Gymnasium St. Augustin” in Grimma. After doing military service, he entered an educational programme in Information Technology at the “Berufsakademie Mannheim” in cooperation with the “Deutsches Zentrum für Luft- und Raumfahrt e.V.” in Braunschweig, and finished in 2002 as a Diplom-Ingenieur (BA) with a work on the image analysis of thermography recordings of airfoils in wind tunnel tests. During that time he enrolled in a correspondence course in Physics at the “Technische Universität Kaiserslautern” for the duration of two years. In 2002, he continued studying Physics at the “Technische Universität Braunschweig” and finished at the end of 2006 as Diplom-Physiker with a diploma thesis on “Structural Properties of Localised Quantum Operations”. His time in Braunschweig ended with a short employment as a Software Engineer for Real-Time Systems in Rail Automation.

In October 2007, he started his PhD project “Flotation and de-mixing of turbulent three-phase flows” at the Laboratory for Aero&Hydrodynamics at the “Technische Universiteit Delft”. The aim of this project was to study the hydrodynamic aspects of flotation, and although the focus of the project was on the experimental techniques using Multi-Phase PIV, it also left a bit of time for theoretical analysis. The results of this work are presented in this thesis. Following the completion of the experimental work on this project in January 2012, he worked as a Postdoc at the Nuclear Energy and Radiation Applications group on the thermohydraulics of supercritical fluids, followed in July 2013 by another Postdoc position at the Wind Energy group on boundary element methods for the simulation of wind turbines.